# A CONTROL-ORIENTED REAL-TIME SEMI-EMPIRICAL MODEL FOR THE PREDICTION OF NOX EMISSIONS IN DIESEL ENGINES

# POLITECNICO DI TORINO

I Facoltà di Ingegneria

**Dipartimento di Energetica**


Dottorato di Ricerca in Energetica
XXVIII ciclo


# A CONTROL-ORIENTED REAL-TIME SEMI-EMPIRICAL MODEL FOR THE PREDICTION OF NOX EMISSIONS IN DIESEL ENGINES


Candidato: Lezhong Fu

Tutori:

Politecnico di Torino

Prof. Antonio Mittica

Prof. Stefano d'Ambrosio

Ing. Roberto Finesso

Tongji University

Prof. Zhijun Wu


Marzo 2016

# Abstract

Nowadays motor vehicle population increases rapidly, and it and this leads to serious energy and environmental problems. Hence, the environment and energy issues are becoming more and more important around the world. Many potential technologies have been presented and researched in universities, institutes and companies. Diesel engines are employed in Europe widely due to high thermal efficiency. The PCCI combustion concept has the potential of simultaneously reducing both NOx and particulate matter emissions under an optimized control, and it will decrease the emissions of diesel engines further. Hence, the combustion control is important in diesel engine.

The present work describes the development of a fast control-oriented semi-empirical model that is capable of predicting NOx emissions in diesel engines under steady state and transient conditions. The model takes into account the maximum in-cylinder burned gas temperature of the main injection, the ambient gas-to-fuel ratio, the mass of injected fuel, the engine speed and the injection pressure. The evaluation of the temperature of the burned gas is based on a three-zone real-time diagnostic thermodynamic model that has recently been developed by the author. Two correlations have also been developed in the present study, in order to evaluate the maximum burned gas temperature during the main combustion phase (derived from the three-zone diagnostic model) on the basis of significant engine parameters. The model has been tuned and applied to two diesel engines that feature different injection systems of the indirect acting piezoelectric, direct acting piezoelectric and solenoid type, respectively, over a wide range of steady-state operating conditions. The model has also been validated in transient operation conditions, over the urban and extra-urban phases of the NEDC. It has been shown that the proposed approach is capable of improving the predictive capability of NOx emissions, compared to previous approaches, and is characterized

by a very low computational effort, as it is based on a single-equation correlation. It is therefore suitable for real-time applications, and could also be integrated in the engine control unit for closed-loop or feed-forward control tasks.

**Key Words:** Diesel engine; NOx emissions; Semi-empirical model; Control-oriented

# Nomenclature

$A$: heat transfer area

BDC: Bottom Dead Center

BMEP: Brake Mean Effective Pressure (bar)

$C_{mix}$: local mixing factor

CA: Crank Angle (deg)

CI: compression ignition

CFD: Computer Fluid Dynamics

CLD: chemiluminescence detector

*COC*: Centre of Combustion (deg)

DAP: Direct Acting Piezo

DoE: Design of Experiment

ECU: engine control unit

EGR: exhaust gas recirculation

$EI_{NOx}$: NOx emission index (g/kg fuel)

EVC: Exhaust Valve Closure

GMPT-E: General Motors PowerTrain-Europe

$h$: specific enthalpy (J/kg)

$h_c$: convective heat transfer coefficient

IAP: Indirect Acting Piezo

ICEAL-PT: Internal Combustion Engines Advanced Laboratory at the Politecnico di Torino

IVC: Intake Valve Closure

$K$: undetermined coefficients

LNT: lean NOx trap

$m$: mass; compression polytropic index

$m_{trap}$: trapped mass in the cylinder (g/cm$^3$ per stroke)

$m_{fuel}$: fuel mass

$m_{NOx}$: NOx mass per cycle/cylinder (g/(cyc·cyl))

$m_{O2}$: O2 mass in the cylinder (g/cm$^3$ per stroke)

*N*: engine speed (rpm)

NEDC: New European Driving Cycle

NOx: Nitrogen Oxides

PC: Personal Computer

PCCI: Premixed Charge Compression Ignition

*p*: pressure

$p_f$: injection pressure (hPa)

$p_{int}$: pressure in the intake manifold (Pa)

PMA: Pilot-Main-After injection strategy

PPM: Pilot-Pilot-Main injection strategy

PPMA: Pilot-Pilot-Main-After injection strategy

*q*: injected fuel volume (mm$^3$)

*Q*: heat transfer; energy (J)

$Q_{ch}$: heat release (J)

*R*: gas constant (J/(kg K)]; correlation coefficient

RMS: Root Mean Square

SCR: Selective Catalytic Reduction

SI: spark ignition

SOC: Start of Combustion

SOI: Start of Injection

$SOI_{main}$: Start of Injection of the main pulse

*t*: time (s)

*T*: temperature (K)

$T_{ad}$: adiabatic flame temperature (K)

$T_{bmax}$: maximum temperature of burned gas (K)

$T_{bmax,main}$: maximum temperature of burned gas of the main injection (K)

$T_{bSOC}$: temperature of burned gas at the start of combustion (K)

$T_{flame}$: adiabatic-stoichiometric flame temperature (K)

$T_{int}$: temperature in the intake manifold (K)

$T_w$: wall temperature (K)

TDC: Top Dead Center

THC: Total Unburned Hydrocarbons

$U_c$: expanded combined uncertainty

$V$: volume ($m^3$)

$X_r$: EGR rate (–)

$X_{r,tot}$: total residual gas fraction (–)

***Greek symbols***

$\lambda_{st}^{u}$: stoichiometric unburned gas-to-fuel ratio (–)

λ: relative air-to-fuel ratio (–)

***Subscripts***

*b*: burned gas zone

*EGR*: made up of EGR

*f*: vapor fuel zone

*f,inj*: injected fuel

*inj*: injection

*res*: made of residual gas

*st*: stoichiometric

*trap*: trapped in the cylinder

*u*: unburned gas zone

***Superscripts***

*u*: made up of unburned gas

***Notation***

*: constant in time

Δ: difference between time instant $t^i$ and time instant $t^{i-1}$

[*X*] : molar concentration o the *X* specie (mol/cm$^3$)

# Index

# Chapter 1 Introduction

Efforts to reduce the NOx emission products in diesel engines by car manufacturers have increased in recent years, due to the need to comply with the more and more stringent emission regulations. Innovative combustion techniques, such as the Premixed Charge Compression Ignition (PCCI) mode, have been developed in order to reduce in-cylinder NOx formation, and more and more efficient exhaust aftertreatment devices, such as SCRs and LNTs, have been introduced to further limit NOx tailpipe emissions.

The PCCI combustion concept has the potential of reducing both NOx and particulate matter emissions simultaneously [1], as it employs low-temperature highly-premixed combustion. Previous studies conducted by the authors have shown that the PCCI combustion mode can lead to a 15% reduction of NOx emissions at an almost constant soot level [1]. These emissions could be further reduced if an algorithm for the real-time estimation of the in-cylinder NOx formation were to be implemented in the engine control unit (ECU), in order to realize a cycle-to-cycle and cylinder-to-cylinder optimization. Interest in the development of real-time NOx models is therefore growing among car manufacturers, due to the increasing computational performance of modern ECUs.

The term “NOx” is in general used to indicate the sum of nitrogen monoxide (NO) and nitrogen dioxide ($NO_2$) emissions [2]. As far as internal combustion engines are concerned, $NO_2$ emissions are usually negligible in spark ignition (SI) engines, whereas they are of the order of 10–30% of the total NOx emissions in compression ignition (CI) engines, in which the higher concentrations are associated with lower load conditions [2],[3].

A common approach in the literature is to model only NO formation in the cylinder, and to consider it as an approximation of the total NOx emissions [4],[5]. This is justified by the fact that $NO_2$ is derived directly from the oxidation of NO.

It is well known that the NO formation process mainly depends on the following mechanisms [2],[3],[6]-[10]: the thermal mechanism, which depends to a great extent on the local temperatures and on the local oxygen concentration of the burned gases; the prompt mechanism, which is usually observed in fuel-rich mixtures; the fuel-derived NO mechanism, which is due to the presence of nitrogen in the reacting fuel.The thermal NO formation is described by the Zeldovich mechanism [6]-[8].In addition to the thermal mechanism, the prompt NOx formation mechanism was identified by Fenimore in 1971[11]. The NOx thermal mechanism is enhanced by the high local burned gas temperatures, which determine $O_2$ dissociation, and by the presence of $O_2$ in the flame region. It has recently been shown by Dec [12] that, in diesel sprays, these conditions occur in the stoichiometric diffusion flame that surrounds the jet, as well as in the post-combustion burned gas regions downstream from the diffusion flame.

The approaches adopted to predict in-cylinder NOx formation can be split into three main categories: phenomenological models, semi-empirical models and empirical models.

Phenomenological models calculate the in-cylinder NOx levels on the basis of a detailed analysis of the evolution of the thermodynamic and chemical properties of the in-cylinder content during the combustion process. This is done by means of 3D-CFD, quasi-dimensional or zero-dimensional thermodynamic models. The thermodynamic and chemical properties of the charge are then used as input quantities to implement NOx thermochemical sub-models, which are usually derived from the Zeldovich mechanism.Some examples of phenomenological models used to predict NOx are reported in [4],[5],[13]-[21].

Empirical models merely rely on measured data to identify relevant correlations for the prediction of NOx emissions; they have the advantage of requiring a low computational effort without detailed knowledge of the physical or chemical processes in the combustion chamber. Some empirical methods for the calculation of NOx, such as the one proposed in [22] can be found in the literature. Artificial intelligence systems and learning algorithms, such as neural networks and evolutionary algorithms, have also been introduced for emission prediction in IC engines [23]-[25]. However, these empirical models usually show a good predictive performance in the calibration range used for training, and their application is therefore limited as they are not physically consistent.

Semi-empirical models usually combine the physical and chemical parameters related to the NOx formation process, such as the center of combustion [26], the adiabatic flame temperature [27] or the heat release rate [28],[29], with relevant engine operating parameters that can be directly measured or evaluated, like empirical models. Semi-empirical models have the advantage of requiring a lower computational speed than phenomenological models, but are more physically-consistent and more accurate than empirical models. Moreover, semi-empirical models have proved to be reliable over a wide range of engine operation conditions [26]-[29]. For these reasons, they have been considered as good candidates for control-oriented and real time applications.

In this paper, a semi-empirical correlation has been developed to estimate the in-cylinder NOx mass. This correlation is based on several physical quantities, such as the maximum temperature of the burned gas zone of the main pulse, the stoichiometric ambient gas-to-fuel ratio, the engine speed and load and the injection pressure. The main novelties are that the in-cylinder maximum temperature of the burned gas zone is evaluated (instead of considering the adiabatic flame temperature usually adopted in the literature) by means of a real-time three-zone

diagnostic thermodynamic model, and the stoichiometric ambient gas-to-fuel ratio is proposed as a correlation parameter. The latter has been parametrized as a function of significant engine quantities, such as the EGR (exhaust gas recirculation) rate and the global relative air-to-fuel ratio of the engine. i.e., $\lambda$.

The three-zone diagnostic thermodynamic model has been recently presented by the authors in [13], in which a phenomenological NOx model, based on the Zeldovich thermal mechanism, was implemented.

Correlations have also been developed in the present study, in order to evaluate the maximum temperature of the burned gas of the main pulse, derived from the application of the three-zone diagnostic model, on the basis of significant engine parameters. This allows the semi-empirical NOx model to be used in all cases in which the in-cylinder pressure trace, which is necessary for the application of the three-zone model, is not available, as in the case of production engines, in which pressure sensors are usually not installed because of the high cost.

The method proposed in this thesis can lead to significant improvements in terms of computational costs, compared to phenomenological approaches, without any significant loss in accuracy, thanks to the inclusion of physically-consistent quantities. Moreover, the model could be applied for either diagnostic or predictive purposes; in the former case, the maximum burned gas temperature is evaluated by means of a diagnostic thermodynamic approach that starts from the measured in-cylinder pressure, like the one proposed in this thesis; in the latter case, the maximum burned gas temperature is evaluated on the basis of a predictive thermodynamic approach, like the one presented in [14].

The proposed model has been compared with other semi-empirical approaches [26],[27] and tested, under both steady-state and transient conditions, on two engines equipped with different injection systems. As far as transient conditions are concerned, the predicted vs. experimental NOx emissions were compared over the

NEDC (New European Driving Cycle). The model has been tested on a PC and it has been found that it requires very little computational time, that is, of the order of a few microseconds. The good test results therefore suggest that the model could be implemented in the ECU for control-oriented applications.

Finally, it should be noted that the model is suitable for different combustion modes, including PCCI and conventional ones, and is capable of evaluating the engine-out NOx emissions. In the case of an engine equipped with a DeNOx system, it should be necessary to develop a sub-model of the aftertreatment device, in order to evaluate also the tailpipe NOx emissions.

# Chapter 2 State of the art of semi-empirical models for the prediction of NOx

A detailed analysis on the main semi-empirical NOx models presented in the literature is reported in this section.

The first attempts to predict NOx emissions in diesel engines involved the use of the maximum in-cylinder average temperature, which was derived from the application of the ideal gas law to the in-cylinder content [26]. It has been shown in [26] that NOx emissions correlate well with the maximum in-cylinder average temperature but only in some operating conditions, such as in SOI (Start of Injection) sweeps tests, but do not correlate well in other conditions, e.g., when SOI is kept constant and the air-to-fuel ratio is varied. This can be explained by the fact that NOx formation is related more to the local burned gas temperature than to the average one, and the trend of the maximum average temperature is not always in line with that of the maximum burned gas temperature, depending on the operating conditions.

Improved correlations for the prediction of NOx have therefore been introduced. The first that is considered is the one presented in [26] by Gärtner et al., which calculates the NOx emission index $EI_{NOx}$ (g/kg fuel) as follows:

$$log(EI_{NOx}) = a_0 + a_1 \cdot COC + a_2 \cdot m_{cyl} + a_3 \cdot m_{O_2} \quad (2.1)$$

where $EI_{NOx}$ is the NOx emission index (g/kg fuel), *COC* is the Centre of Combustion (50% energy Conversion) (CA deg),

$m_{cyl}$ is the trapped mass in the cylinder (g/cm$^3$ per stroke),

$m_{O2}$ is the mass of oxygen trapped in the cylinder (g/cm$^3$ per stroke). And $a_0$–$a_3$ are calibration parameters.

It has been shown in [26] that the proposed correlation leads to good improvements in the prediction accuracy, compared to previous approaches based on the calculation of the maximum in-cylinder average temperature. However, this method does not take into account the observation that the local temperatures of the burned gases can vary to a great extent at constant *COC*, depending on the engine operating conditions (EGR rate, boost pressure, etc.), which lead to different in-cylinder pressure and temperature levels for equal values of *COC*.

The improvement in the accuracy of NOx prediction, obtained by means of Eq.(2.1) is mainly due to the addition of the *COC* parameter, which is related to the burned gas temperature levels.

Several semi-empirical correlations, which directly include the flame temperature among the input variables, have therefore been proposed in the literature. An example is reported by Krishnan et al. [27], and is represented by the following equation:

$$EI_{NOx} = C_{mix} \cdot e^{\left(\frac{-38700}{Tflame}\right)} \tag{2.2}$$

where $EI_{NOx}$ is the NOx emission index (g/kg fuel),

$C_{mix}$ is a local mixing factor that depends on the speed and load,

$T_{flame}$ is the adiabatic stoichiometric flame temperature (expressed in K) evaluated at the Start of Combustion (SOC). The model has the advantage of being able to directly include the maximum adiabatic flame temperature. However, the flame temperature is only one of the variables that are related to the formed NOx mass per cycle, and Eq. (2.2) is therefore not expected to be applicable for a wide range of operating conditions. Moreover, the model is based on the adiabatic flame temperature at SOC. The NOx formation rate depends on the actual time history of the temperature of the burned gases over the cycle [16],[17], and is expected to be more closely correlated to the maximum in-cylinder temperature of the burned gas than to the adiabatic flame temperature evaluated at SOC. The temperature of the

burned gas can in fact increase after SOC, due to the compression of the charge related to the expansion of the burned gases [16],[17]. Moreover, dissociation and heat transfer effects are not taken into account when the adiabatic flame temperature is considered.

A more complex model, which takes into account the whole trend of the adiabatic flame temperature over the cycle, has recently been proposed in [28]. This model is based on an integral approach that starts from the method illustrated in [29], according to which the total predicted NOx mass per cycle is calculated with the following equation:

$$m_{NOx,base} = \int_{\alpha} dQ_b(CA) \cdot K_1 \cdot \left(\frac{N}{2000}\right)^{K_2} \cdot e^{\left(\frac{K_3}{T_{ad}(CA)}\right)} dCA \tag{2.3}$$

where $N$ is the engine speed, $K_1$, $K_2$ and $K_3$ are tuning coefficients, $T_{ad}(CA)$ is the adiabatic flame temperature calculated as a function of the crank angle, and $dQ_{ch}$ is the instantaneous heat release.

This method has been improved in [28] by considering the NOx reduction mechanism. This mechanism is derived from the analysis of the diesel combustion process on the basis of the Dec conceptual scheme [12], which states that conventional diesel combustion is a two-stage process, made up of a rich premixed combustion phase and a stoichiometric diffusive combustion that takes place at the jet periphery. The diffusion flame generates NOx on the basis of the thermal mechanism. It has been suggested in [28] that a re-entrainment of the formed NOx can occur inside the rich premixed combustion region; this region is constituted by a highly reducing atmosphere, and part of the formed NOx is therefore reduced. Some of the NOx included in the EGR and residual gas can also be reduced on the basis of this mechanism. The whole set of equations is reported in [28] and is not explained in detail here for the sake of brevity.

This model has the advantage of being more physically-consistent than the other semi-empirical approaches. Although it has been reported in [28] that this model can be used for control-oriented applications, the main drawbacks are related to the fact that the approach is of the integral type, and the calculation of the predicted NOx mass per cycle therefore requires an integration over the entire combustion cycle. Moreover, a large number of equations is adopted, and this further increases the computational time, which is of the order of 4.5 ms when the elaboration is performed on a Pentium D PC.

The approach proposed in this work considers a single-equation semi-empirical correlation that predicts the formed NOx mass per cycle and per cylinder, without referring to an integral approach. This has been done in order to keep the computational time as low as possible, so that the model can be used for control-oriented applications.

# Chapter 3 Model description

## 3.1 Identification of the correlation variables

A preliminary discussion is reported hereafter, in order to identify the correlation variables that are expected to have most influence on the NOx formation process, and which should therefore be included in the semi-empirical model.

The NO formation reaction rate can be derived (as described in [13]) starting from the first three reactions of the super-extended Zeldovich mechanism:

$$\frac{d[NO]}{dt} = \frac{k_1^+ \cdot 2\left[1-\left(\frac{[NO]}{[NO]_e}\right)^2\right][N_2]_e[O]_e}{1+\left(\frac{[NO]}{[NO]_e}\right)\frac{k_1^+[N_2]_e[O]_e}{k_2^-[NO]_e[O]_e + k_3^-[NO]_e[H]_e}} \tag{3.1}$$

where the quantities in square brackets are expressed as molar concentrations in [mol/cm3], the subscript 'e' designates the equilibrium concentration at a given temperature and $K_1^+, K_2^+, K_3^+$ are quantified by the Miller expressions as a function of the temperature [2].

It should be noted that the NO molar formation rate is exponentially dependent on the burned gas temperature, which should therefore be taken into account in the semi-empirical NOx model.

The NOx derived from the thermal mechanism are mainly formed in the stoichiometric diffusion flame, according to the Dec conceptual scheme [12]. The NOx formation can then proceed in the post-combustion regions downstream from the diffusion flame, but, as dilution takes place, the reactions are frozen, as shown in [16],[17].

For a given NOx molar formation rate, which depends exponentially on the burned gas temperature, the mass of formed NOx per cycle and per cylinder depends on the mass of nitrogen and on the mass of oxygen that are available in the diffusive burned gas region. The mass of nitrogen and oxygen are functions of the mass of the unburned gas that participates in diffusive combustion, which is in turn proportional to the mass of injected fuel $m_{fuel}$. Since combustion is stoichiometric in

the diffusion flame [12], the total mass of unburned gas that reacts with the fuel, through the diffusion flame, is the product of the total injected fuel mass and the stoichiometric ambient gas-to-fuel ratio (which will also be denoted as "unburned gas-to-fuel ratio"), i.e., $\alpha_{st}^{u}$ . It has been shown in [13] that $\alpha_{st}^{u}$ depends to a great extent on the EGR rate and on the global relative air-to-fuel ratio $\lambda$ of the engine. For example, the higher the EGR rate, the lower the oxygen concentration in the combustion chamber, the higher the mass of unburned gas required for stoichiometric combustion of the unit fuel mass and, as a consequence, the higher values of $\alpha_{st}^{u}$ are therefore associated with lower in-cylinder oxygen concentrations, and these could lead to lower NOx formation rates at constant burned gas temperatures. Therefore, $m_{fuel}$ and $\alpha_{st}^{u}$ should be included in the semi-empirical model to predict the total NOx mass formed per cycle and per cylinder.

The burned gases generated by diffusive combustion dilute with the surrounding charge, and this can lead to a quick reduction in the temperatures, with a consequent blocking of the NOx formation rate. Moreover, a re-entrainment of the hot gases can occur in the jet, as shown in [28], and this could lead to a certain NOx reduction. Both physical processes are closely related to the in-cylinder turbulence, and the latter is also related to the injected fuel velocity (i.e., to injection pressure $p_f$) and to engine speed $N$. Moreover, a higher injection pressure can lead to better atomization and fuel/air mixing, through an extended spray penetration. This could cause higher NOx formation rates, due to locally higher temperatures and oxygen rich regions close to the beginning of the combustion process [30].

The gas temperature of the burned gas zone that has to be considered for the NOx correlation should not be the maximum one over the cycle ($T_{bmax}$), but the maximum one during the burning of the main injection ($T_{bmax,main}$). The main contribution to NOx formation is in fact related to the main injection, because the latter is the one with the highest value of injected fuel mass. This has also been shown in [16]-[18], where the results were obtained with a quasi-dimensional multizone model.

An example is reported in Fig. 3.1, which shows the predicted trends of the burned gas temperatures for different values of the start of injection of the main pulse, i.e., baseline (red solid curve), baseline delayed of 10 deg (blue dotted line), baseline delayed of 20 deg (black pointed line). The baseline point corresponds to an experimental acquisition of the 2000 × 5 key-point (the number before the *x* sign represents the engine speed in rpm and the other one is the BMEP in bar), while the other curves were obtained with the predictive heat release model presented in [14]. It can be noted in the figure that as SOI is delayed, $T_{bmax,main}$ decreases accordingly. $T_{bmax,\mathrm{main}}$ is only equal to the maximum burned gas temperature in the baseline case, but is not in the other two conditions, as $T_{bmax}$ occurs at TDC. Since NOx emissions usually decrease when $\mathrm{SOI_{main}}$ is delayed, $T_{bmax,main}$ is a more robust correlation parameter than $T_{bmax}$.

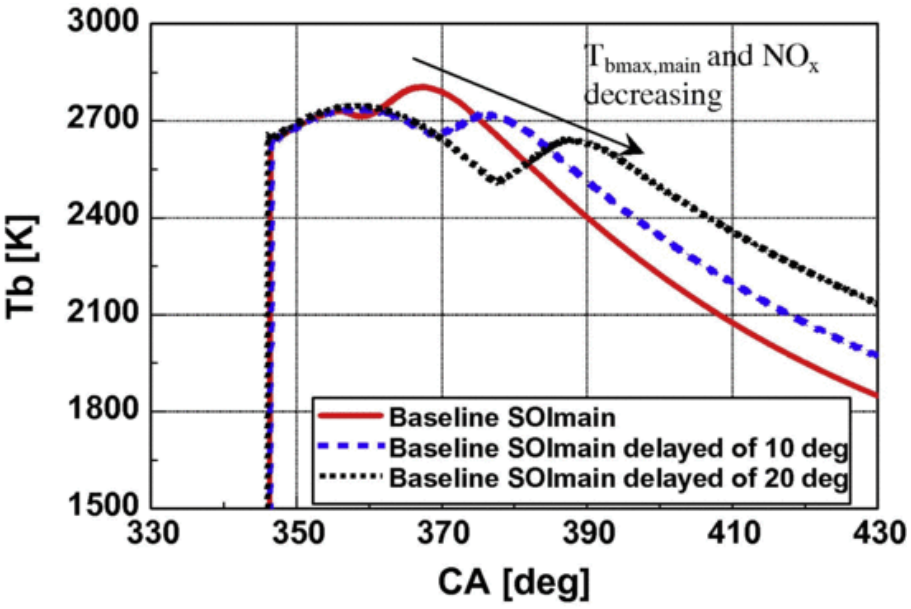


**Fig. 3.1** Trends of the burned gas temperatures for different values of $\mathrm{SOI_{main}}$.

An additional engine parameter that was initially considered to be included in the model is the swirl ratio. A higher swirl ratio leads to a higher fuel/air mixing, which in turn promotes a higher burn rate and a higher temperature of the burned gases, thus leading to higher NOx formation rates. However, it was verified that including the swirl ratio among the correlation variables leads to a small

improvement in the accuracy of the model. This can be justified considering that, in a diagnostic approach, the measured in-cylinder pressure is an input for the three-zone thermodynamic model. Therefore, variations in the swirl ratio reflect in variations in the in-cylinder pressure trace, and the related effects on the burned gas temperatures and NOx formation rates are therefore indirectly taken into account by the three zone model.

On the basis of all the previous considerations, the formed NOx mass per cycle and per cylinder, i.e., $m_{NOx}$, should be a function of the following quantities:

$$m_{NOx} = f(T_{b\,max,main}, \alpha_{st}^{u}, m_{fuel}, N, p_f) \tag{3.2}$$

and the following functional form has been proposed:

$$m_{NOx} = K \cdot e^{\frac{K_1}{T_{b\,max,main}}} \cdot (\alpha_{st}^{u})^{K_2} \cdot (m_{fuel})^{K_3} \cdot (N)^{K_4} \cdot (p_f)^{K_5} \tag{3.3}$$

where $K$, $K_1$–$K_5$ are tuning factors, and the maximum burned gas temperature of the main pulse is included in the model by means of an exponential term, as suggested in [2] and on the basis of the exponential dependence of the NOx formation reaction rates on the temperature of the burned gases.

The mass of injected fuel, engine speed and injection pressure can be evaluated directly from the ECU measurements. The maximum burned gas temperature can be evaluated by applying the real-time three-zone diagnostic model that was recently presented in [13].

The unburned gas-to-fuel ratio can be correlated to the total EGR and residual gas fraction $X_{r,tot}$ and to the global relative air-to-fuel ratio $\lambda$, as reported in [13], as follows:

$$\alpha_{st}^{u} = 132.08\left(\frac{X_{r,tot}}{\lambda}\right)^4 - 78.471\left(\frac{X_{r,tot}}{\lambda}\right)^3 + 38.115\left(\frac{X_{r,tot}}{\lambda}\right)^2 + 13.695\frac{X_{r,tot}}{\lambda} + 14.379 \tag{3.4}$$

## 3.2 Real time three-zone thermodynamic diagnostic model

The maximum burned gas temperature of the main pulse used in Eq. (3.3) was

determined by applying the real-time three-zone diagnostic thermodynamic model recently presented in [13]. The approach is suitable for control-oriented applications, as the equations can be solved in closed form without an iterative procedure. The basic equations are summarized hereafter. The reader can refer to [13] for a more detailed description of the approach.

The model has been derived by simplifying the premixed-diffusive multizone diagnostic model previously developed and presented in [16]-[18], which was based on the Dec conceptual scheme ([12]): diesel combustion is a two-stage process that usually starts with fuel-rich premixed combustion, the products of which complete the oxidation process through a stoichiometric diffusion flame located at the jet periphery.

Rich premixed combustion is responsible for the formation of soot and incomplete combustion products, such as CO and THC, while stoichiometric diffusive combustion is responsible for NOx formation ([12]).

The rich premixed combustion zone has been disregarded for the thermodynamic model proposed in this study, because the latter has been coupled to a sub-model to estimate the formation of nitrogen oxides. This simplification is also justified by the consequent reduction in the computational time, a critical parameter for real-time applications. The authors have verified that the removal of the rich premixed burned gas zone does not lead to remarkable differences in the values of the maximum temperature of the diffusive burned gas zone, which is one of the key-variables for the semi-empirical NOx proposed correlation (see Eq. (3.3)).

The combustion chamber is divided into three zones: a vapor-fuel zone (f), an unburned gas zone (u), made up of fresh-air, residual gas and EGR, and a burned gas zone (b) obtained from a globally stoichiometric combustion process. The zones are treated as homogeneous and made up of ideal gas, and pressure is considered uniform throughout the combustion chamber.

The combustion process in the model includes the following steps: from the IVC (Intake Valve Closure) to the SOI (Start of Injection), only the unburned zone exists

before fuel is injected into the cylinder; from the SOI to the SOC (Start of Combustion), an endothermic vapor-fuel zone is generated after fuel injection; after the SOC, a stoichiometric burned gas zone is generated, which consumes the fuel zone and the unburned gas zone. The burned gas zone is considered to be made up of $CO_2$, $H_2O$, $O_2$, $N_2$, O, H, OH and NO, and dissociation effects are therefore taken into account, in order to achieve an accurate calculation of the burned gas temperatures.

The total trapped mass, $m^*_{trap}$ has to be evaluated to estimate the mass and oxygen concentration of the unburned gas zone. This mass is given by the sum of the trapped mass of fresh air, residual gas and EGR, according to the following equation:

$$m^*_{trap} = m^*_a + m^*_{res} + m^*_{EGR} \tag{3.5}$$

where the asterisk denotes a constant quantity in time.

The total trapped mass can be evaluated adopting different procedures, depending on the specific application for which the model is used.

In fast transient applications, as well as in onboard applications, the trapped fresh air mass, $m^*_a$ can be derived directly from the ECU measurements, and the trapped mass of EGR, i.e., $m^*_{EGR}$ can be calculated by means of the procedure outlined in [31], which is based on the duty-cycle signal of the EGR valve and on the thermodynamic conditions upstream and downstream from the EGR valve. In steady-state applications at the test bench, the mass $m^*_a$ can be derived as the product of the injected fuel mass, obtained from the measurement of the rate of the fuel mass consumed by the engine, and the air-to-fuel ratio, calculated on the basis of the measured emissions with the procedure reported in [32]. The EGR rate can be derived, in these kinds of applications, on the basis of the $CO_2$ level measured in the intake manifold with the procedure illustrated in [32]. The last two procedures for the calculation of $m^*_a$ and $m^*_{EGR}$ provide a higher degree of accuracy than those that are based on ECU measurements and on the duty cycle of the EGR valve. However, these procedures cannot usually be used in fast transient conditions, as the emissions at the engine exhaust or the $CO_2$ levels in the intake manifold are generally

measured by means of low frequency acquisition systems, and because some mixing of the gases can occur in the pipes between the engine and the gas analyzer. The measured levels are therefore an average of the instantaneous levels that occur in the intake or exhaust manifolds during transient conditions. Moreover, these procedures cannot be used for onboard applications, as the intake $CO_2$ level and the emissions are not available to the ECU.

The residual gas mass $m_{res}^{*}$ can be calculated, for both steady-state and fast transient applications, by applying the ideal gas law to the in-chamber volume at EVC (Exhaust Valve Closing), considering the values of pressure and temperature of the previous cycle.

The approach is based on the application of the energy conservation equations, written in the Eulerian nonstationary form, of the mass conservation equations and on the volume congruence equation to the three zones. It can be shown ([13]) that combining the abovementioned relations, the following equations hold for the three zones in the time interval *dt*, under the assumption of a stoichiometric combustion:

$$\delta Q_f + V_f dp = d\left(m_f h_f\right) - dm_{f,inj} h_{f,inj} + dm_{f\to b} h_f \tag{3.6}$$

$$\delta Q_u + V_u dp = d\left(m_u h_u\right) + dm_{u\to b} h_u \tag{3.7}$$

$$\delta Q_b + V_b dp = d\left(m_b h_b\right) - dm_{u\to b} h_u - dm_{f\to b} h_f \tag{3.8}$$

The specific enthalpy of the *j*th zone is denoted with $h_j$, while $dm_{f,inj}$ is the injected fuel mass in the time interval *dt*, which is calculated on the basis of the injection rate profile. The in-chamber pressure is denoted by *p*, and $\delta Q_j$ indicates the infinitesimal heat transfer between the *j*th zone and the walls of the combustion chamber, which is evaluated by means of a convective formulation using the Woschni heat transfer coefficient ([33]). The stoichiometric unburned gas-to-fuel ratio $\alpha_{st}^{u}$ was already introduced in the previous section, and indicates the mass of unburned gas that is required for stoichiometric combustion of the unit fuel mass.

It has been verified in [13] that second-order polynomial correlations are able to accurately describe the specific enthalpy variation of the different zones, as follows:

$$h_j = a_j T_j^2 + b_j T_j + c_j \tag{3.9}$$

On the basis of the volume congruence equation, it is possible to derive the mass of burned gas $m_b$ at each time instant as a function of the measured in-cylinder pressure, as follows:

$$m_b = \frac{pV - m^*_{trap} R_u T_u - m_{f,inj} R_f T_f}{R_b T_b - \frac{\alpha^u_{st}}{1+\alpha^u_{st}} R_u T_u - \frac{1}{1+\alpha^u_{st}} R_f T_f} \tag{3.10}$$

Finally, from the mass conservation equations, the mass of unburned gas zone and fuel zone can be derived as a function of the mass of the burned gas zone, as follows:

$$m_f = m_{f,inj} - \frac{m_b}{1+\alpha^u_{st}} \tag{3.11}$$

$$m_u = m^*_{trap} - \frac{m_b}{1+\alpha^u_{st}} \alpha^u_{st} \tag{3.12}$$

As reported in [13], Eqs.(3.6)-(3.8) are then discretized considering finite time intervals $\Delta t = t^i - t^{i-1}$. It is thus possible to explicitly derive the temperature of the three zones by solving the resulting second-order polynomial equations for the three zones:

$$a^{II}_j \left(T^i_j\right)^2 + b^{II}_j T^i_j + c^{II}_j = 0 \tag{3.13}$$

Table 3.1 reports a summary of the method used to derive the mass and temperature of the zones in closed form. The coefficients of Eq. (3.13) are also reported.

It has been shown in [13] that the application of the three-zone model requires a computational time that is of the order of 1 ms on a Pentium D PC for the simulation of the entire cycle.

**Table 3.1** Summary of the method used to solve the mass and temperature of the three zones in closed form.

$$m_b^i = \frac{p^i V^i - m_{trap}^* R_u T_u^{i-1} - m_{f,inj}^i R_f T_f^{i-1}}{R_b T_b^{i-1} - \frac{\alpha_{st}^u}{1+\alpha_{st}^u} R_u T_u^{i-1} - \frac{1}{1+\alpha_{st}^u} R_f T_f^{i-1}}; \qquad p^i \ \ measured$$

$$m_u^i = m_{trap}^* - \frac{m_b^i}{1+\alpha_{st}^u}\alpha_{st}^u \qquad\qquad m_f^i = m_{f,inj}^i - \frac{m_b^i}{1+\alpha_{st}^u}$$

$$T_j^i = \frac{-b_j^{II} + \sqrt{\left(b_j^{II}\right)^2 - 4a_j^{II}c_j^{II}}}{2a_j^{II}}; \qquad i_j^i = a_j T_j^{i2} + b_j T_j^i + c_j \qquad j = u, b, f$$

$$\alpha_{st}^u = 132.08\left(\frac{X_{r,tot}}{\lambda}\right)^4 - 78.471\left(\frac{X_{r,tot}}{\lambda}\right)^3 + 38.115\left(\frac{X_{r,tot}}{\lambda}\right)^2 + 13.695\frac{X_{r,tot}}{\lambda} + 14.379$$

$$X_{r,tot} = \frac{m_{EGR}^* + m_{res}^*}{m_a^* + m_{EGR}^* + m_{res}^* + m_{f,inj}^*}; \; m_{trap}^* = m_a^* + m_{res}^* + m_{EGR}^*; \; m_{f,inj}^i = \int_{tSOI}^{t^i} \dot{m}_{f,inj} dt$$

$$\dot{Q}_j = h_j A_j \left(T_j - T_w\right); \qquad h_j = h_j(c_0)$$

| | $a_j^{II}$ | $b_j^{II}$ | $c_j^{II}$ |
|---|---|---|---|
| **f** | $\left(m_f^i + \Delta m_{f,inj}\right)a_f$ | $\left[\left(m_f^i + \Delta m_{f,inj}\right)b_f - \frac{m_f^i R_f \Delta p}{p^i}\right]$ | $-\dot{Q}_f^{i-1}\Delta t + \left(m_f^i + \Delta m_{f,inj}\right)c_f - m_f^i i_f^{i-1} + -\Delta m_{f,inj} i_{f,inj}^i$ |
| **u** | $m_u^i a_u$ | $\left[m_u^i b_u - \frac{m_u^i R_u \Delta p}{p^i}\right]$ | $-\dot{Q}_u^{i-1}\Delta t + m_u^i\left[c_u - i_u^{i-1}\right]$ |
| **b** | $\left[m_b^i + \Delta m_b\right]a_b$ | $\left[m_b^i + \Delta m_b\right]b_b - \frac{m_b^i R_b \Delta p}{p^i}$ | $-\dot{Q}_b^{i-1}\Delta t + \left[m_b^i + \Delta m_b\right]c_b + -m_b^i i_b^{i-1} - \frac{\Delta m_b}{1+\alpha_{st}^u}\alpha_{st}^u i_u^i - \frac{\Delta m_b}{1+\alpha_{st}^u} i_f^i$ |

| | $\mathbf{a_i}$ | $\mathbf{b_i}$ | $\mathbf{c_i}$ |
|---|---|---|---|
| **f** | *1.44590* | *860.78* | *− 949736* |
| **u** | *0.09983* | *982.30* | *− 477140 + − 2817105* $\frac{X_{r,tot}}{\lambda}$ |
| **b** | *0.31703* | $\begin{pmatrix} 426.31 + \\ -0.68863\,p \end{pmatrix}$ | $-2851737 + 517.97p + +2.3173\,p^2$ |

However, for the present application it is not necessary to perform a complete elaboration of the cycle, as only the maximum burned gas temperature during the combustion of the main shot ($T_{bmax,main}$) is required for Eq.(3.3) and not the entire temperature trend as a function of the crank angle. Considering that $T_{bmax,main}$ occurs just after TDC, the required elaboration time should be further reduced.

# Chapter 4 Test engine, experimental setup and activity

## 4.1 Test engine

The engine used for model calibration was a GM 2.0 $dm^3$ 16 V twin-stage turbocharged Euro 5 engine, equipped with piezoelectric injectors. In addition, a GM 1.6 $dm^3$ automotive medium-sized Euro 6 diesel engine, equipped with solenoid injectors, was considered for model testing and validation. The main specifications of the two engines are given in Table 4.1. The experimental tests were carried out at the AVL highly dynamic test bench installed at ICEAL-PT (Internal Combustion Engine Advanced Laboratory at the Politecnico di Torino).

**Table 4.1** Main specifications of the engines.

| **Engine type** | **2.0 $dm^3$ 4 cylinders "Twin-Stage" Euro 5** | **1.6 $dm^3$ 4 cylinders in-line Euro 6** |
|---|---|---|
| **Displacement** | 1956 $cm^3$ | 1598 $cm^3$ |
| **Bore × stroke** | 83.0 mm × 90.4 mm | 79.7 mm × 80.1 mm |
| **Conrod length** | 145 mm | 135 mm |
| **Compression ratio** | 16.5 | 16.0 |
| **Valves per cylinder** | 4 | 4 |
| **Turbocharger** | Twin-stage with valve actuators and WG | Single stage VGT with rack position feedback |
| **Fuel injection system** | Common Rail injection | Common Rail Solenoid 2000 bar 3rd generation |
| **Nominal rated power and torque** | 140 kW @ 4000 rpm | 100 kW @ 3500–4000 rpm |
| | 400 Nm @ 1750–2500 rpm | 320 Nm @ 2000–2500 rpm |

## 4.2 Experimental setup and uncertainty

The test rig is shown in Fig. 4.1, and it was equipped with: an 'ELIN AVL APA 100' AC dynamometer; an 'AVL KMA 4000' system, used to continuously meter engine fuel consumption; an 'AVL AMAi60' raw exhaust-gas analyzer. The latter is basically made up of three analyzer trains. Two of these have: one heated chemiluminescence detector (CLD), to analyze NOx–NO; a couple of heated flame ionization detectors, to analyze THC/CH4; three nondispersive infrared analyzers, to measure low and high CO as well as $CO_2$ concentrations; one paramagnetic oxygen detector to measure O2. These trains allow the pollutant levels to be measured upstream and downstream from the aftertreatment equipment at the same time. The third train has only one instrument to measure the $CO_2$ levels in the intake manifold, in order to evaluate the EGR ratios of the engine. The dynamic test bed was also equipped with an AVL 415S smokemeter, an AVL 439S opacimeter and an AVL SPC472 Smart Sampler in order to measure the soot emissions from diesel engines.

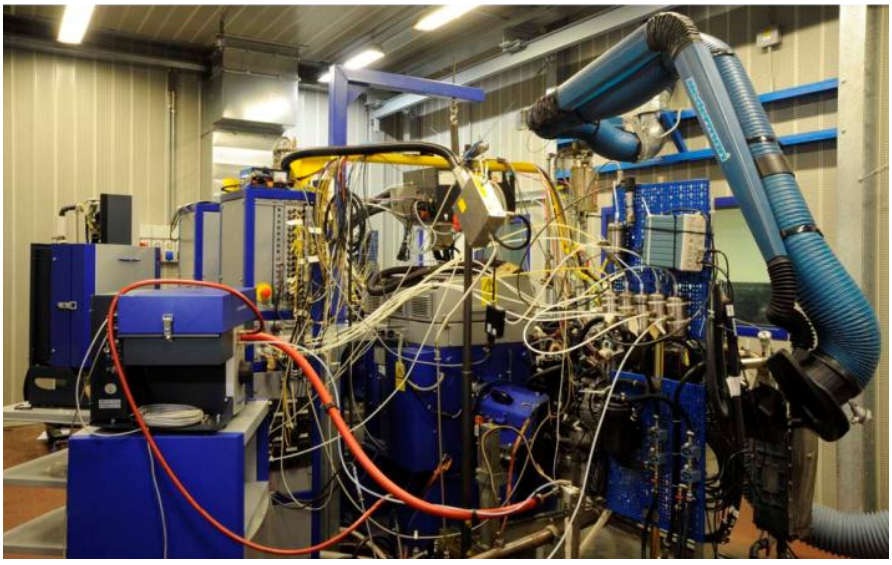

**Fig. 4.1** Highly-dynamic test rig

All of the abovementioned measuring instruments were controlled by the AVL PUMA OPEN 1.3.2 automation system. The model for real-time NOx emission prediction and control was implemented in AVL IndiCom software, which offers an open and friendly compiling environment for the user. The test bed environment

was interfaced with AVL CAMEO software to run intelligent engine calibration procedures on the basis of the DoE (Design of Experiment) approach.

The engines were fully instrumented with piezoresistive pressure transducers and *K* and *T* thermocouples to measure the pressure and temperature levels at various engine locations. An 'NGK' UEGO air–fuel ratio sensor was placed inside the exhaust system. A Kistler 6058A41 high-frequency piezoelectric transducer was fit to the glow-plug seat to measure the in-cylinder pressure time-histories. The in-chamber pressure traces were referenced on the basis of the pressure in the intake manifold, which was measured by means of a high-frequency Kistler 4075A10 piezoresistive transducer. The latter was located at the inlet runner of the cylinder equipped with the in-cylinder pressure sensor.

The procedure applied to evaluate the experimental uncertainties was based on the recommended practices reported in [36].

Given an output quantity *y*, which is dependent on *N* independent variables $x_i$, the associated variance $u_c^2(y)$ can be calculated by means of the following expression:

$$u_c^2(y) = \sum_{i=1}^{N} \left( \frac{\partial f}{\partial x_i} \right)^2 u^2(x_i) = \sum_{i=1}^{N} c_i^2 u^2(x_i) \tag{4.1}$$

Equation (36) can be considered consistent if the mutual effects between the independent variables are neglected.

$c_i$ is called the "sensitivity coefficient" of the output quantity *y* with respect to the *i-th* independent variable $x_i$.

Once $u_c^2(y)$ has been evaluated, and a level of confidence, for example, of 95%, and a corresponding coverage factor *k* equal to 2 have been assumed, it is possible to evaluate the expanded combined uncertainty of *y*, i.e., $U_c(y)$:

$$U_c(y) = k\sqrt{u_c^2(y)} \tag{4.2}$$

$U_c(y)$ is the uncertainty associated with the calculated quantity *y*.

If the independent variables $x_i$ are the result of a measurement, the associated variance $u^2(x_i)$ is estimated taking into account the accuracy of the instrument that is stated in the calibration certificate, the repeatability, the instrument resolution and the master uncertainty.

The uncertainty of the measured NOx concentration at the engine exhaust, used for the model validation, has been evaluated according to the proposed procedure.

This uncertainty mainly depends on two contributions: the uncertainty of the NOx calibration cylinder, which is used for the span adjustment of the CLD device, and the accuracy of the CLD gas analyzer.

Two calibration ranges were used to measure the NOx concentration in the exhaust gas, the first from 0 to 150 ppm and the second from 0 to 1000 ppm.

Table 5 reports the expanded uncertainty of the NOx concentration in the two calibration cylinders used for both low and high measurement ranges (Table 4.2a), and the main sources of error of the CLD device (Table 4.2b).

**Table 4.2** CLD calibration ranges (a) and data available to evaluate the measurement errors of the CLD device (b).

| Range | Full Span | Expanded uncertainty U |
|---|---|---|
| 1 | 150 | 2% |
| 2 | 1000 | 2% |

(a)

| Error type | Error |
|---|---|
| Linearity | ≤2% of measured value (10-100% of full scale range)<br>≤1% of full scale range<br>whichever is smaller |
| Drift 24h | ≤1% of full scale range |
| Reproducibility | ≤0.5% of full scale range |

(b)

Table **4.3** reports an example of the calculated expanded uncertainty for different measured NOx concentrations. The expanded uncertainty is lower when the measurement is close to the full span range used for calibration (Tab. 6a), because the linearity error in the CLD is higher in the middle between the zero value and the full span calibration value, and is lower near the two calibration boundaries.

**Table 4.3** Calculated expanded uncertainty for different values of the NOx concentrations.

| Measured NOx [ppm] | Expanded uncertainty [bar] | Expanded uncertainty [%] |
|---|---|---|
| 50 | 1.6 | 3.06 |
| 100 | 2.5 | 2.48 |
| 500 | 16.3 | 3.26 |
| 1300 | 32.7 | 2.52 |

## 4.3 Experimental activity

The experimental data were acquired in the frame of research projects carried out with GMPT-E.

The research activity conducted on the 2.0 $dm^3$ diesel engine is explained in detail in [34]. The ultimate goal of the activity was to assess the potentiality of innovative piezo- and solenoid-driven Common Rail injection systems as far as engine performance, emissions, fuel consumption and combustion are concerned. Particular attention was paid to the effects of the advanced injection patterns enabled by each Common Rail system.

A standard calibration set, featuring an injection schedule with a pilot shot and a main pulse, was used as the baseline, and three advanced injection patterns were taken into account, namely:

- *PPM:* two pilot pulses and a main injection;
- *PMA:* a pilot pulse and a main injection followed by an after pulse;
- *PPMA:* two pilot pulses and a main injection followed by an after pulse.

The injection strategies were optimized at six key-points, which were chosen in order to characterize engine operation of a medium-sized passenger car during an NEDC, in terms of engine speed and BMEP (1500 × 2, 1500 × 5, 2000 × 2, 2000 × 5, 2500 × 8, 2750 × 12 rpm × bar). Different calibration sets were identified for each key-point and each considered injection strategy by means of a specifically developed DoE approach ([34],[35]).

Table 4.4 summarizes the maximum and minimum values of the engine parameters considered in the variation lists of the DoE. Additional experimental data, related to EGR-sweeps ($X_r$ = 0–50%), for the six key-points were also included in the dataset. About 900 experimental tests were carried out.

**Table 4.4** Minimum and maximum range of variation of the main engine parameters for the variation lists and the EGR-sweep tests conducted on the 2.0 dm3 diesel engine with IAP injectors.

| Key-point | No. of tests | | $p_f$ | Intake $O_2$ | λ | $q_{pil2}$ | $q_{pil1}$ | $q_{aft}$ | $q_{f,inj}$ | SOI pil2 | SOI pil1 | SOI main | SOI aft |
|---|---|---|---|---|---|---|---|---|---|---|---|---|---|
| | | | bar | % | - | $mm^3$ | $mm^3$ | $mm^3$ | $mm^3$ | CAD | CAD | CAD | CAD |
| 1500x2 | 148 | max | 600 | 16.48 | 1.93 | 2.0 | 2.5 | - | 14.4 | 357.8 | 362.7 | 366.9 | - |
| | | min | 300 | 13.88 | 1.31 | 0.8 | 0.8 | - | 8.9 | 328.0 | 342.9 | 360.4 | - |
| 1500x5 | 133 | max | 900 | 17.59 | 1.66 | 1.5 | 2.0 | - | 21.6 | 352.1 | 359.5 | 366.3 | - |
| | | min | 600 | 14.63 | 1.18 | 0.8 | 0.8 | - | 18.6 | 329.9 | 345.8 | 362.0 | - |
| 2000x2 | 144 | max | 700 | 16.99 | 2.08 | 2.0 | 2.5 | - | 16.5 | 355.5 | 362.0 | 367.7 | - |
| | | min | 400 | 13.87 | 1.16 | 0.7 | 0.7 | - | 9.6 | 316.2 | 338.6 | 361.0 | - |
| 2000x5 | 134 | max | 1150 | 17.30 | 1.67 | 1.5 | 2.0 | - | 21.6 | 347.4 | 356.6 | 366.0 | - |
| | | min | 750 | 15.06 | 1.31 | 0.8 | 0.8 | - | 19.3 | 319.0 | 340.0 | 361.5 | - |
| 2500x8 | 130 | max | 1400 | 18.42 | 1.77 | - | 1.5 | 4.0 | 35.4 | - | 351.1 | 362.2 | 394.7 |
| | | min | 1000 | 15.55 | 1.3 | - | 0.7 | 0.7 | 29.5 | - | 330.6 | 357.1 | 376.4 |
| 2750x12 | 160 | max | 1800 | 18.21 | 1.41 | - | 1.3 | 4.0 | 52.9 | - | 344.2 | 359.6 | 392.0 |
| | | min | 1500 | 15.82 | 1.12 | - | 0.7 | 0.7 | 43.9 | - | 326.5 | 355.5 | 376.3 |
| EGR-sweep tests | 70 | max | 1482 | 20.89 | 4.25 | - | 1.7 | - | 44.6 | - | 351.7 | 364.8 | - |
| | | min | 453 | 14.96 | 1.32 | - | 1.1 | - | 9.5 | - | 332.9 | 356.8 | - |

# Chapter 5 Model calibration and identification of correlations to evaluate $T_{bmax,main}$

## 5.1 Model calibration

The semi-empirical NOx formation model given by Eq. (3.3) has been calibrated, for the 2.0 $dm^3$ Euro 5 diesel engine, by means of the least square method, on the basis of the steady-state variation list tests whose specifications are reported in Table 4.4. This has allowed the (K, $K_1$-$K_5$) coefficient set to be determined. One half of the dataset has been used for model calibration, while the remaining half has been used for model validation.

The resulting tuned semi-empirical model used to predict the formed NOx mass per cycle, i.e., $m_{NOx}$, is:

$$m_{NOx} = 43144 \cdot e^{\frac{-15984}{T_{b\,max,main}}} \cdot (\alpha_{st}^{u})^{-6.8046} \cdot (m_{fuel})^{0.6547} \cdot (N)^{-0.2908} \cdot (p_f)^{0.7883} \quad (5.1)$$

A discussion on the model coefficients is reported hereafter.

The negative coefficient of the temperature term is in line with the observations reported in Charpter 2. The negative coefficient of the $\alpha_{st}^{u}$ term can be explained by the fact that higher values of $\alpha_{st}^{u}$ are associated with lower in-cylinder oxygen concentrations, which lead to lower NOx formation rates at a fixed burned gas temperature. The positive sign of the $m_{fuel}$ term can be explained by the fact that the higher the injected fuel mass, the higher the mass of nitrogen (and oxygen) involved in the stoichiometric burned gas region, and the higher the formed NOx mass per cycle for an equal molar NOx formation rate. The positive exponent of the injection pressure terms is in line with the results reported in the literature, according to which a direct correlation exists between injection pressure and NOx formation. The engine speed term has a negative exponent. This could be related to such effects as the re-entrainment of part of the NOx mass generated through the diffusion flame

into the jet, with a consequent partial reduction according to the process described in [28]. Moreover, the increase in the engine speed reduces the absolute resident time for the oxidation of $N_2$, and the expansion freezes the burning gas earlier.

## 5.2 Identification of correlations to evaluate $T_{bmax,main}$

The evaluation of the maximum burned gas temperature during the combustion of the main pulse ($T_{bmax,main}$) requires the application of the real-time three-zone thermodynamic model, which in turn requires, as input, the in-cylinder pressure trace. This can be either measured according to a diagnostic approach, or simulated by means of a combustion predictive approach (see [14]).

The development of a robust correlation to evaluate $T_{bmax,main}$ could be of great interest for all the applications in which the in-cylinder pressure trace is not available, as in the case of production engines, in which pressure sensors are usually not installed because of the high cost, and also to further decrease the computational effort required by the semi-empirical NOx model in control-oriented applications.

The three-zone diagnostic combustion model has been applied to all the test cases reported in Table 4.4, in order to derive a dataset of experimentally-derived $T_{bmax,main}$ values. These values were then used to derive the following correlation:

$$T_{bmax,main} = 1832.8 \cdot (m_{fuel})^{0.0165} \cdot (N)^{-0.0080} \cdot (T_{SOImain})^{0.2688} \cdot (\alpha_{st}^{u})^{-0.4950} \quad (5.2)$$

In Eq. (5.2), $Tb_{max,main}$ is expressed in K, $m_{fuel}$ in g/(cyc·cyl), $N$ in rpm and $T_{SOImain}$ in K.

The maximum burned gas temperature is in fact expected to be related to the charge temperature at the SOI of the main shot, to the stoichiometric unburned gas-to-fuel ratio, which is related to the in-cylinder oxygen concentration, and to the fuel mass and engine speed, which could be related to the heat transfer effects, that are engine load and speed-dependent.

The temperature of the charge at SOI of the main shot is evaluated on the basis of the following equation, which assumes a polytropic evolution from BDC to SOI:

$$T_{SOImain} = T_{int}\left(\frac{V_{BDC}}{V_{SO\,Imain}}\right)^{m-1} \tag{5.3}$$

in which *m* represent the polytropic index of the compression process. Eq. (5.3) also indirectly takes into account the effect of the engine compression ratio on the charge temperature.

The parameter $T_{SOImain}$ takes into account the effect of the engine compression ratio, by means of the volume ratios, and the effect of the injection strategy (i.e., the start of the main injection).

The parameters of most influence on $T_{bmax,main}$, in Eq. (5.2), are $T_{SOImain}$and $\alpha_{st}^{u}$.The sign of the exponents is consistent, as $T_{bmax,main}$ increases with$T_{SOImain}$, and decreases when $\alpha_{st}^{u}$ increases (i.e., the EGR rate increases or λdecreases).

A simplified correlation, which is only dependent on the intake manifold thermodynamic conditions (pint, Tint) and on $\alpha_{st}^{u}$, was also taken into account:

$$T_{bmax,main} = 7031.2 \cdot (P_{int})^{0.1160} \cdot (T_{int})^{-0.3069} \cdot (\alpha_{st}^{u})^{0.2133} \tag{5.4}$$

In Eq. (5.4), $T_{bmax,main}$ is expressed in K, $p_{int}$ in Pa and $T_{int}$ in K.

This correlation does not take into account the engine compression ratio or the injection strategy.

Fig. 5.1 reports the predicted vs. experimental values of $T_{bmax,main}$, obtained using either Eq. (5.2) (Fig. 5.1a and b) or Eq. (5.4) (Fig. 5.1c and d) for the calibration (Fig. 5.1a and c) and validation (Fig. 5.1b and d) datasets. The experimental values were obtained using the three-zone diagnostic model.

It can be observed that Eq. (5.2) leads to a very high correlation coefficient ($R$ = 0.978 for the calibration dataset and $R$ = 0.971 for the validation dataset), while the results are still good, but less accurate, with Eq. (5.4) ($R$ = 0.953 for the calibration dataset and $R$ = 0.936 for the validation dataset).

An analysis of the uncertainty on the predicted values of $T_{bmax,main}$, using either Eq. (5.2) or Eq. (5.4), has been carried out in order to verify the robustness of both equations to the errors associated in the input parameters. Considering an operating condition for the 1500 × 5 key-point with a nominal value of $T_{bmax,main}$ equal to 2590 K,

and assuming an error on the values of the input variables of ±1%, the resulting uncertainty of $T_{bmax,main}$ is of about 33 K (i.e., 1.2%) using Eq. (5.2) (where the predominant uncertainty sources are related to the parameters *m*(75%) and $\alpha_{st}^{u}$ (20%)) and of about 11 K (i.e., 0.42%) using Eq. (5.4) (where the predominant uncertainty sources are related to the parameters $T_{int}$ (60%) and (30%)). As a consequence, Eq. (5.2), although more accurate than Eq. (5.4), seems to be less robust when the uncertainty of the input variables, and especially of the*m* coefficient, is high.

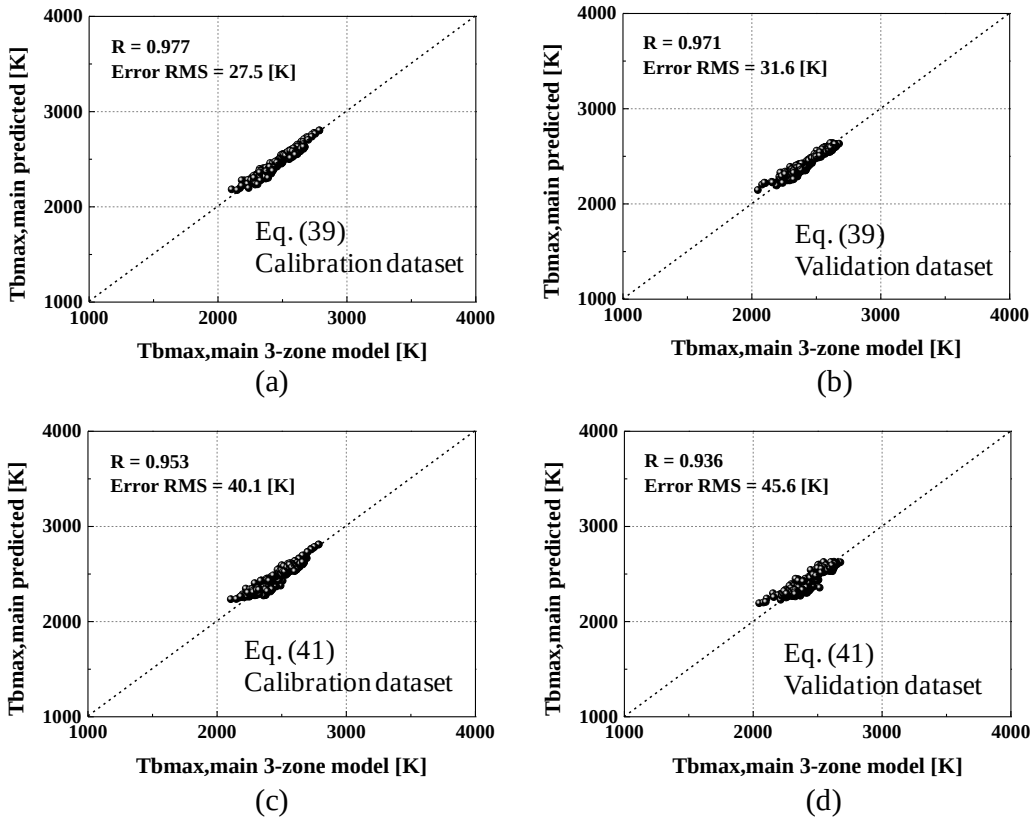


**Fig. 5.1** Comparison between the predicted (Eqs. (5.2)and(5.4)) and calculated (3-zone model) values of $T_{bmax,main}$ using the calibration dataset (a, c) and the validation dataset (b, d).

In conclusion, Fig. 5.2 reports a scheme of the proposed methodology, where the main input variables are indicated.

**Model calibration and identification of correlations to evaluate $Tb_{max,main}$**

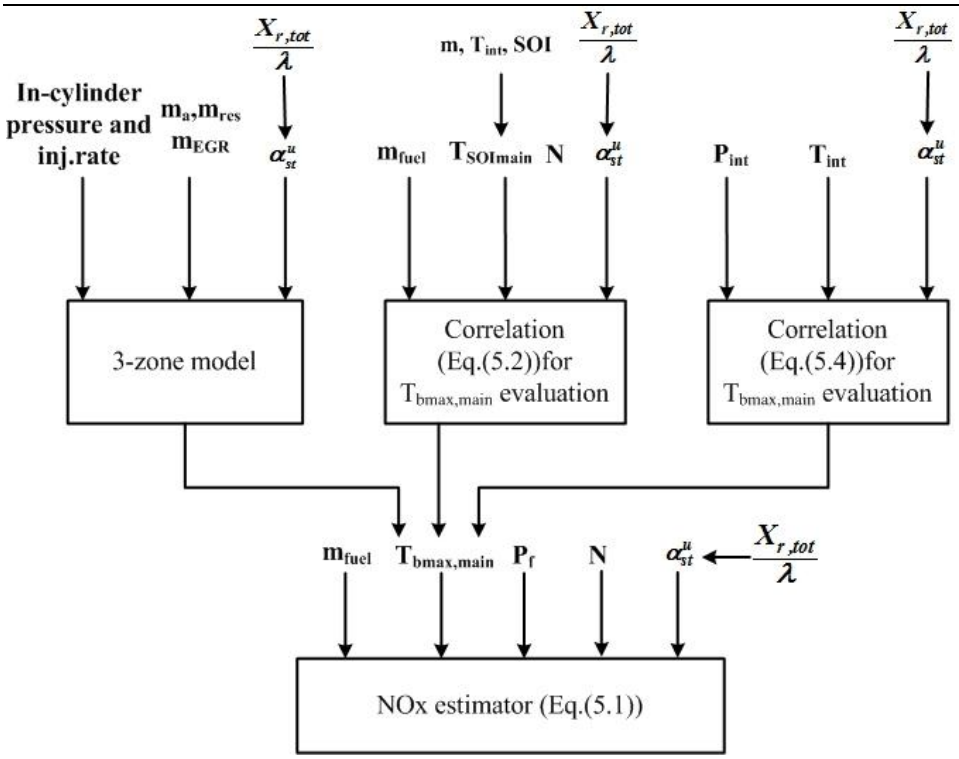


**Fig. 5.2** Scheme of the proposed methodology.

# Chapter 6 Results and discussion

## 6.1 Model tuning and application to the 2.0 dm3 engine with IAP injectors

In this section, the model proposed by the authors has been applied to the steady-state DoE tests of the 2.0 $dm^3$ "Twin-Stage" Euro 5 engine equipped with IAP injectors. One half of the dataset has been used for the calibration of the models, and the other half for the validation.

A comparison between the proposed model and the two correlations presented in [26] and [27], and expressed by Eqs.(2.1) and (2.2), has also been carried out, as they are of the single-equation type like the one proposed in this paper. Both models were re-tuned on the experimental data considered in the present study, as follows:

$$log(EI_{NOx}) = 1.2234 - 0 \cdot 0001458COC - 4207 \cdot m_{cyl} + 24366 \cdot m_{O_2} \quad (6.1)$$

$$EI_{NOx} = 2.657E7 \cdot e^{\left(\frac{-38700}{Tflame}\right)} \quad (6.2)$$

The units of NOx emissions, calculated with the above-mentioned models, were converted from emission indexes into mg per cycle and per cylinder, for an easier comparison with the results of the proposed approach.

Fig. 6.1 reports the predicted vs. experimental values of the formed NOx mass [mg/(cyc·cyl)], obtained with the authors' model (Eq. (5.1)) (Fig. 6.1a), Gärtner's model (Eq. (6.1)) (Fig. 6.1b) and Krishnan's model (Eq. (6.2)) (Fig. 6.1c), respectively. The values of the correlation coefficient *R* and of the RMS error (Root Mean Square of the prediction error) are also reported in the graphs. The higher *R* value and the lower RMS of the proposed model show a significant improvement in the prediction of the in-cylinder formed NOx mass, compared to the previous approaches.

Fig. 6.1d reports the values of the RMS error for the three models at different key-points. It should be noted that the values of the RMS error are similar for the

three considered models for low-load conditions, while the proposed method leads to a better accuracy for medium–high load conditions.

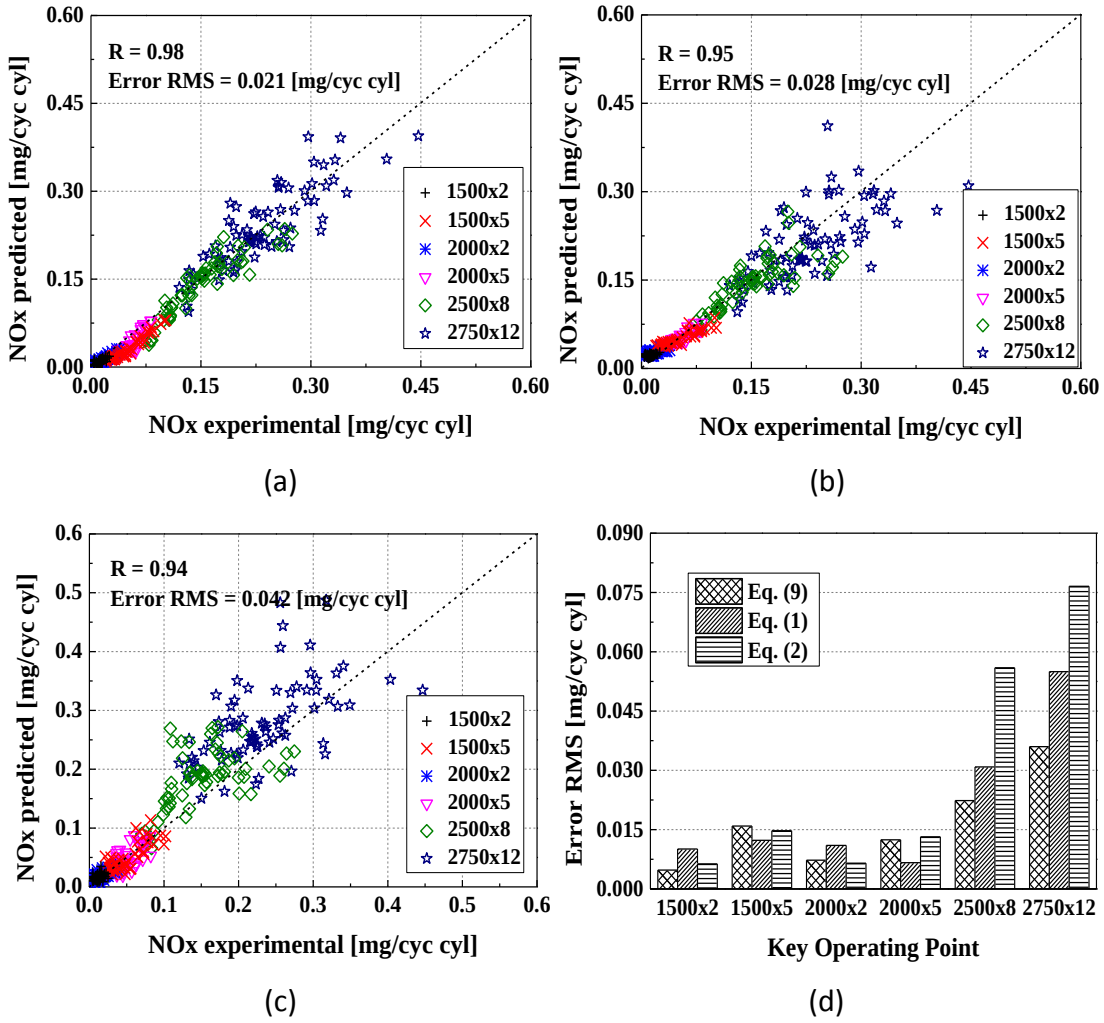


**Fig. 6.1** Comparisons between the models described by Eqs. (5.1), (6.1), and (6.2) at different key-points, on the 2.0 dm$^3$engine with IAP injectors, for the DoE conditions reported in Table 4.4.

The improvements obtained with the proposed model (Eq. (5.1)) compared to Eq. (6.1) is mainly related to the adoption of the actual maximum temperature of the burned gas zone instead of the *COC* parameter, which leads to a more physically-consistent approach. It should be noted that the NOx formation is more and more sensitive to $T_{bmax,main}$ as the EGR rate is lower and engine load is higher, and this justifies the higher accuracy of the proposed method at higher loads. The improvements given by the proposed model, compared to Eq. (6.2), are probably

due to the fact that Eq. (6.2) evaluates the adiabatic temperature calculated at SOC ($T_{bSOC}$) instead of the actual maximum temperature during the combustion of the main pulse. Fig. 6.2 reports the $T_{bSOC}$ vs. $T_{bmax,main}$ for several DoE tests (Table 4.4) and different key-points. It can be observed that even though the two quantities are related to each other, a large dispersion of $T_{bmax,main}$ values can occur at constant values of $T_{bSOC}$, especially for high values of $T_{bmax,main}$ (i.e., at high load conditions). This dispersion can even be of the order of 100 K, and can lead to inaccurate NOx predictions if $T_{bSOC}$ is included as a correlation variable.

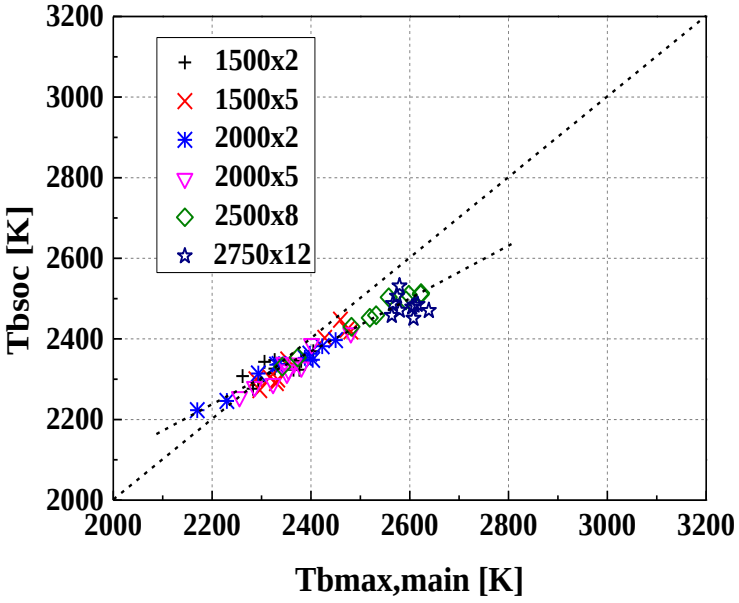


**Fig. 6.2** $T_{bSOC}$ vs. $T_{bmax,main}$ at different operation conditions (N[rpm] x BMEP [bar]), on the 2.0 dm$^3$ Euro 5 diesel engine with IAP injectors, for several DoE test conditions (Table 4.4).

Fig. 6.3 reports the trends of the temperature of the three zones (Fig. 6.3a) and of the in-cylinder NOx concentration (Fig. 6.3b), which was predicted with the phenomenological approach reported in [14], for a test condition at the 2750 × 12 key-point. It can be observed that $T_{bmax,main}$ is much higher than $T_{bSOC}$, as a consequence of the effect of the unburned gas compression that occurs after SOC, due to the expansion of the burned gases. The figure also shows that $T_{bmax}$ is slightly different from $T_{bmax,main}$. It can also be noted that the main NOx formation region is

in the interval around $T_{bmax,main}$, which is therefore a more robust correlation parameter than $T_{bSOC}$ for the semi-empirical NOx correlation.

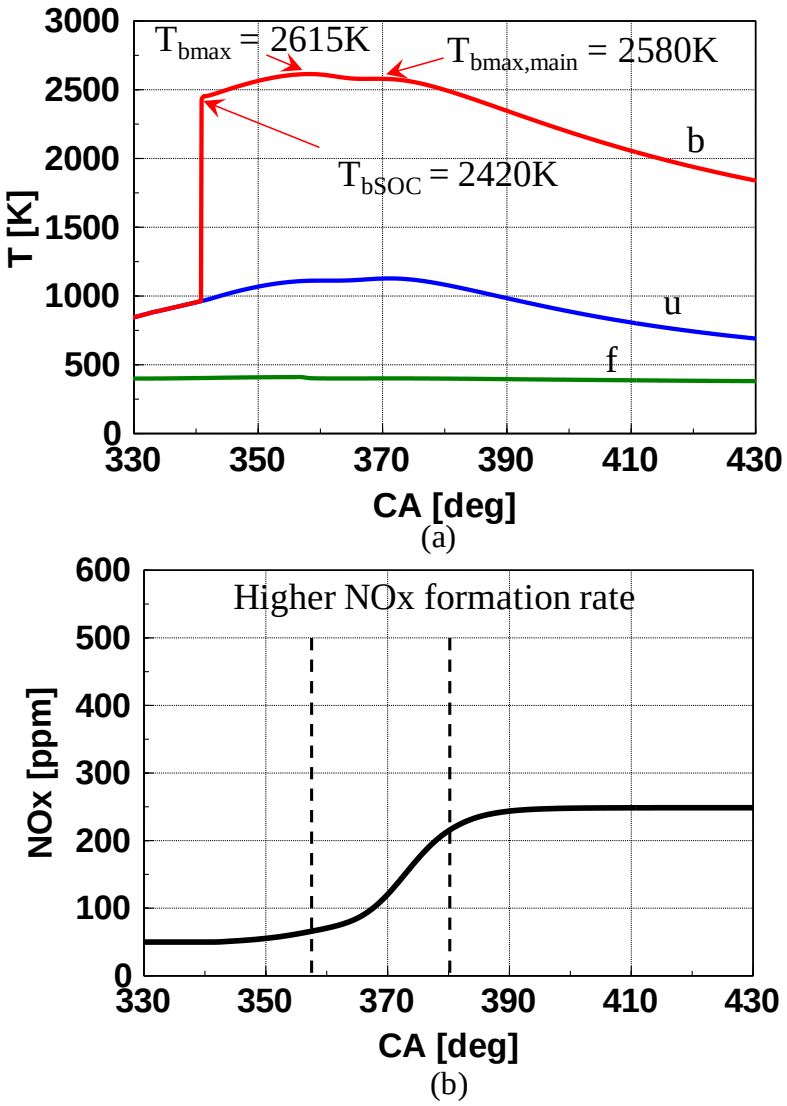


**Fig. 6.3** Temperature of the different zones (a) and in-cylinder NOx trend predicted with the phenomenological approach described in [13], for a test case on the 2.0 $dm^3$ Euro 5 diesel engine at the 2750x12 key-point.

This can also be confirmed in Fig. 6.4, which reports the formed NOx mass per cycle and per cylinder as a function of $T_{bmax,main}$, for EGR-sweep tests at different key-points. It can be observed that a good correlation exists between the two quantities, and it can be improved by accounting for the other correlation variables included in (3.3).

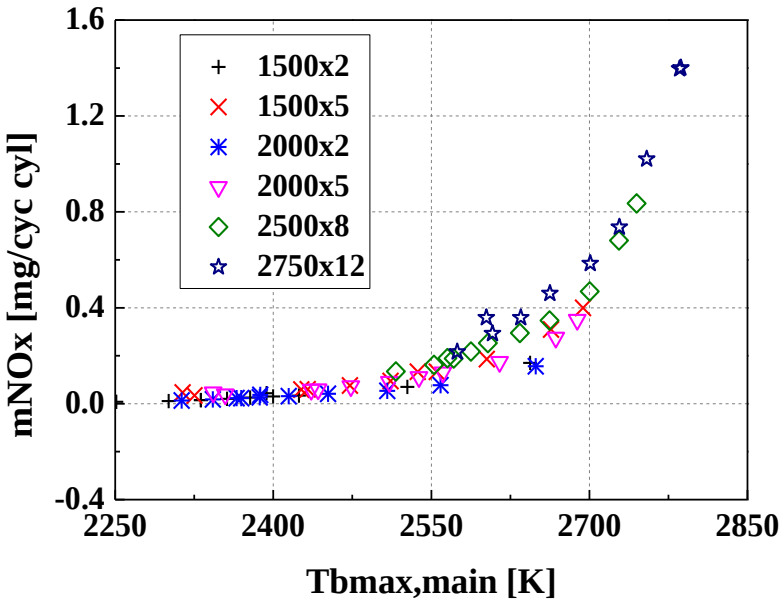


**Fig. 6.4** Te Formed NOx mass per cycle vs. maximum burned gas temperature of the main injection for the EGR-sweep tests at different operating conditions (N[rpm] × BMEP [bar]), on the 2.0 $dm^3$ engine with IAP injectors, for several DoE test conditions (Table 4.4).

## 6.2 Model application to the 2.0 dm3 engine with DAP (Direct Acting Piezoelectric) injectors

The model tuned with the results of the tests run on the 2.0 $dm^3$ engine equipped with the IAP injectors (i.e., (5.1)), was also tested to predict NOx emissions for the same engine equipped with DAP injectors, in order to test the robustness of the model with a different injection system. EGR sweep tests conducted at the NEDC key-points were considered.

The simplified approach for the calculation of $T_{bmax,main}$ was used, using either Eq. (6.1) or (6.2), in order to evaluate the fastest approach for the estimation of the NOx mass.

Fig. 6.5a shows the predicted vs. experimental values of the in-cylinder NOx mass, along with the values of the correlation coefficient and of the RMS error, using Eq. (6.1), while Fig. 9b shows the same quantities obtained with Eq. (6.2).

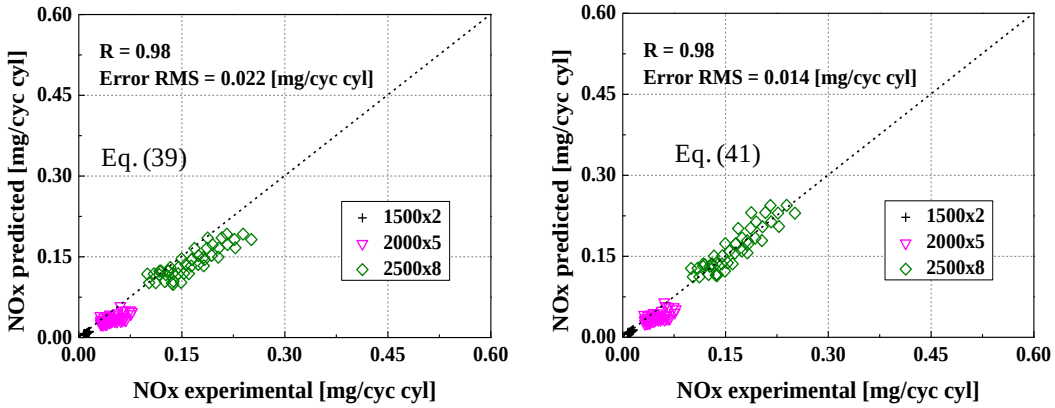


**Fig. 6.5** Predicted vs. experimental values of the in-cylinder NOx mass, for the 2.0 $dm^3$ Euro 5 diesel engine with DAP injectors, considering EGR-sweep tests at different key-points and using Eq. (6.1) (a) or Eq. (6.2) (b).

The correlation coefficient can be considered good for both approaches, even though a systematic, slight underestimation of the NOx mass occurs when Eq. (6.1) is used, as it is characterized by a higher RMS error than Eq. (6.2). This could be probably justified considering that, according to the analysis of the uncertainty of Eqs. (6.1) and (6.2), the results of Eq. (6.1) are more sensitive to the uncertainties related to the polytropic compression coefficient *m*. This underestimation could be corrected by including a pre-multiplying coefficient in Eq. (5.1) which is injector-dependent. However, the good correlation coefficient suggests that the proposed model is robust with respect to a change in the injection system configuration.

## 6.3 Model application to the 1.6 dm3 engine with solenoid injectors

The model tuned with the results of the tests run on the 2.0 $dm^3$ engine equipped with the IAP injectors (i.e., Eq. (5.1)), was then applied to the 1.6 $dm^3$medium-sized Euro 6 diesel engine equipped with solenoid injectors (Table 4.1). Engine mapping test were considered (N: 1000–4000 rpm; BMEP: 0.5–25 bar).

As in the cases with DAP injectors, the simplified approach for the calculation of $T_{bmax,main}$ was used, using either Eq. (6.1) or Eq. (6.2), to establish the fastest approach to estimate the NOx mass.

Fig. 6.6a reports the predicted vs. experimental values of the predicted in-cylinder NOx mass, along with the values of the correlation coefficient and of the RMS error, using Eq. (6.1), while Fig. 6.6b shows the same quantities obtained with Eq. (6.2).

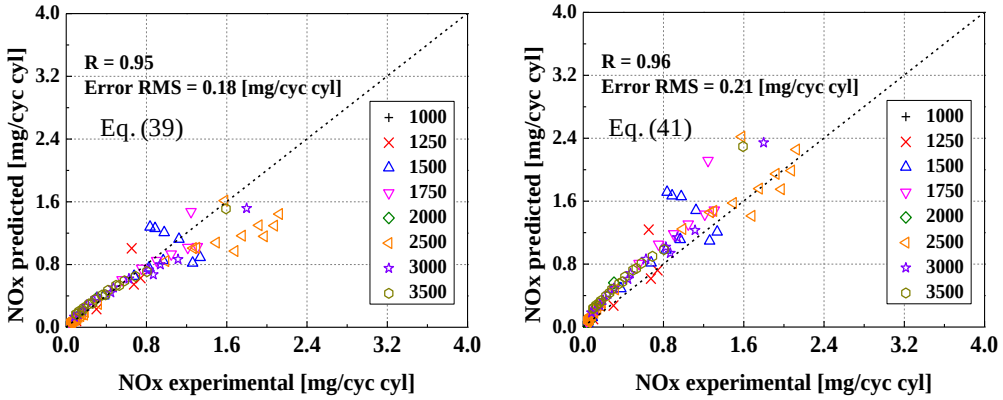


**Fig. 6.6** Predicted vs. experimental values of the in-cylinder NOx mass for the 1.6 dm3 Euro 6 diesel engine with solenoid injectors, considering engine map tests at different key-points and using Eq. (6.1) (a) or Eq. (6.2) (b).

The high correlation coefficient obtained for both simplified approaches suggests that the proposed model is robust with respect to a change in the injection system configuration.

## 6.4 Model application in transient operation conditions over an NEDC

Finally, the model was utilized to predict the NOx emissions for the 2.0 $dm^3$ "Twin-Stage" Euro 5 engine equipped with IAP injectors over three different NEDCs performed at the dynamic test bench of the ICEAL-PT. Eq. (6.1) and (6.2) were used to evaluate $T_{bmax,main}$, as the in-cylinder pressure was not measured during the tests, and the real-time three-zone model therefore could not be applied.

Fig. 6.7a, 12c and 12e report the time histories of the predicted (black thick lines) and the experimental (red dotted lines) NOx instantaneous emissions [g/s] for the three considered NEDCs, while the predicted vs. experimental values are shown in Fig. 6.7b, 12d and 12e, respectively. The results were obtained using Eq. (6.1).

The values of the correlation coefficient R and of the RMS error obtained using Eq. (6.1) and Eq. (6.2) are also reported in the graphs.

It can be observed that the values of R and RMS error, referring to the prediction of the instantaneous NOx mass emissions, are of the same order of magnitude for the two approaches.

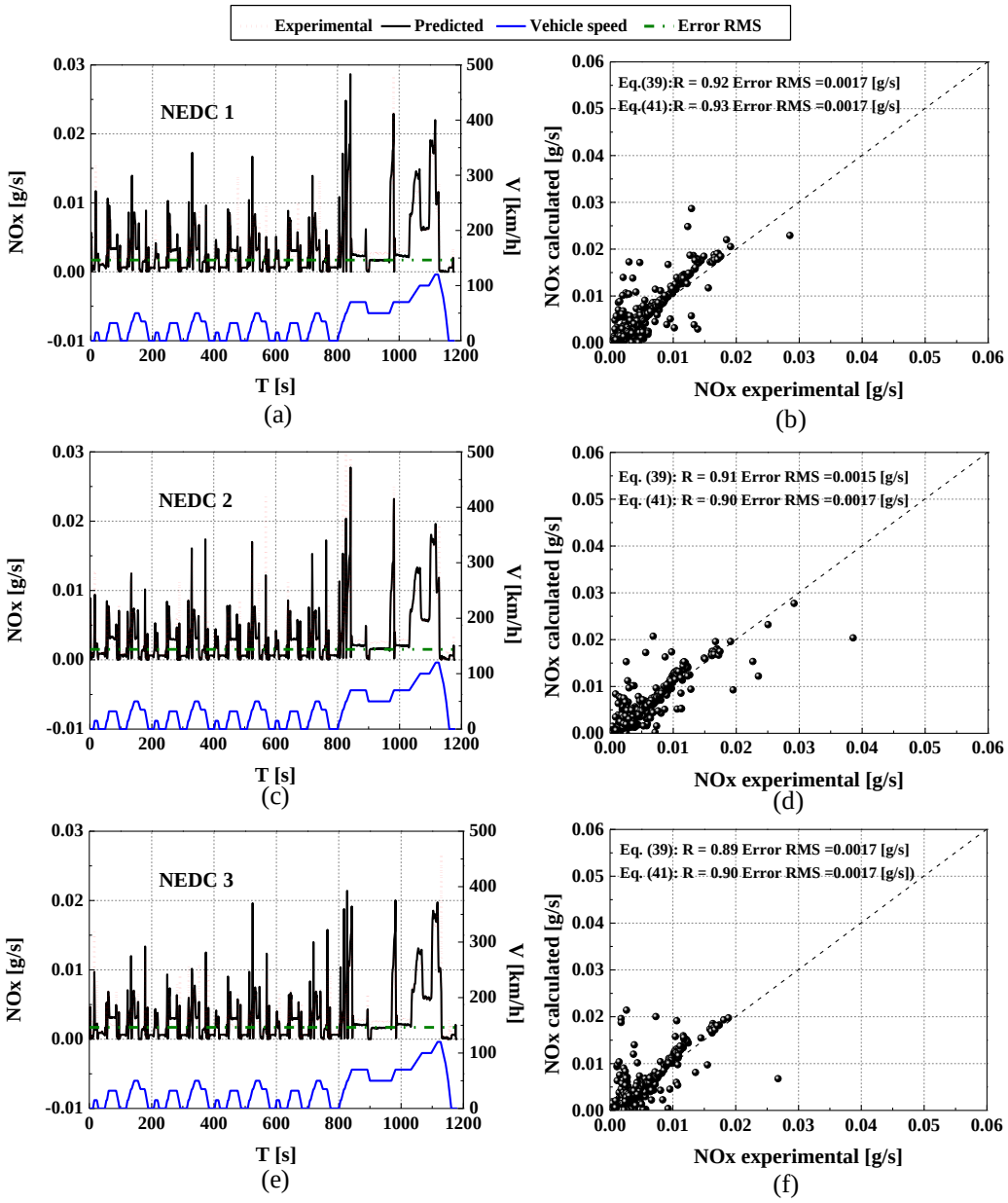


**Fig. 6.7** Time histories of the predicted (Eq. (6.1)) and experimental instantaneous NOx emissions for the three considered NEDCs(a, c, e); predicted (Eq. (6.1)) vs.

experimental instantaneous NOx emissions(b, d, f). The values of R and RMS obtained with Eq. (6.2) are also reported.

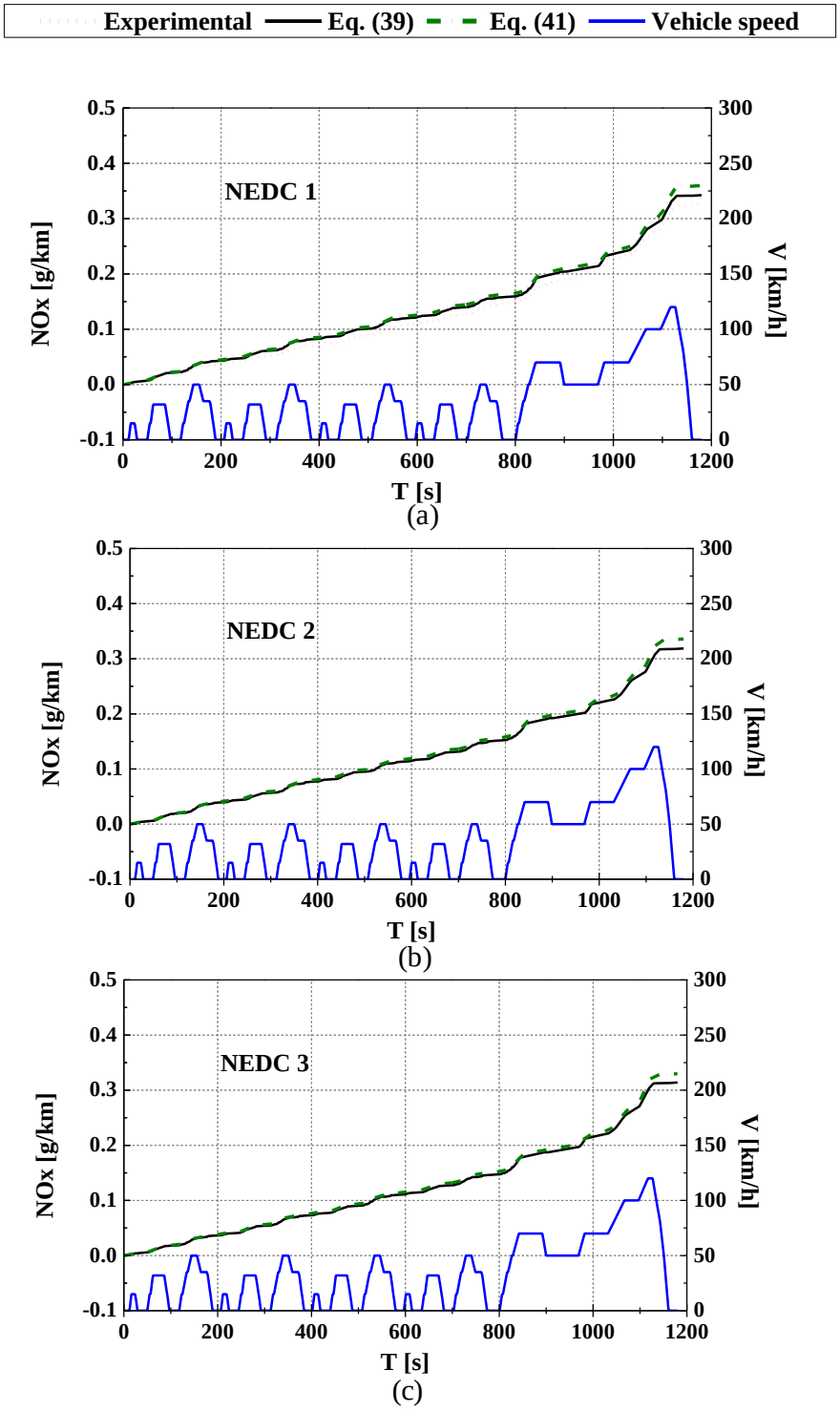


**Fig. 6.8** Time histories of the cumulated mass emissions of NOx for the three considered NEDCs, using either Eq. (6.1) or Eq. (6.2).

Fig. 6.8a, 13b and 13c report the experimental (red dotted lines) and predicted values of the cumulated NOx mass emissions, expressed in g/km, over the three considered NEDCs, using Eq. (6.1) (black lines) and Eq. (6.2) (green dotted-pointed lines).

It should be noted that the utilization of Eq. (39) leads to an improvement in the prediction of the cumulated NOx mass emissions, compared to Eq. (6.2), even though the values of R and RMS error, referring to the instantaneous NOx emissions, are of the same order of magnitude.

Although a high dispersion of the instantaneous NOx mass emissions can be observed in Fig. 6.7b, 12d and 12f for a limited number of points, their influence on the predicted cumulated NOx mass emissions is limited, as can be seen in Fig. 6.8.

## 6.5 Analysis of the computational time

It has emerged, from the previous analyses, that an important issue for real-time predictive model applications is the calculation time.

A detailed analysis of the calculation time and model accuracy of the three-zone thermodynamic model was made in [13],[14]. On the basis of the results reported in [13],[14], when the three-zone thermodynamic model and a phenomenological NOx model, based on the Zeldovich mechanism, are used, a calculation time of 1 ms is required on a Pentium D PC for the simulation of the whole engine cycle, using a computational step of 1 deg.

In the present approach, the three-zone model has only been used to evaluate $T_{bmax,main}$, thus it is not necessary to apply the three zone model to the whole cycle. This leads to a significant saving in computational time. Moreover, the computational performance can be further increased if the correlations reported in Eq.(6.1) or Eq.(6.2) are used to evaluate $T_{bmax,main}$, instead of applying the thermodynamic three-zone model.

The adoption of a semi-empirical NOx correlation, rather than a phenomenological approach, also leads to a significant reduction in the

computational time, that is, of the order of a few tens of a microsecond when the elaboration is performed on a PC, using Eq.(6.1) or Eq.(6.2) correlations to evaluate $T_{bmax,main}$.

# Chapter 7 Conclusion

A control-oriented semi-empirical model for the calculation of NOx emissions in diesel engines has been developed and assessed on two engines that feature different injection systems. The model has been developed with the aim of being implemented in the engine control unit (ECU) for model-based control tasks.

The model takes into account the maximum in-cylinder burned gas temperature during the combustion of the main pulse ($T_{bmax,main}$), the ambient gas-to-fuel ratio, the mass of injected fuel, the engine speed and the injection pressure. The evaluation of the burned gas temperature is based on a three-zone real-time diagnostic thermodynamic model, which has recently been developed by the authors. A simplified correlation to evaluate $T_{bmax,main}$ has also been developed for the cases in which the three-zone model cannot be applied.

The model has been tuned on the results of several tests carried out with a DoE methodology for a GM 2.0 $dm^3$ diesel engine, equipped with an Indirect Acting Piezoelectric injection system, for representative key-points of engine operation during an NEDC.

The higher $R$ value (0.98) and the lower RMS (0.021 mg/cyc·cyl) of the proposed model show a significant improvement in the prediction of the in-cylinder formed NOx mass, compared to previous approaches. The model was then applied to the same engine, but equipped with a Direct Acting Piezoelectric injection system, obtaining a similar accuracy to the calibration data ($R$ = 0.98 and RMS = 0.022 mg/cyc·cyl) and to a Euro 6 GM 1.6 $dm^3$ diesel engine equipped with a solenoid injection system, over a wide range of steady-state operating conditions, and the prediction accuracy resulted to be satisfactory ($R$ = 0.95 and RMS = 0.18 mg/cyc·cyl).

Finally, the performance of the model was also tested over urban and extra-urban phases of an NEDC. A good agreement was found between the predicted and experimental values of the instantaneous and the cumulated mass emissions.

**Conclusion**

The calculation time required by the semi-empirical model is of the order of some tens of a microsecond when the elaboration is performed on a Pentium D PC, and this means that the method is suitable for real time and control-oriented applications.

# Chapter 8 Appendix
## (Research in Tongji University)

# Study on working process and system thermal efficiency boundary for ICRC engine


## Abstract

The environment and energy issues are becoming more and more important. Carbon emissions nowadays, which were the standard of the industry, were limited due to greenhouse effect. The corresponding carbon emissions regulations and laws had been made in the automotive industry. Oxy-fuel combustion technique has been commercially used in power plants in order to capture the $CO_2$ from the exhaust gas, therefore, control the total amount of $CO_2$ in the atmosphere. ICRC (Internal Combustion Rankine Cycle) engine merges oxy-fuel combustion, water injection, Waste heat recovery technology and carbon capture. Water recycles the exhaust heat, and is injected into the cylinder to control the combustion temperature. Moreover, the injected water increases the mass of the working fluid so that the thermal efficiency increases.

Based on the First Thermodynamic Law, a thermodynamic analysis model of ideal ICRC is established, and water injection process is simplified. The effect of different working fluids and operation conditions on ICRC engine is investigated. The results show that $CO_2$ is most suitable as oxygenated diluent and working fluid in ICRC engine due to its less negative compression work and low specific heat. Therefore, air-cooling, low compression ratio and water-cooling, high compression ratio ICRC benches are developed base on a single-cylinder gasoline engine and a double-cylinder diesel engine. Spark plug and water injector, intake system, fuel system and control system are added. The effect of different compression ratio,

oxygen concentration and intake pressure on ICRC combustion and emissions are investigated. The results show that higher compression ratio, higher oxygen concentration and lower intake pressure are propitious to the thermal efficiency of ICRC engine. The thermal efficiency increases by 12.4% when compression ratio is 12.5. Moreover, water injection can decrease combustion unsteadily under high load, and also suppress knock and pre-ignition.

The investigation on the atomization and evaporation process of water is very important for ICRC engine because water is one of the most important working fluid. Based on a controllable active thermo-atmosphere combustor, the effect of different injection pressure, injection temperature and background temperature on water evaporation were investigated. Furthermore, the temperature of the working fluid on ICRC engine performance was investigated combined with bench experiments. Results show that higher injection pressure, injection temperature and in-cylinder temperature are propitious to better water evaporation. It can decrease the negative effect of water mist on combustion and increase the in-cylinder pressure near TDC, and therefore increase the thermal efficiency of ICRC engine. The indicated work increases by 11.45% when the water is injected on TDC with 120°C injection temperature.

Furthermore, an ideal engine thermodynamic model combined with a heat exchange model was developed to investigate the thermal efficiency upper boundary of this cycle. The best thermal efficiency of the whole ICRC system can reach to 58% when engine compression ratio is 14.

**Key Words:** IC engine; Oxy-fuel combustion technology; Rankine cycle; Water direct injection; Waste heat recovery.

## Nomenclature

A heat transfer area ($m^2$)

C specific heat capacity (J /(kg • K))

$C_r$ heat capacity ratio (-)

$d_e$ equivalent diameter of tubes (m)

$d_i$ internal diameter of tube (m)

$d_o$ outside diameter of tube (m)

D shell diameter (m)

h specific enthalpy (J/kg)

H overall heat transfer coefficient (W/($m^2$ • K)

$h_i$ Tube side heat transfer coefficient (W/($m^2$ • K)

$h_o$ shell side heat transfer coefficient(W/($m^2$ • K)

$j_h$ heat transfer factor (-)

L tubes length (m)

$L_b$ baffle spacing (m)

LVH lower heating value J/kg

m mass (kg)

$\dot{m}$, q mass flow rate (kg/s)

N tubes number (-)

NTU number of transfer units (-)

Pr Prandtl number (-)

Pt tubes center distance (m)

Q heat (J)

Re Reynolds Number (-)

T temperature (K)

u flow speed (m/s)

v volume ($m^3$)

W work (J)

η efficiency (%)

$\Delta T_m$ logarithmic mean temperature difference (K)

$\rho$ density (kg/m$^3$)

ε exchanger effectiveness (-)

***Abbreviations***

BTDC before top dead center

CR compression ratio (-)

IC internal combustion

ICRC internal combustion Rankine cycle

I/F intake charge/fuel

IMEP indicated mean effective pressure

NOx nitrogen oxides

ORC organic Rankine cycle

TEG thermoelectric generators

***Subscripts***

g exhaust gas

i indicated

in inlet

inj injection

min minimum

max maximum

out outlet

w water

1-6 state points in P-V diagram of an ICRC engine

## 8.1 Introduction

The combustion of fossil fuels for energy and transportation results in emission of greenhouse gases (main $CO_2$). To avoid the impact of the increasing greenhouse gases emission on climate, many new technologies have been developed. Oxy-fuel combustion integrated with carbon dioxide capture is one of the most effective technologies widely used in power generation industry [37]. High-purity oxygen instead of air is utilized during the combustion process. Therefore, the main components of exhaust gases are carbon dioxide and water vapor, and carbon dioxide is easily separated and captured [38]. Some parts of exhaust gas are usually recycled into the boiler in order to maintain a proper combustion temperature aiming to the acceptable limits of the boiler materials [39]. A large number of studies have investigated performance analysis and system optimization of oxy-fuel combustion [40],[41],[42].

Clean energy system merges oxy-fuel combustion and water injection [43],[44]. In this system, a large amount of high pressure recycled water is injected into the gas generator during the oxy-fuel combustion to increase the mass of the working fluid, and therefore the thermal efficiency increases. The emissions only include water and carbon dioxide, which are easily separated and recovered. This type of oxy-fuel combustion power-plant cycles is called internal combustion Rankine cycles (ICRCs). The thermal efficiency of an ICRC can reach 65% or more. The overall efficiency still can reach 58% when the energy cost of separating oxygen from air is considered [45].

Addition of water into the combustion process in IC engines is not a novel concept [46]. Water injection at ambient temperature is mainly employed in IC engines, such as an internal coolant [47], and NOx emissions reduction [48],[49], because water can reduce flame propagation and in-cylinder temperature. However, water injection provides a small contribution to improvement in thermal efficiency (increased by a maximum of 4%) [49]. Water is generally utilized to inhibit combustion and decrease in-cylinder temperature in these applications, thus the mass of water is limited due to the significant negative effects of excess water during

traditional air combustion process. Hence, thermal efficiency of the cycle benefits less from the evaporation of injected water.

Reciprocating engine versions of the ICRC was investigated for the potential application in automobiles [45]. The schematic figure of ICRC system is shown in Fig. 8.1. Oxygen mixed with EGR is inhaled into cylinder during intake stroke. Water recovered the thermal energy from the exhaust gas, and is directly injected into the cylinder during the combustion. Since combustion with higher oxygen concentration is more intense, more water can be added as working fluid to increase the work with less negative impact. The exhaust gas is a mixture of $CO_2$ and water vapor, which can be easily separated through condensation process at relatively low cost. In this way, high pure $CO_2$ can be captured and stored in a tank. Therefore, a high thermal efficiency combustion cycle with ultra-low emission is achieved. Thermodynamic analysis of an ICRC engine (CR = 9.2) without considering waste heat recovery was investigated by authors [45],[50]. Modeling results show that thermal efficiency can reach to 67% when water injection temperature reaches to 200$^{o}$C, and even more with higher water injection temperature.

As far as waste heat recovery are concerned, there are some typical approaches of recovering ICE waste heat including thermoelectric generators (TEG), organic Rankine cycle (ORC), six-stroke cycle IC engine and new developments on turbocharger technology [51]. TEG, ORC and turbocharger technology convert low-grade temperature heat from the exhaust to electrical or mechanical energy [52], while six-stroke cycle IC engine improves the thermal efficiency through absorbing waste heat energy directly and reducing the exhaust temperature [53]. Two-stroke extra heat recovery steam cycles are added after traditional four-stroke Otto or Diesel cycles. After exhaust gas is recompressed, water is injected into the cylinder. Energy from the trapped and recompressed exhaust gases is transferred to the injected liquid water, causing water to vaporize and the pressure and work increase. The ICRC engine combines the advantages of these methods, not only decreases the exhaust gas temperature by injecting water during the combustion, but also utilizes

exhaust gas to heat injected water for the remaining low-grade exhaust gas heat recovery.

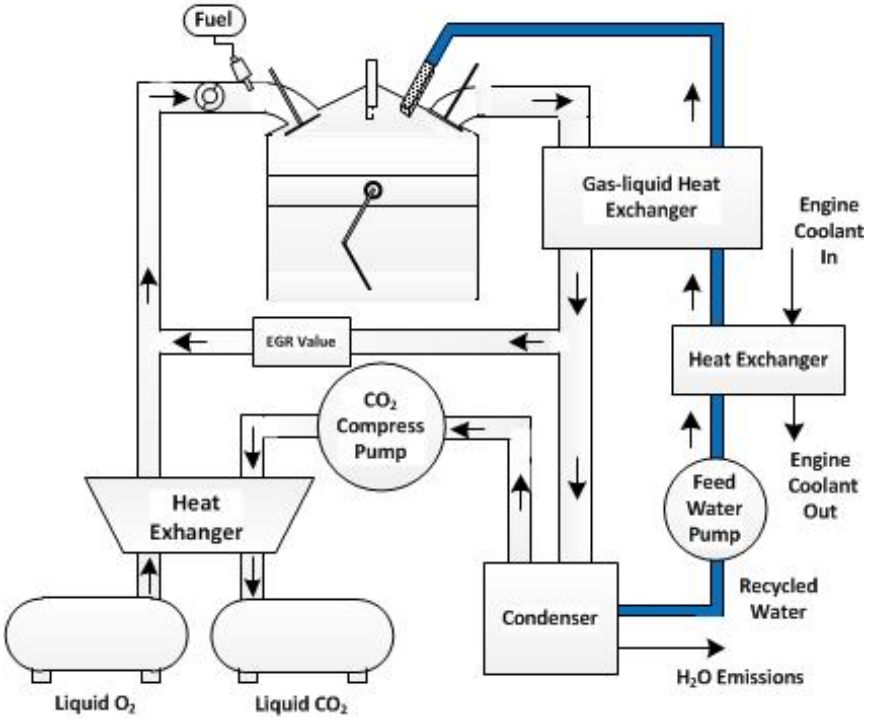


**Fig. 8.1** Schematic of ICRC system

An ideal engine thermodynamic model developed by the authors was employed to select the working fluid of an ICRC engine. Moreover, a self-designed prototype engine test bench with water cooling was built. Through changing the area of the combustion chamber and employing different operational boundaries, the effects of the working fluid on combustion and emission were investigated based on the ICRC engine.

Based on a controllable active thermo-atmosphere combustor, the effect of different injection pressure, injection temperature and background temperature on water evaporation were investigated. Furthermore, the temperature of the working fluid on ICRC engine performance was investigated combined with bench experiments.

The ideal engine thermodynamic model combined with a heat exchange model were developed to estimate the entire thermal efficiency of an ICRC engine, The

injected water temperature heated by exhaust gas was considered in the heat exchange model. Heat exchanger system was designed on the basis of engine operation conditions. The thermal efficiency boundaries of ICRC engine under different operation conditions and engine compression ratio were investigated.

## 8.2 Experiment setup and select of the working fuild

### 8.2.1 Experimental apparatus and procedure

#### 8.2.1.1 Experimental apparatus and procedure

The engine used for the experiment is based on a single-cylinder, air-cooling gasoline engine (Fig. 8.3a) and a double-cylinder, water-cooling diesel engine (Fig. 8.3b). The engines were retrofitted and fueled with propane through the KN3-2B type electronic control gas injector. A spark ignition, water injector and cylinder pressure transducer were installed in one of the cylinders. In this paper, one cylinder of the engine was employed for the experiment, whereas the other one was just operated as a load cylinder without combustion. The main specifications of the engines are given in Table 8.1. The area of the combustion chamber was changed by changing the thickness of the gland shim, and various compression ratios were therefore obtained in the second-generation system.

**Table 8.1** Specifications of test engines

| | |
|---|---|
| ***Engine type*** | SI engine |
| ***Number of cylinders*** | 2 |
| ***Bore/mm*** | 56.5(Fig. 8.3a)/95(Fig. 8.3b) |
| ***Stroke/mm*** | 49.5(Fig. 8.3a)/114(Fig. 8.3b) |
| ***Compression ratio*** | 9.2(Fig. 8.3a)/10.5-12.5(Fig. 8.3b) |
| ***Number of valves per cylinder*** | 2 |
| ***Displacement per cylinder [mL]*** | 124(Fig. 8.3a)/800(Fig. 8.3b) |
| ***Injection system*** | Intake manifold injection |
| ***Fuel*** | Propane |
| ***Cooling system*** | Water-cooling |

**8.2.1.2 Experimental setup and Test procedure**

The schematic diagram of the experimental setup is shown in Fig. 8.1. Two systems were used in the research, and Specifications of systems are listed in Table 8.1. The second-generation system is employed in the following chapter if not special specified. The engine was coupled to a FR100 eddy current dynamometer from the Italian API.com Company. $O_2$ and $CO_2$ were mixed to simulate the intake gas with EGR. Gas pipes were twined by a heating belt to maintain gas temperature stability, and the premixing chamber in the intake system kept the mixture gas homogeneous. The intake pressure was measured using a Bosch intake pressure sensor (20). To conveniently investigate the influence of water injection on combustion under specific temperature and pressure, the water was heated and pressurized in a stainless steel tube with a controllable built-in immersion heater. The heating temperature was controlled by thermocouples in the heater to avoid sub-cooled boiling of the water near the surface of the heater. The water injector is a solenoid diesel injector made by the FAW Company. The operating conditions of the engine were monitored using a photoelectric encoder (3), cylinder pressure sensor (4), lambda sensor (8) and throttle position sensor (9). The in-cylinder pressure was measured using a Kistler 6052C piezoquartz pressure sensor. The cylinder pressure signal was amplified through a Kistler 5018A charge amplifier and collected by a NI 6250C acquisition card. The photoelectric encoder was installed with the crankshaft to record the crank angle signal. The ECU controlled the injectors, spark plug and other actuators based on that signal. The emissions were measured using an FGA-4100 Five-gas ($O_2$, $CO_2$, CO, HC, NOx) emissions analyzer from the Foshan Company.

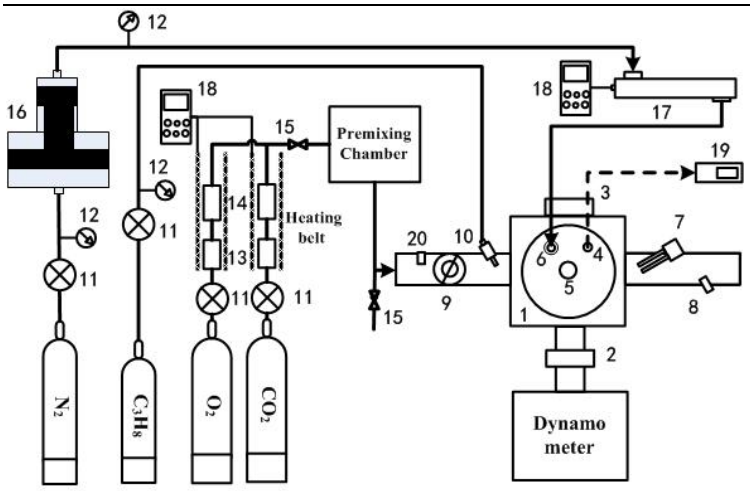


**1 Engine; 2 Coupling; 3 Photoelectric encoder; 4 Pressure transducer; 5 Spark plug; 6 Water injector; 7 Emission analyzer; 8 Lambda sensor; 9 Throttle; 10 Propane nozzle; 11 Pressure reduction valve; 12 Pressure gage; 13 Throttle valve; 14 Flowmeter; 15 Ball valve; 16 Pressure accumulator; 17 Water heating rail; 18 Temperature controller; 19 Charge amplifier;20 Intake pressure sensor**

**Fig. 8.2** Schematic of the test bench dedicated to ICRC engine

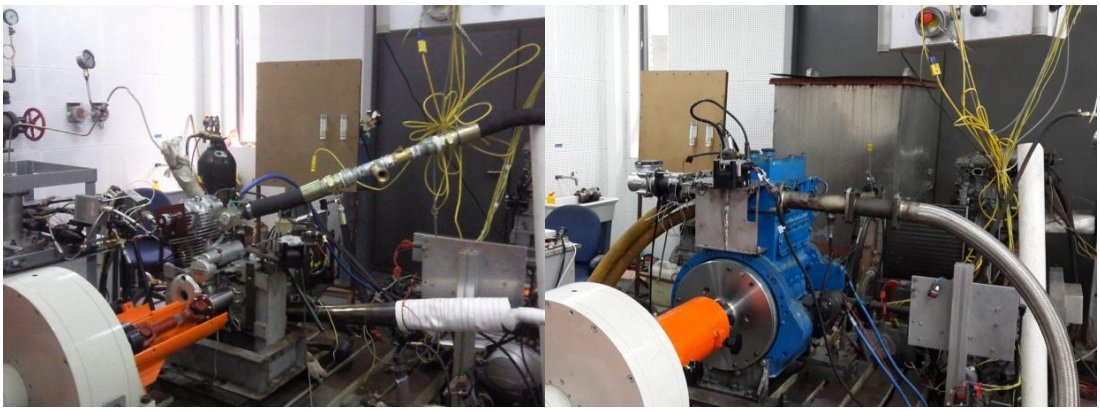

(a) 1st-generation (b) 2st- generation

**Fig. 8.3** ICRC test system

The schematic of the water rail is detailed in Fig. 8.4. Water flowed into the rail from the pressure accumulator through the water inflow end and leaves the rail to the injector through water outflow end. A built-in immersion heater was installed to heat water in a stainless steel tube. The heating temperature was controlled by thermocouples in the heater to avoid sub-cooled boiling of the water near the surface of the heater. The water temperature was offered from the right thermocouple closed to water outflow end in the rail. Water was pressured up to

20~25MPa in the rail and the boiling point of water at this pressure was around 330°C, much higher than the highest water injection temperature (120°C) in this paper, which guaranteed the water at liquid state in the injection system.

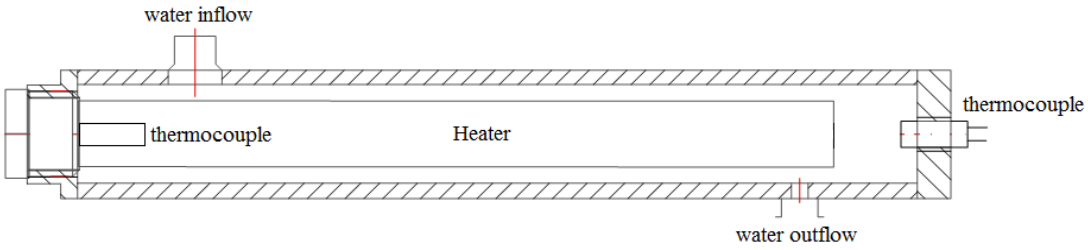


**Fig. 8.4.** Detailed schematic of the water rail

The engine was started with an intake of air and then changed to the oxy-fuel model when the engine and dynamometer were synchronous. Measurements were gathered after the operational condition of the engine became stable. One hundred cycles, including 50 continuous water injection cycles, were collected under each condition. The no water injection cycles (dry cycles) and water injection cycles were distinguished by the water injection signal recorded in the acquisition card.

#### 8.2.1.3 Error analysis

In the present study, the procedure applied to evaluate the experimental uncertainties was based on the root mean square method. The error analysis of the derived quantities, such as the indicated work and indicated thermal efficiency, were estimated based on an error analysis using the real measurement values. The measurement ranges and relative measurement errors are listed in Table 8.2.

**Table 8.2** Measurement ranges and relative measurement errors

| ***Instrument*** | ***Measurment range*** | ***Relative error (%)*** |
|---|---|---|
| ***Inlet gas pressure*** | 0-0.2 MPa | ±0.25 |
| ***In-cylinder pressure*** | 0-10 MPa | ±0.5 |
| ***$O_2$ concentration*** | 0-80% vol | ±1 |
| ***Propane flow meter*** | 0-25 L/min | ±2.5 |
| ***Crank angle encoder*** | - | ±0.1 |

| | | |
|---|---|---|
| ***Engine speed*** | 0-5000r/min | ±1 |
| $W_i$ | - | ±0.5 |
| $\eta_i$ | - | ±2.9 |
| ***Emissions (HC,NOx)*** | HC (0-9999ppm); NOx (0-5000ppm) | ±5 |

### 8.2.2 Model description

Fig. 8.5(a) illustrates the in-cylinder pressure of an ICRC engine under both water injection cycles and no water injection cycles (dry cycles), and data comes from the previous experiments [54]. Fig. 8.5(b) illustrates the simulant in-cylinder pressure of a one-dimensional ICRC engine model using a turbulent combustion model, and the operation conditions of Fig. 8.5(a) and Fig. 8.5(b) are the same. It shows form both Fig. 8.5(a) and Fig. 8.5(b) that water injection increases the mass of the working fluid and hence the in-cylinder pressure increases. As shown in Fig. 8.5 (a), Fig. 8.5 (b) and the comparisons of experiment and ideal thermodynamic model in [50] [55], the increase of the in-cylinder pressure is derived from the injected water evaporation and the increase of the working fluid. In the previous studies of authors, the injected water indeed has affected the combustion process and the analyses about combustion optimization and the influences of injected water on combustion process can be detailed in [54],[56]. But through combustion and control optimization in engineering, water can be evaporated faster and increase the mass of working fluid to improve thermal efficiency. Hence, after combustion optimization, thermodynamic effect between injected water and the original working fluid is most important for the thermal efficiency of this cycle. In this paper, estimating the upper bound on the potential thermal efficiency boundary of an ICRC engine is the main aim. Hence, in order to support a theoretical analysis for ideal thermal efficiency bound of ICRC, thermodynamic analysis between injected water and the original working fluid is focused on in this paper. Therefore P-V diagram of an ICRC engine is simplified to an Otto cycle combined with water injection process, which is shown in Fig. 8.6(a). Cycle 1-2-3-4-1 is a traditional Otto cycle in which processes 1-2, 3-4 are assumed as adiabatic processes. Water is injected in state point 3 (end point of

combustion) and is assumed to evaporate instantaneously. Due to vaporization of the injected water, the in-cylinder pressure will rise to state point 5 and the new combined cycle (1-2-5-6-1) is formed. Moreover, the injected water can absorb combustion heat and evaporate to increase in-cylinder pressure. Hence, the in-cylinder temperature after water injection is lower than the in-cylinder temperature before water injection [50], and the in-cylinder temperature change diagram was shown in Fig. 8.6(b).

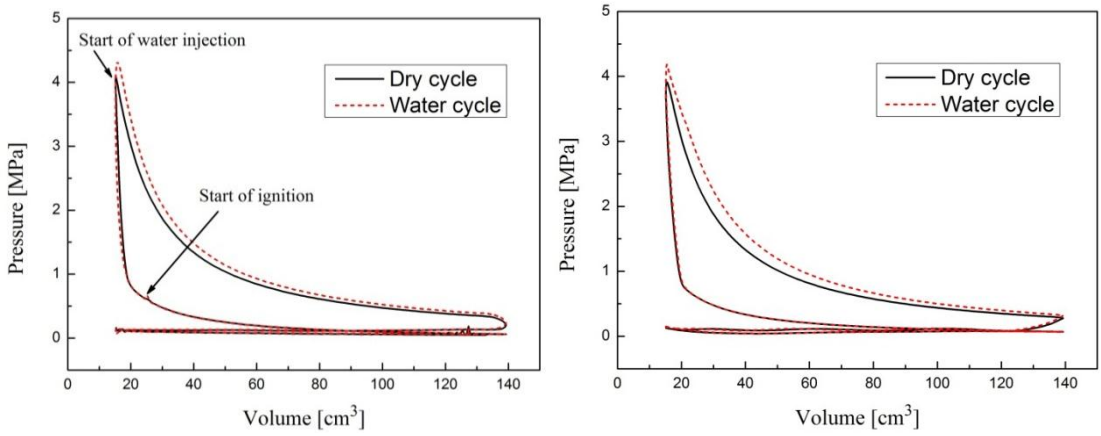


**(a) Experimental** **(b) Simulant diagram of a one-dimensional model**

**Fig. 8.5. Experimental and Simulant P-V diagram of an ICRC engine**

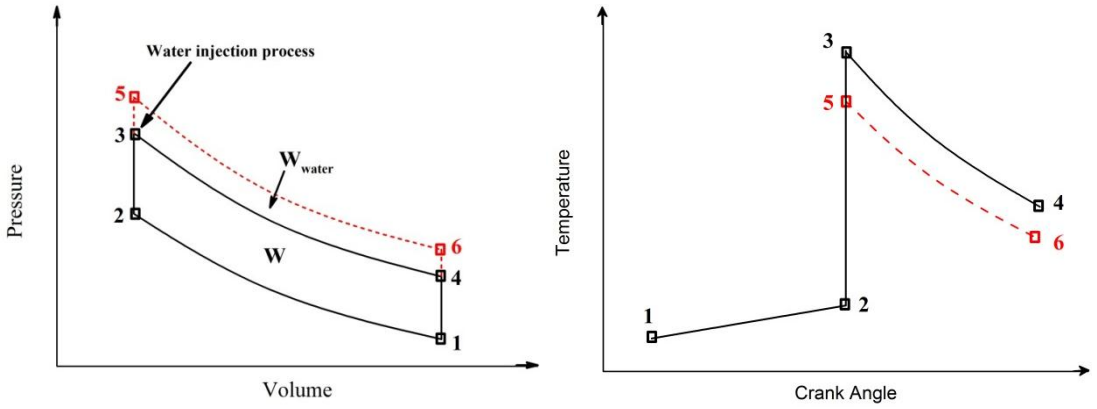


**(a) P-V diagram** **(b) T-Crank Angle diagram**

**Fig. 8.6. Simplified P-V diagram and T-Crank Angle diagram of an ideal ICRC**

Traditional adiabatic process (1-2 and 5-6) and constant-volume process (2-3) are solved by STANJAN software of Reynolds [57].

According to the First Law of Thermodynamics, the thermodynamic process after water injection (3-5) is calculated with Eq. (8.1) and (8.2) below, assuming instantaneous water evaporation:

$$\mathrm{m}_{water} \cdot h_{water} = \mathrm{m}_5 \cdot h_5 - \mathrm{m}_3 \cdot h_3 \tag{8.1}$$

$$\mathrm{m}_5 = m_{water} + m_3\ ,\ u_5 = C_{v5} \cdot T_5,\ u_3 = C_{v3} \cdot T_3 \tag{8.2}$$

where $m_{water}$ and $h_{water}$ are the mass and specific enthalpy of the injected water, and $m_n$ and $h_n$ are the trapped mass and specific enthalpy in the cylinder of state point n (Fig. 8.6). $C_{vn}$ is specific heat at constant volume of state point n calculated based on the temperature and mass fraction of the species of state point n. Thermochemical properties of the species in this paper come from NIST-JANAF Thermochemical Tables [57].

On the basis of the Eq. (8.1) and (8.2), the temperature of state point 5 ($T_5$) could be determined.

$$T_5 = \frac{m_3 C_{v3} T_3 + m_{water} h_{water}}{m_5 C_{v5}} \tag{8.3}$$

Hence, the pressure of state point 5 ($P_5$) could be derived from the application of the ideal gas law:

$$P_5 = \frac{\left(\frac{m_3}{M_3} + \frac{m_{water}}{M_{water}}\right) R T_5}{V_5} \tag{8.4}$$

where $m_3$ *and* $m_{water}$ the molar mass of trapped mass (state point 3, kg/mol) and water vapor respectively (kg/mol), $m_3$ *and* $m_{water}$ is the mass of trapped mass (state point 3, kg) and water vapor respectively (kg), $V_5$ is the volume of state point 5 ($m^3$), and $R$ is the mole gas constant (J/(mol • K)).

In an ICRC engine, water injection pressure is high in order to fast evaporation rate and keep the water at liquid state under high temperature. Hence, the pump energy for water pressurizing must be considered. It is expressed as:

$$\mathrm{W}_{pump} = m_{water} \cdot (P_{inj} \cdot v_{inj} - P_0 \cdot v_0)/\eta_{pump} \tag{8.5}$$

where $W_{pump}$ is the compression work of pump for water, $P_{inj}$ and $v_{inj}$ are the pressure and specific volume of water after pressure process, while $P_0$ and $v_0$ are the pressure and specific volume of water under initial status. $\eta_{pump}$ is the pump efficiency.

The energy used for water heat is gained from exhaust gas, and does not consume external energy. Performance and efficiency of heat exchange will be analyzed and discussed in the later chapters.

Since expansion stroke (5-6) is also assumed to be adiabatic, the entire work output and thermal efficiency for each cycle could be expressed as following:

$$W_i = W_{5-6} - W_{1-2} - W_{pump} \tag{8.6}$$

$$\eta_i = W_i/(m_{fuel} \cdot LVH_{fuel}) \tag{8.7}$$

where $m_{fuel}$ is the fuel consumption per cycle, $LHV_{fuel}$ is the low heating value of fuel.

### 8.2.3 Boundary conditions

The initial conditions, assumptions and constraint conditions for the ICRC engine thermodynamic model are listed in Table 8.3, and are based on pervious experiments [18]. The engine parameters are listed in Table 8.1. The water injection pressure (35MPa) is much higher than the saturated vapor pressure of water from 80°C~160°C, and the water can therefore be maintained in the liquid state before injection. The oxygen concentrations is exceeds 40% because $CO_2$ has a strong side effect on flame propagation, and lower oxygen concentrations may lead to the instability of the combustion process, especially when water is injected. The in-cylinder temperature at state point 4, where the expansion stroke ends at BTDC, was set above 330 °C for two reasons: to keep the exhaust gas temperature high enough for the recycled water heating and to keep the temperature of the water vapor above its dew point to avoid potential equipment damage due to droplet erosion.

**Table 8.3** Initial conditions, assumptions, and constraints

| | |
|---|---|
| ***Initial conditions*** | |
| Fuel | $C_3H_8$ |
| Initial temperature | 300K |
| Initial intake charge mass | 0.79bar |
| Intake composition | 40%~70% $O_2$ ($CO_2$/$N_2$/Ar) |
| Fuel mass | 52.7mg |

| | |
|---|---|
| Compression ratio | 10.5 |
| Water injection temperature | 80°C~160°C |
| Water injection pressure | 35MPa |
| Water injection mass | 20g - upper limit value |
| Water injection timing | 360°CA |
| ***Assumptions*** | |
| Water injection duration | Instantaneous at 360°CA |
| Water and air mixing | Instantaneous at 360°CA |
| Water vaporization | Instantaneous at 360°CA |
| $\eta_{pump}$ | 50% |
| Heat transfer to cylinder walls | None |
| ***Constrains*** | |
| Temperature at state point 4 | ≥330°C |

.

### 8.2.4 Effect of different intake charges on the thermal efficiency of the ICRC engine and select of the working fluid

The closed cycle technique is employed in the ICRC engine and the components of the intake charge include oxygen and diluent (employed for the control of the rapid combustion rate in the oxy-fuel combustion). Hence, the intake charge can be flexibly charged to achieve higher thermal efficiencies. Different intake charge compositions were investigated, and the appropriate diluent was determined for the ICRC engine

1. $O_2$+EGR (used $CO_2$ to simulate EGR)
2. $O_2$+$N_2$
3. $O_2$+Ar

These three intake charge compositions represent: 1. Oxy-fuel combustion, 2. oxygen-enriched combustion and 3. Ar/$O_2$ engine.

Figure 3 shows the work ratio under the different intake charge compositions, and Table 2 lists the b conditions and thermodynamic parameters of these test conditions. The operation conditions are referred to the experiments. The intake pressure was 0.79bars, the fuel mass was 52.7mg, and the oxygen concentration was 60%. Cases 1 and 2 were the dry (without water injection) and water (with water

injection) cycles, respectively, with $CO_2/O_2$ as the intake charges. Cases 3 and 4 were the dry (without water injection) and water (with water injection) cycles, respectively, with $N_2/O_2$ as the intake charge respectively. Cases 5 and 6 were the dry (without water injection) and water (with water injection) cycles, respectively, with $Ar/O_2$ as the intake charge. Fig. 8.7 shows that the output work of the water cycle is obviously more than the output work of the dry cycle, and the steam work derived from the injected work is accounted for a large proportion of the output work, which is the reason why this cycle is referred to as a special type of Rankine cycle. Moreover, the output work of the dry cycle using Ar as the diluent is greater than the output work of other dry cycle conditions, because Ar is monatomic molecule and the specific heat ratio (1.67) is more than the specific heat ratio of $CO_2$ (1.33) and $N_2$ (1.4). However, the output of the water cycle using $CO_2$ is most under those water cycles. According to Table 8.4, the thermal efficiency of case 2 is the highest because the fuel mass is the same. Table 8.4 also shows that the increase in the in-cylinder pressure and the decrease in the in-cylinder temperature due to water injection are the highest.

The pressure of point 5 can be calculated using:

$$P_5 = \frac{\left(\frac{m_3}{M_3} + \frac{m_{water}}{M_{water}}\right) R \frac{n_3 C_{v3} T_3 + m_{water} h_{water}}{n_5 C_{v5}}}{V_5} = \frac{n_5 R \frac{n_3 C_{v3} T_3 + m_{water} h_{water}}{n_5 C_{v5}}}{V_5} \quad (8.8)$$

$$= \frac{n_3 R T_3}{V}\left(\frac{C_{v3}}{C_{v5}}\right) + \frac{m_w h_w R}{C_5 V} = P_3\left(\frac{C_{v3}}{C_{v5}}\right) + \frac{m_w h_w R}{C_{v5} V}$$

Fig. 8.8 shows that the special heat ratio of $CO_2$ is higher than the special heat ratios of $N_2$ Ar and $H_2O$. Therefore, the value of $C_{v3}/C_{v5}$ in Equation 8 under the $CO_2$ condition is larger than 1, whereas the value is the smallest under the Ar condition due to lower special heat ratio of Ar. Hence, the increase in the in-cylinder pressure due to water injection is greater under the $CO_2$ condition, whereas the increase is least under the Ar condition. Moreover, during the heat exchange between the water and original working fluid, $H_2O$ vapor can gain more thermal energy from the original working fluid under the Ar condition due to lower special heat ratio of Ar. Therefore, it can be seen in the Table that the work ratio of water vapor under Ar is

highest. However, $H_2O$ vapor (triatomic molecule) is, unfortunately, a poorer working fluid than Ar (monoatomic molecule). Therefore, the increase in the expansion work under the Ar condition is less than the increase in the expansion work under the $CO_2$ condition. Moreover, the negative compression work under the Ar condition is more than the compression work under the $CO_2$ condition. Hence, the thermal efficiency under the $CO_2$ condition is higher than the thermal efficiency under the Ar condition.

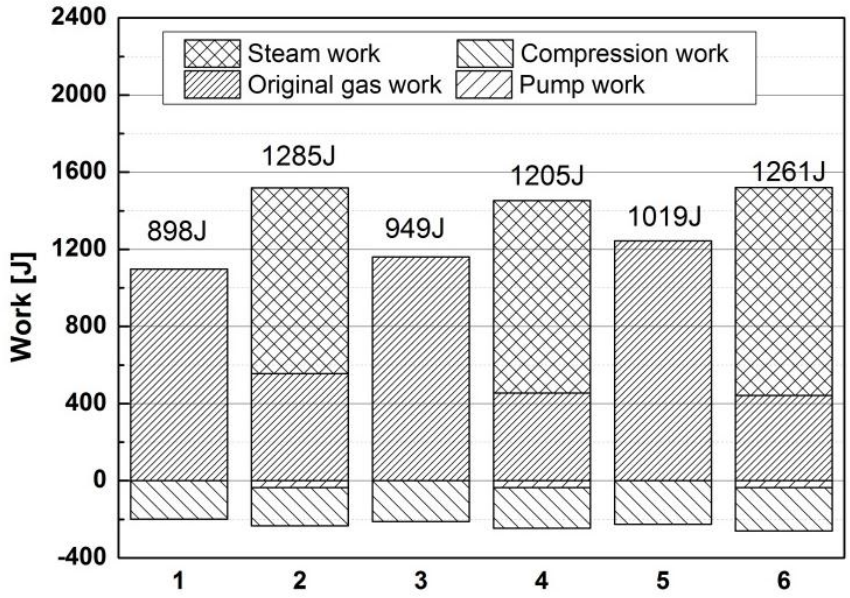


**Fig. 8.7** Work ratio under different intake charge compositions

**Table 8.4** Boundary conditions and thermodynamic parameters under different intake charge compositions

| ***Test condition*** | Case 1 | Case 2 | Case 3 | Case 4 | Case 5 | Case 6 |
|---|---|---|---|---|---|---|
| ***Diluent*** | $CO_2$ | $CO_2$ | $N_2$ | $N_2$ | Ar | Ar |
| $m_{water}/m_{intake}$ | 0 | 1 | 0 | 1 | 0 | 1 |
| ***Thermal efficiency [%]*** | 33.8 | 49.8 | 35.7 | 44.8 | 38.3 | 48.7 |
| ***P3，P5 [MPa]*** | 7.19 | 10.59 | 8.13 | 9.94 | 8.96 | 10.79 |
| ***T3，T5 [K]*** | 2531 | 1102 | 2844 | 1177 | 3109 | 1161 |
| ***Compression work[J]*** | -199 | -199 | -211 | -211 | -225 | -225 |
| ***Pump work [J]*** | 0 | -35 | 0 | -35 | 0 | -35 |
| ***Expansion work[J]*** | 1097 | 1519 | 1160 | 1452 | 1243 | 1521 |
| ***Steam work/output work*** | 0 | 75% | 0 | 83% | 0 | 86% |

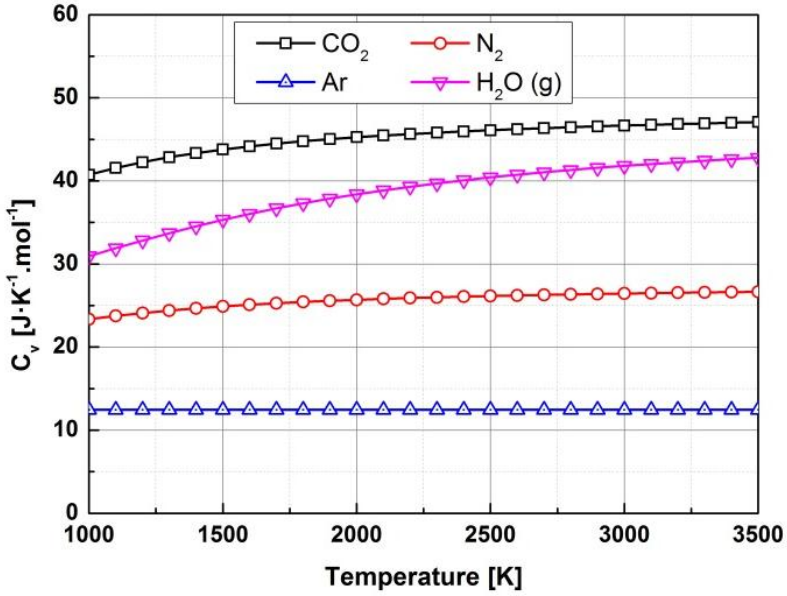


**Fig. 8.8** Special heat ratio of different working fluids

Fig. 8.9 shows that the effect of the different working fluids on the thermal efficiency of ICRC engine. Fig. 8.9 shows that the thermal efficiency increases with the increase in the water injection mass due to the increase in the expansion work. Moreover, the enthalpy and energy derived from the injected water increases with the increase of water injection temperature, and the thermal efficiency is therefore higher with a higher water injection temperature. Fig. 8.9 shows that the thermal efficiency under the Ar condition is higher than the thermal efficiency under the $N_2$ and $CO_2$ conditions when the water injection mass is zero (dry cycle), because Ar has a higher special heat ratio. According to the previous analysis, $H_2O$ vapor is a poorer working fluid than Ar, but $H_2O$ replaces Ar as the working fluid in the water cycle (the cycle with water injection). Moreover, more heat energy is transported from the original gas to the water vapor, therefore, the increase in the thermal efficiency derived from water injection under the Ar condition is the smallest. Because $CO_2$ is a poorer working fluid than Ar and $N_2$ for expansion work, the increase in the water vapor ratio is benefit for the increase in the thermal efficiency under the $CO_2$ condition. Moreover, the negative compression work under the $CO_2$ condition is less, and the thermal efficiency under the $CO_2$ condition therefore is even higher than the thermal

efficiency under the Ar condition with a large amount of water injection mass. The thermal efficiency reaches 58.2% when the ratio of the water injection mass to the original gas mass is 1.58.

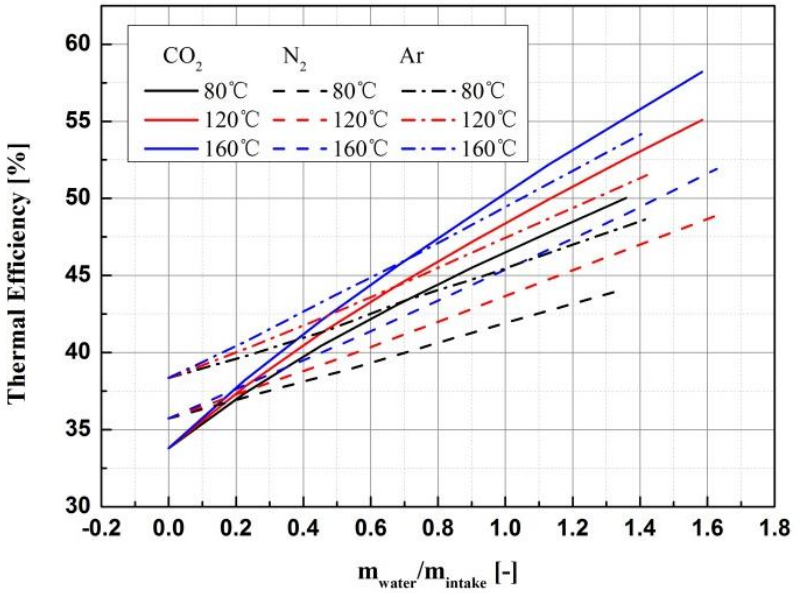


**Fig. 8.9** Thermal efficiency of the ICRC engine under different working fluids

According to the previous analysis, $CO_2$ is a suitable working fluid for the ICRC engine due to the less negative compression work, and $CO_2$ (EGR) is therefore chosen for the ICRC engine in the following chapters.

## 8.3 Effects of the working fluid on the combustion of ICRC engine

The operating conditions are listed in

Table **8.5**. One hundred cycles, including 50 continuous water injection cycles, were collected under each condition. The no water injection cycles (dry cycles) and water injection cycles were distinguished by the water injection signal recorded in the acquisition card.

**Table 8.5.** Operating conditions

| | |
|---|---|
| ***Speed [r/min]*** | 1500 |
| ***$O_2$ volume fraction [%]*** | 45~55 |
| ***Compression Ratio [-]*** | 10.5-12.5 |
| ***Intake pressure [kPa]*** | 72-101 |
| ***Water injection duration [ms]*** | 1-7 |

| *Injected water Temperature [°C]* | 120 |
|---|---|

### 8.3.1 Effect of the intake pressure on the combustion and emission

There are two working fluids in the ICRC engine. One is the mixture gas ($O_2$, EGR and fuel) inhaled in the intake stroke, and the other is the water injected near the top dead center. Both influence the performance and emission of the ICRC engine. Moreover, it is convenient for the ICRC engine to change its intake pressure during the operation because a closed inlet system is employed in the ICRC engine. Hence, the effect of the intake pressure ($P_i$) on the combustion and emission are examined in this section. The engine speed was set to 1500 r/min with an ignition angle of 35°CA BTDC. The water injection pressure was 38MPa, and the water injection time was 0°CA BTDC. The fuel mass was 52.7 mg, and the compression ratio was 10.5. The oxygen volume fraction was 50%.

Fig. 8.10 (a) shows the effect of different intake pressures on the in-cylinder pressure without water injection. The mass of the working fluid into the cylinder increases with the increase in intake pressure, and therefore the in-cylinder pressure under compression and expansion stroke is higher under the higher intake pressure. Moreover, the peak in-cylinder pressure increases with the increase in intake pressure. Oxygen is excessive for fuel in the ICRC engine. Hence, when the fuel mass is fixed, the mixture became richer with the decrease in the intake pressure and intake charge, and the combustion rate increases. Therefore, as shown in Table 8.6, the phase of the peak in-cylinder pressure advances with the increase in the intake pressure. Fig. 8.10 (b), (c) and (d) show the in-cylinder pressure comparison of dry and water cycles under the different intake pressures. According to the previous analysis, the combustion rate increases with the increase in intake pressure, and therefore the in-cylinder temperature increases. The evaporation rate of the injected water increases due to the higher background temperature, and the more rapid evaporation causes a less negative impact of the water mist on the combustion process [58]. Furthermore, more rapid evaporation of the injected water rapidly increases the mass of the working fluid, and the in-cylinder pressure increases. Hence, Fig. 8.10 shows that the peak in-cylinder pressure and expansion pressure

clearly increase as a result of the water injection under the lower intake pressure. The increased proportion of the peak in-cylinder pressure increases from 0.5% ($P_i$ = 101kPa) to 3% ($P_i$ = 72kPa). Table 8.6 shows that the indicated work increases from 825 J to 852 J (3.3%) due to the water injection under the 101 kPa intake pressure. The increased proportion of the indicated work is improved to 5.4% when the intake pressure deceases to 72 kPa. However, the indicated work decreases with the decrease in intake pressure because the mass of the working fluid into the cylinder decreases.

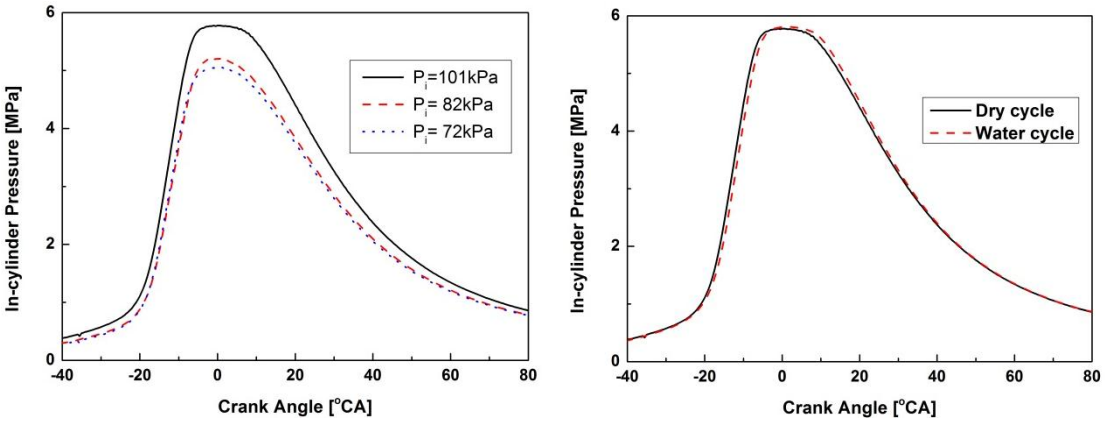


(a) Dry cycles under different intake pressure (b) $P_i$ = 101kPa

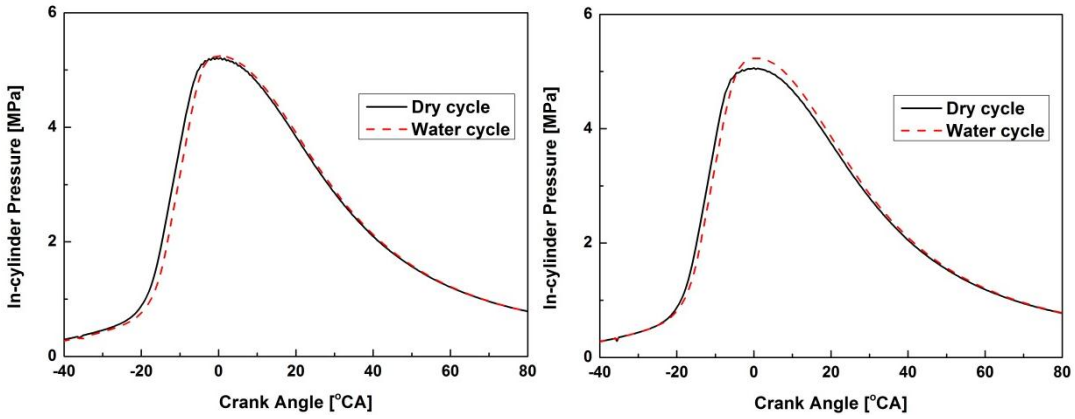


(c) $P_i$ = 82kPa (d) $P_i$ = 72kPa

**Fig. 8.10** Effect of water injection on the in-cylinder pressure under different intake pressures

**Table 8.6** Combustion characteristics under different intake pressures

| ***Intake preussre [kPa]*** | **101** | | **82** | | **72** | |
|---|---|---|---|---|---|---|
| ***Water injection duration [ms]*** | 0 | 1 | 0 | 1 | 0 | 1 |
| ***Pmax [MPa]*** | 5.78 | 5.81 | 5.18 | 5.25 | 5.06 | 5.22 |
| ***φ(Pmax) [°CA ATDC]*** | 0 | 1 | -1 | 0 | -1.5 | 0 |
| ***$W_i$ [J]*** | 825 | 852 | 742 | 779 | 720 | 765 |

Fig. 8.11 (a) illustrates the indicated work of the water and dry cycles under different intake pressures. In the dry cycles (water injection duration = 0 ms), the mass of the intake charge decreases with the decrease in the intake pressure, and the indicated work decreases. Water injection increases the mass of the working fluid in the cylinder, and the indicated work increases. The indicated work increases under the 82 kPa intake pressure and reaches a maximum (785 J) when the water injection duration increases from 1 ms to 3 ms. The indicated work decreases when the water injection duration increases from 3 ms to 7 ms because excess water causes significant negative effects on the combustion process. When the intake pressure was 72 kPa, the indicated work tends to first rise then fall as the water injection duration increases, identical to that under the 82 kPa intake pressure operation condition. An optimal water injection duration for the highest indicated work exists in those two cases. It is interesting that the optimal indicated work of 72 kPa (786J, 5ms) is more than the optimal indicated work of 82 kPa (785J, 3ms), although the mass of the intake charge under the 72 kPa intake pressure is less than the mass under the 82 kPa intake pressure. This occurred because the negative compression work decreases as the intake pressure decreases. Moreover, as mentioned before, the mixture gas became richer and the combustion temperature increases under the lower intake pressure, and therefore the indicated work derives from water evaporation increases as the in-cylinder temperature increases. The supplement of the working fluid through water injection can avoid the increase in

the negative compression work in an ICRC engine, and therefore higher indicated work and thermal efficiency can be obtained under lower intake pressures.

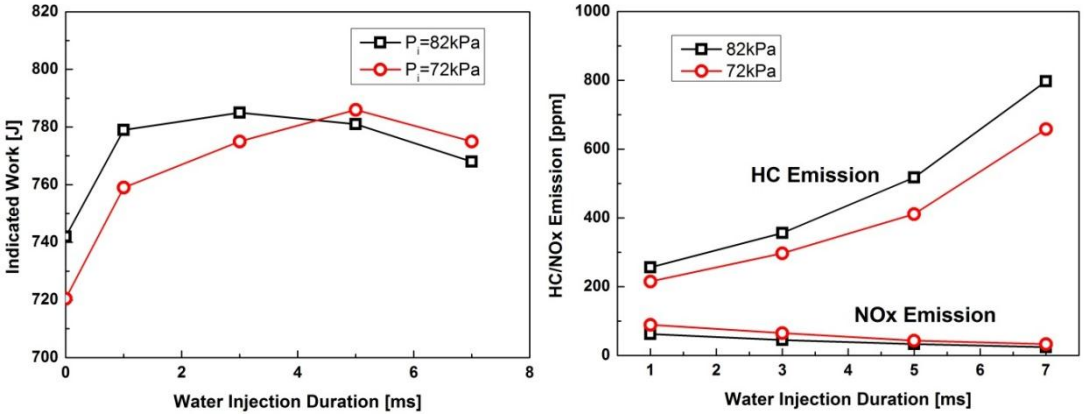


(a) indicated work (b) HC/NOx emission

**Fig. 8.11** Effect of water injection on the indicated work and HC/NOx emission under different intake pressures

Fig. 8.11 (b) shows the HC/NOx emission under different intake pressures in the ICRC engine. In the ideal state, NOx emission should not exist in oxy-fuel combustion. The reason is that the purity of industrial $O_2$ and $CO_2$ production employed in the experiment is approximately 99%, and the remaining gas is mainly $N_2$. With the increase in the water injection duration, more injected water evaporates and absorbs more heat energy, and the in-cylinder temperature therefore decreases. Temperature is the main factor for NOx formation; hence, an increased water injection duration will lead to lower NOx emissions. Furthermore, more injected water increases the probability of local incomplete combustion and leads to higher HC emissions. As mentioned before, the Fuel/ ($O_2$+$CO_2$) ratio increases and the combustion temperature is higher under low intake pressures. Hence, HC emissions decrease and NOx emissions increase as the intake pressure decreases. However, compared with the HC emissions, the NOx emissions remain low because injected water effectively reduces the in-cylinder temperature.

### 8.3.2 Effect of oxygen concentration on the combustion and emission

One of the most significant differences in ICRC engines is that oxygen and EGR replaces air as the intake charge and oxidant. Therefore, an ICRC engine can control the oxygen concentration of intake charge conveniently, which offers another approach to effectively control the combustion compared to conventional engines. Moreover, water injection integrated with oxy-fuel combustion is employed in ICRC engines, and therefore the combustion characteristics of ICRC engines are also different from oxygen-enriched combustion. In this section, the effects of oxygen concentration on the characteristics of the combustion and emissions for an ICRC engine are investigated, and the OF value was employed to indicate the oxygen volume fraction.

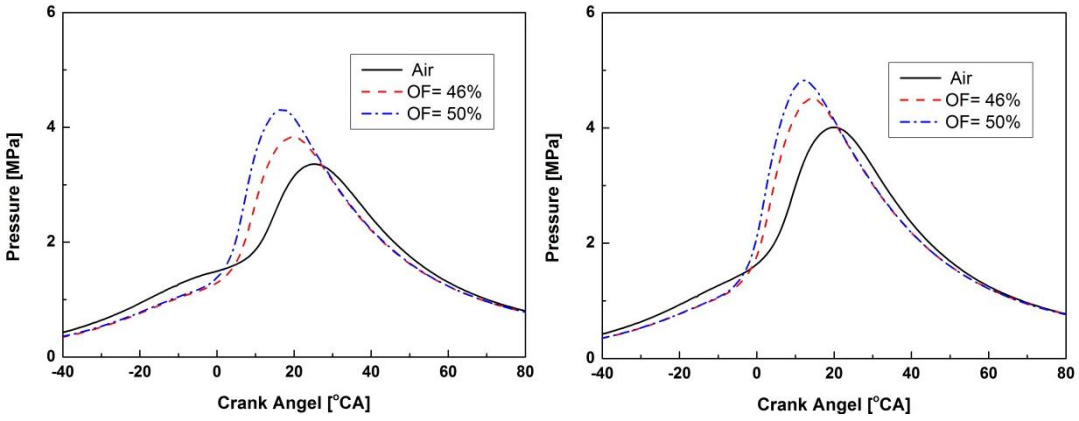


(a) 10°CA BTDC (b) 15° CA BTDC

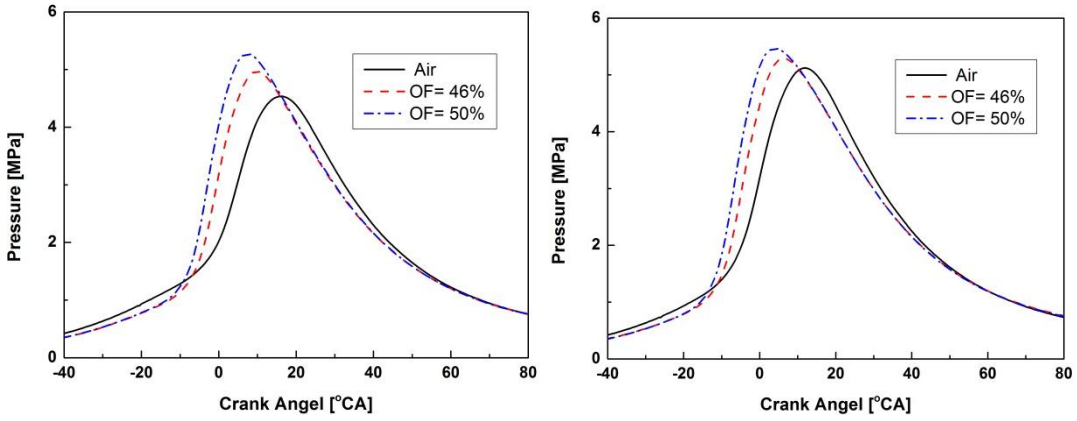


(c) 20°CA BTDC (d) 25°CA BTDC

**Fig. 8.12** Effect of oxygen concentration on the in-cylinder pressure under different spark timings (dry cycle)

Fig. 8.12 shows the effects of oxygen concentration on the in-cylinder pressure under different spark timings (dry cycle). The engine speed was set to 1500 r/min with ignition angles at 10-35°CA BTDC. The fuel mass was 49.7 mg. The compression ratio was 10.5, and the intake pressure was 101 kPa. Fig. 8.12 shows that the in-cylinder pressure under air combustion is higher than the pressure under oxy-fuel combustion before the spark ignition because the components of the intake charge under oxy-fuel combustion are oxygen and carbon dioxide. Carbon dioxide is a triatomic molecule and has lower specific heat ratio (k = 1.33) than nitrogen (diatomic molecule, k = 1.40) in air. Hence, the compression pressure of the oxygen and carbon dioxide mixture is lower than the pressure of air as the intake charge. Moreover, the combustion rate and the peak in-cylinder pressure increases as the oxygen volume fraction increased. The peak in-cylinder pressure increases from 3.36 MPa (air) to 4.32 MPa (OF=50%) under the 10°CA BTDC spark ignition timing.

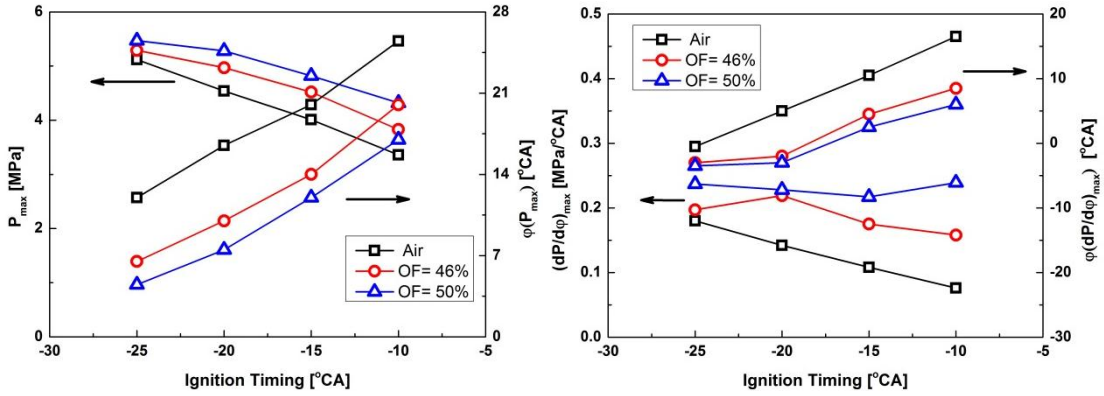


(a) Peak in-cylinder pressure (b) Pressure rise rate

**Fig. 8.13** Effect of oxygen concentration on the combustion under different spark timing (dry cycle)

Fig. 8.13 (a) shows the effect of the oxygen concentration on the peak in-cylinder pressure and the corresponding phase under different spark timings (dry cycle). The peak in-cylinder pressure under oxy-fuel combustion is higher than the pressure of air combustion and increases as the oxygen volume fraction increases because the reaction rate and flame propagation speed under oxy-fuel combustion are faster, and the heat release rate derived from the fuel combustion therefore

increases. The trend in the faster combustion rate increases as the oxygen volume fraction increases. Hence, the phase of the peak in-cylinder pressure advances as the oxygen volume fraction increases. Fig. 8.13 (b) shows the effect of the oxygen concentration on the rate of pressure rise and corresponding phase under different spark timings (dry cycle). It can be seen that the increased combustion rate under the higher oxygen volume fraction causes the maximum pressure rise rate to increase, and the phase of the maximum pressure rise is also advanced.

Fig. 8.14 shows the effect of the oxygen concentration on the in-cylinder pressure in the dry and water cycles. The engine speed was set to 1500 r/min with an ignition angle of 35°CA BTDC. The water injection pressure was 38 MPa, and the water injection duration was 3ms. The water injection time was 10°CA ATDC and the water injection temperature was 120°C. The fuel mass was 52.7 mg, the compression ratio was 10.5, and the intake pressure was 101 kPa. Fig. 8.14 shows that the combustion rate increases under the dry cycle as the oxygen volume fraction increases. Therefore, the in-cylinder temperature increases under the higher oxygen volume fraction, and the evaporation rate of the injected water increases with fewer negative effects on the combustion process. Furthermore, the increase in water vapor increases the mass of the working fluid more rapidly due to the more rapid evaporation process, which increases the in-cylinder pressure and indicated work. Hence, as shown in the Figure 12, the in-cylinder pressure during the expansion stroke increases as oxygen volume fraction increases. The in-cylinder pressure in the Figure 11 is derived from the average pressure of 50 cycles. Hence, it is noteworthy that the in-cylinder pressure of the water injection cycle from the start of combustion to TDC is lower than that of the dry cycle for all cases, which is because the residual water from the last cycle results moderates the combustion process of the next cycle.

Fig. 8.15(a) shows the effect of the oxygen concentration on the indicated work of the ICRC engine. Engine speed was set to 1500 r/min with an ignition angle of 35°CA BTDC. The water injection pressure was 38MPa, and the water injection

duration was 3 ms. The water injection time was 10°CA ATDC, and the water injection temperature was 120°C. The fuel mass was 52.7 mg, compression ratio was 10.5, and the intake pressure was 101kPa. As shown in Fig. 8.15(a), the indicated work of the oxy-fuel combustion (dry and water cycles, more than 792J) is more than the indicated work of the air combustion (768J, fuel mass 49.7mg; 786J, fuel mass 52.7mg), because the fuel mass is excessive and unable to be oxidized completely under air combustion, whereas there was sufficient oxygen to completely combust the fuel under oxy-fuel combustion, and therefore the greater release of heat increases the indicated work because more fuel is burned. The combustion rate increases with the higher oxygen volume fraction, and the negative compression work increases, and therefore the indicated work of the dry cycle with a 49.7mg fuel mass decrease from 813J to 792J when the oxygen volume fraction increases from 50% to 60%. However, the improvement of water injection to the indicated work increases as the oxygen fraction volume increases. Especially under larger water injection duration (3-7ms), the indicated work for the 60% oxygen volume fraction is even greater than the indicated work for the 50% oxygen volume fraction. This is a result of the higher in-cylinder temperature obtains under higher oxygen volume fraction and the more rapider combustion rate, and the injected water evaporates more rapidly with a smaller negative impact on the combustion process. Moreover, more working fluid is added into the cylinder near the top dead center and the indicated work increases. It can also be seen in the Fig. 8.15 (a) that optimal water injection duration for the best indicated work exists under the two oxygen volume fraction conditions, and the optimal injection duration increases as the oxygen volume fraction increases. The flame propagation speed and the in-cylinder temperature increase under the higher oxygen volume fraction. Therefore, a greater water injection mass can be endured and employed to add to the mass of the working fluid when the oxygen volume fraction increases, and the indicated work will increase. The indicated work and ITE of water cycle (OF=60%，52.7 mg) increase by 9% (from 823J to 896J) and 2.7%, respectively, compared to the dry cycle, and

increase by 14% (from 786J to 896J) and 4.1%, respectively, compared to the air combustion cycle .

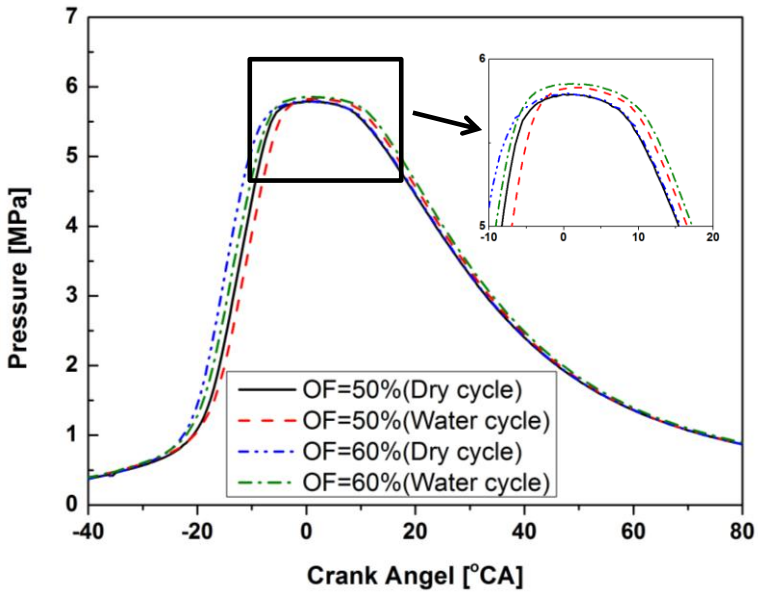


**Fig. 8.14** Effect of the oxygen concentration on the in-cylinder pressure of the ICRC engine (dry and water cycles)

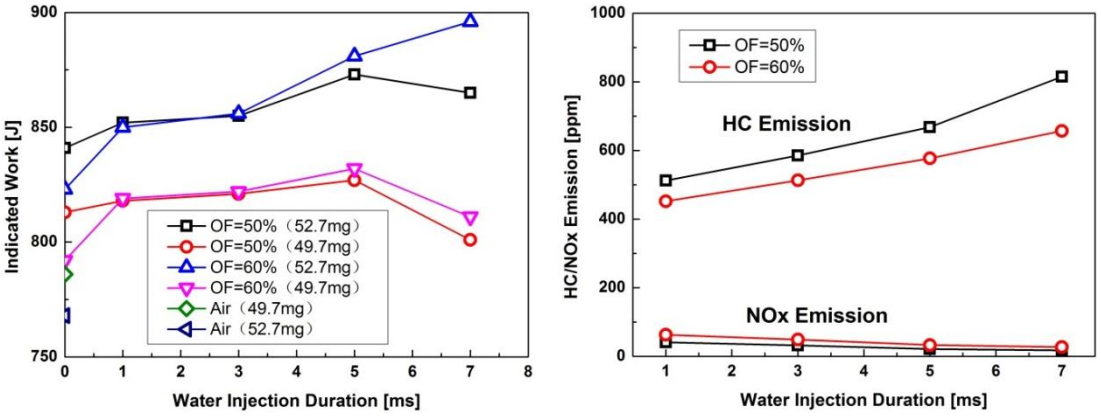


(a) Indicated work (b) HC/NOx emission

**Fig. 8.15** Effect of oxygen concentration on the indicated work and HC/NOx emission of ICRC engine (air, dry and water cycles)

Fig. 8.15(b) shows the HC/NOx emissions under different oxygen concentrations. The operation condition is the same as the condition in the Fig. 8.15(a). Fuel was burned more completely under the higher oxygen volume fraction, and the HC emissions decrease therefore as the oxygen volume fraction increases. HC emissions

decrease from 585 ppm to 513 ppm due to the increase in the oxygen volume fraction, when the water injection duration is 3ms. As mentioned before, a higher oxygen volume fraction means a higher in-cylinder combustion temperature, which is the key for the formation of NOx. Hence, the NOx emissions increase when the oxygen volume fraction increases.

### 8.3.3 Effect of the compression ratio on the combustion and emission

Fig. 8.16 shows the effect of compression ratio (CR) on the in-cylinder pressure and pressure rise rate (water cycle). Engine speed was set to 1500 r/min with an ignition angle of 25°CA BTDC. The water injection pressure was 35MPa, and the water injection duration was 3ms. The water injection time was 10°CA ATDC, and the water injection temperature was 120°C. The oxygen volume fraction was 50% and the intake pressure was 101kPa. As shown in the Fig. 8.16 and Table 8.7, the peak in-cylinder pressure increases and the phase of the combustion advances as the compression ratio increases. Because the in-cylinder pressure and temperature increase as the compression ratio increases, and the ignition delay of the fuel is shortened and the speed of flame propagation increases. It can be also seen in the Fig. 8.16 (b) that the pressure rise rate increases when compression ratio increases, and corresponding phase also advances.

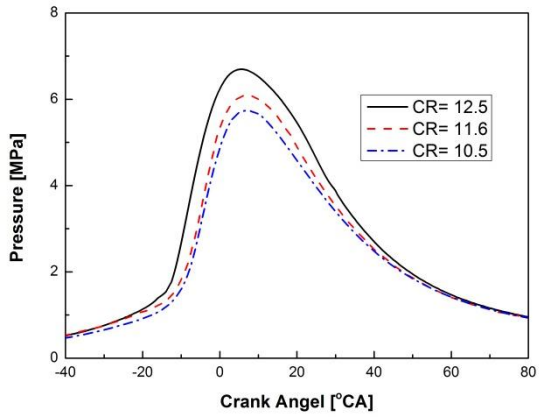


(c) In-cylinder pressure

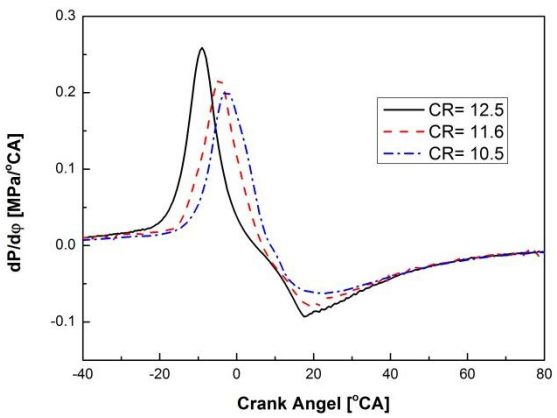


(d) Pressure rise rate

**Fig. 8.16** Effect of compression ratio on the in-cylinder pressure and pressure rise rate (water cycle)

**Table 8.7** Combustion characteristics under different compression ratios

| ***Compression ratio [-]*** | 10.5 | 11.6 | 12.5 |
|---|---|---|---|
| ***Pmax [MPa]*** | 5.73 | 6.09 | 6.70 |
| ***φ(Pmax) [°CA ATDC]*** | 7.5 | 7.0 | 5.5 |
| $(dP/d\varphi)_{max}$ ***[MPa/°CA]*** | 0.2 | 0.22 | 0.26 |
| $\varphi((dP/d\varphi)_{max})$ ***[MPa/°CA]*** | -2.5 | -4.5 | -9 |

Fig. 8.17 shows the effect of compression ratio (CR) on the in-cylinder pressure and the indicated work of dry and water cycles. The operation condition is the same as the operation condition of Fig. 8.16. As shown in Fig. 8.17(a), (b), (c), the in-cylinder pressure of water cycle is the average pressure of 50 cycles. Hence, the in-cylinder pressure of the water injection cycle from the start of the combustion to TDC is lower than that of the dry cycle for all cases, which is because the residual water from last cycle results moderates the combustion process of the next cycle. It can been found from the Fig. 8.17(a), (b), (c) that the effect of the residual water on the combustion process of the next cycle becomes less as the compression ratio increases. When the compression ratio is 12.5, the in-cylinder pressures of the dry and water cycles under compression stroke are almost coincidence, because the negative impact of the residual water reduces due to higher in-cylinder temperature and pressure under higher compression ratio. Fig. 8.17(d) shows the effect of water injection on the indicated work under different compression ratios. The indicated work with CR =11.6(dry cycle) is larger than the indicated work with CR =10.5 (dry cycle) because the peak in-cylinder pressure increases as the compression ratio increases. But the indicated work (dry cycle) decreases when compression ratio increases from 11.6 to 12.5. It is because that the negative compression work increases under higher compression ratio, which leads to the decrease in the

indicated work. However, the indicated work of water cycle increases much obviously as the compression ratio increase. Water injection and evaporation process starts near the top dead center, and therefore the water vapor can add to the mass of the working fluid directly under expansion stroke without the negative compression work. The higher pressure and temperature environment under higher compression ratio are conducive to the evaporation of water with less negative impact on combustion, and also increase the working capacity of water vapor. Hence, the indicated work increases. The indicated work increases by 12.4% due to water injection when compression ratio is 12.5.

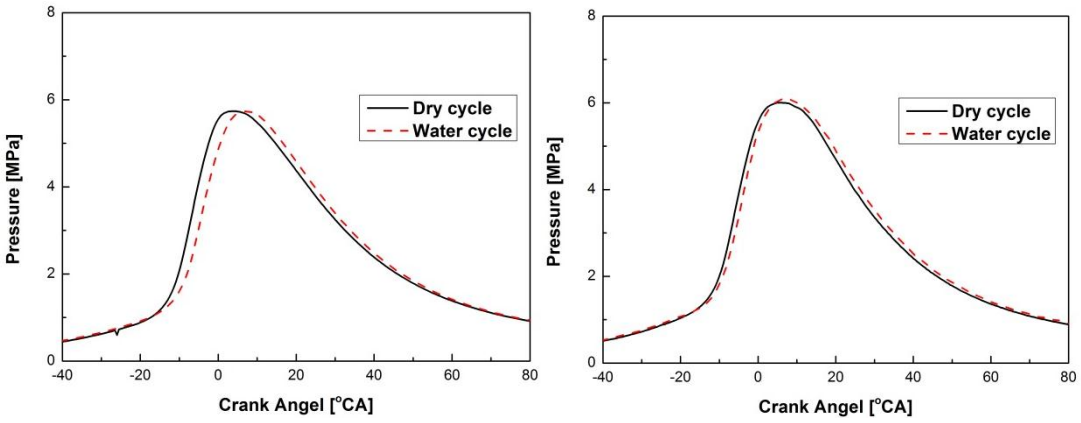


(a) CR =10.5 (b) CR =11.6

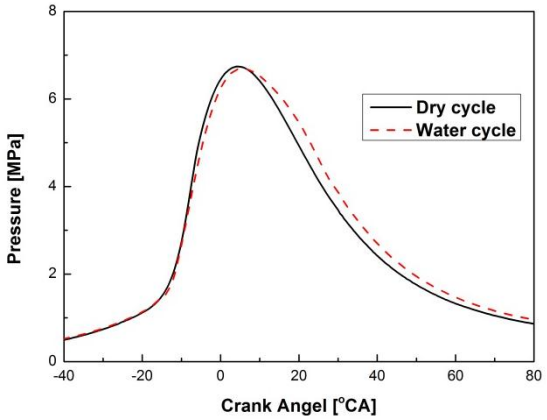


| *Compression ratio(-)* | 10.5 | 11.6 | 12.5 |
|---|---|---|---|
| *Indicated work - dry cycle (J)* | 831 | 863 | 847 |
| *Indicated work - water cycle (J)* | 844 | 918 | 952 |
| *Increase of indicated work (%)* | 1.56 | 6.37 | 12.4 |

(c) CR =12.5 (d) indicated work

**Fig. 8.17** Effect of the compression ratio on the in-cylinder pressure and indicated work (dry and water cycles)

Fig. 8.18(a) shows the effect of the water injection on the increment of the indicated work under different compression ratios. The indicated work increases much obviously as the compression ratio increases. The increment of the indicated work increases from 2.7% (CR =10.5) to 12.4% (CR =12.4%), compared to the oxy-fuel combustion cycle. Moreover, the ITE under water cycle (5ms, CR=12.5) is increased by 4.9%, compared to the air combustion cycle. Under the operation condition with the low compression ratio (CR =10.5), the injected water has more negative effect on the combustion process due to the lower combustion rate and in-cylinder temperature. Therefore, the indicated work decreases as the water injection duration increases. But under higher compression ratio (11.6, 12.5), the negative effect of the water injection on combustion process decreases because the speed of flame propagation and in-cylinder temperature increases under high compression ratio. Moreover, the work derived from water evaporation increases. Hence, the indicated work increases when the injected water mass increases properly. But excessive water is injected into the cylinder, the in-cylinder temperature decreases sharply and the indicated work decreases. The optimal water injection duration exists under different compression ratios, and the optimal water injection duration increases as the compression ratio increases. It shows that more water can be injected into cylinder to increase the mass of the working fluid under higher compression ratio, and the indicated work and thermal efficiency are therefore improved.

Fig. 8.18(b) shows the HC and NOx emissions under different compression ratios. According to the previous analysis, the in-cylinder temperature and pressure are higher under higher compression ratio, and water evaporated more rapidly with less negative effect on flame propagation. Hence, the HC emissions decrease as compression ratio increases. Moreover, more temperature means the formation of more NOx emissions, and the NOx emissions increase therefore as compression ratio increases. However, NOx emissions stay under low level.

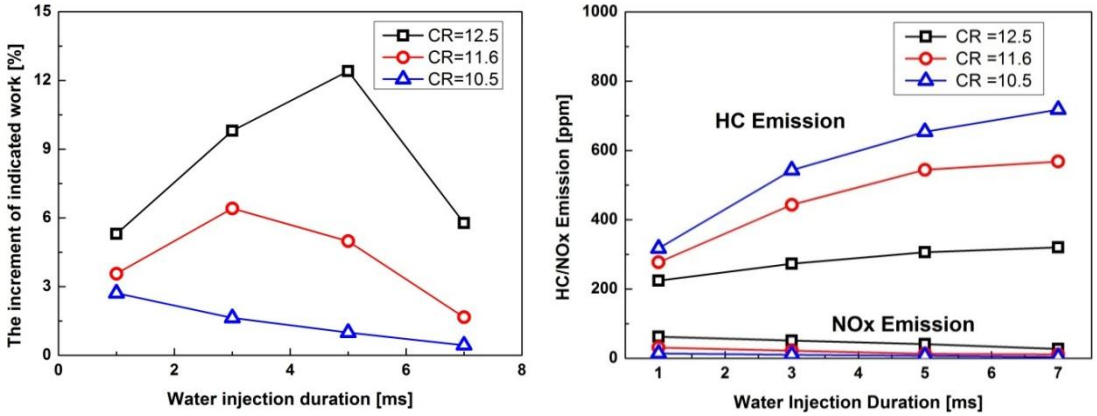


(a) Increment of indicated work (b) HC/NOx emission

**Fig. 8.18** Effect of water injection on the increment of indicated work and the HC/NOx emissions under different compression ratios

### 8.3.4 Effect of the water injection on the engine stability

Water is usually considered for the fire suppressant because it can dilute oxidant gas and reduce temperature effectively. Whereas Excessive water injection mass may lead to violent cyclic variation in THE ICRC engine, even engine flameout. Moreover, according to the previous analysis, the higher load and temperature, which may lead to rough operation, are propitious for the work of the injected water. And the water injection is therefore needed in ICRC engine to control the fast combustion rate of the oxy-fuel combustion. Hence, the investigation of the effect of water injection on the engine stability is important in ICRC engine. The COV (coefficient of variation) value of IMEP (indicated mean effective pressure) is usually employed to indicate the cyclic variation of the engine [59], and it can be expressed:

$$COV_{IMEP} = 100\% \times \frac{(\frac{1}{n-1}\sum_{i=1}^{n}(IMEP_i - \overline{IMEP})^2)^{1/2}}{\overline{IMEP}} \quad (8.9)$$

where $COV_{IMEP}$ is the *COV* value, $IMEP_i$ is the *IMEP* value of i cycle, and $\overline{IMEP}$ is the average *IMEP* value of *n* cycles.

Fig. 8.19 shows the effect of the water injection on the engine stability under different loads. Fig. 8.19(a) shows that the $COV_{IMEP}$ value of the dry cycle is 4.7% under higher load, while the $COV_{IMEP}$ of water cycle decreases to 3.3%, because the

water injection reduces the in-cylinder temperature and controls the rapid combustion rate. As is shown in the Fig. 8.19(b), the cyclic variation reduces under the low load, and the $COV_{IMEP}$ value (1.2%) is less than the $COV_{IMEP}$ value of high load. Compared with the high load, the in-cylinder temperature is lower under the low load, and water injection therefore has more negative effect on the combustion and flame propagation process. Hence, the $COV_{IMEP}$ of the water cycle is more than the $COV_{IMEP}$ of the dry cycle under the low load.

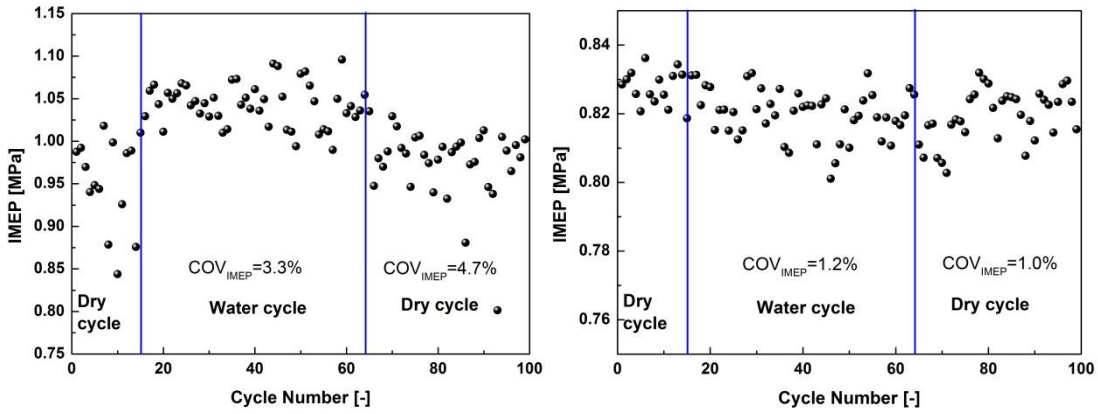


(a) High load (IMEP =0.97bar Dry cycle) (b) Low load (IMEP =0.82bar Dry cycle)

**Fig. 8.19** Effect of water injection on the engine stability under different loads

Fig. 8.20 shows the effect of water injection on the cyclic variation under different fuel injection masses. The engine speed was set to 1500 r/min with an ignition angle of 30°CA BTDC. The water injection pressure was 38MPa. The water injection time was 10°CA ATDC and water injection temperature was 120°C. The oxygen volume fraction was 50% and intake pressure was 101kPa. Fig. 8.20 shows that water injection can reduce the $COV_{IMEP}$ value. With 47.9mg fuel mass, the $COV_{IMEP}$ value decreases from 1.7% to 0.5% when the water injection duration increases from 0ms to 3ms. When water injection duration increases from 3ms to 7ms, the $COV_{IMEP}$ value also increases because the excessive water injection mass has more negative effect on the combustion process. More fuel mass lead to more heat release, which leads to the engine operation roughness. Hence, the $COV_{IMEP}$ value increases with the increase of fuel mass. Furthermore, it is shown in the Fig.

8.20 that the water injection duration for the optimal $COV_{IMEP}$ value with 52.9mg (5ms) is more than that for the optimal $COV_{IMEP}$ value with 49.7mg (3ms). The reason is that more heat release with more fuel mass means higher in-cylinder temperature, and the water injection mass for the control of the combustion process increases correspondingly.

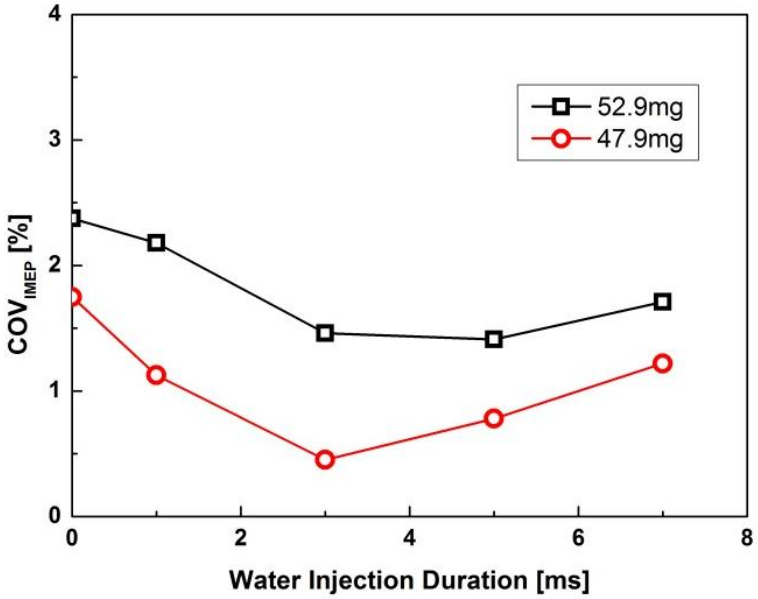


**Fig. 8.20** Effect of water injection on the engine stability under different fuel masses

Fig. 8.21 shows the effect of oxygen concentration on the engine stability. Engine speed was set to 1500 r/min with an ignition angle of 35°CA BTDC. The compression ratio is 10.5, and the fuel mass is 52.7mg. Water injection pressure was 38MPa. The water injection time was 10°CA ATDC and water injection temperature was 120°C. The intake pressure was 101kPa. When the OF value is 50%, more water injection duration can control the rapid combustion rate of the oxy-fuel combustion when water injection mass is less (1-3ms), and the $COV_{IMEP}$ value decreases from 2.68% (1ms) to 1.46% (3ms). But the water injection duration increases from 3ms to 7ms, more water injection mass lead to bad flame propagation and engine stability. Therefore, the $COV_{IMEP}$ value increases to 1.7% when water injection duration increases to 7ms. The in-cylinder temperature and combustion rate increases as oxygen volume fraction increases. More water is needed to control combustion

process, and the $COV_{IMEP}$ value decreases with the increase of oxygen volume fraction. The $COV_{IMEP}$ value with OF =60% is even less than the $COV_{IMEP}$ value of OF =50% when water injection duration is 7ms.

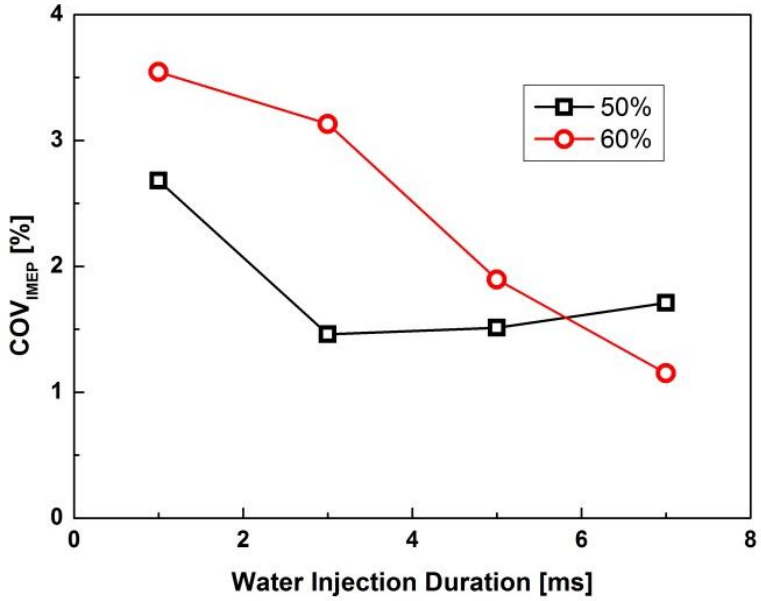


**Fig. 8.21** Effect of the water injection on the engine stability under different oxygen concentrations

Fig. 8.22 shows the effect of the compression ratio on the engine stability. The engine speed was set to 1500 r/min with an ignition angle of 25°CA BTDC. The fuel mass is 52.7mg. The water injection pressure was 38MPa. The water injection time was 10°CA ATDC and water injection temperature was 120°C. Intake pressure was 101kPa. As is shown in the Fig. 8.22, in general, the $COV_{IMEP}$ value increases as the compression ratio increase. However, when compression ratio decreases to 11.6 and 10.5, the excessive water injection mass has more negative effect on combustion process. Hence, under these two operation conditions, the $COV_{IMEP}$ value increases as the water injection duration increases (from 5ms to 7ms), due to the negative effect on combustion of the excessive water injection mass. Moreover, the optimal water injection duration for the least $COV_{IMEP}$ value increases as the compression ratio increases.

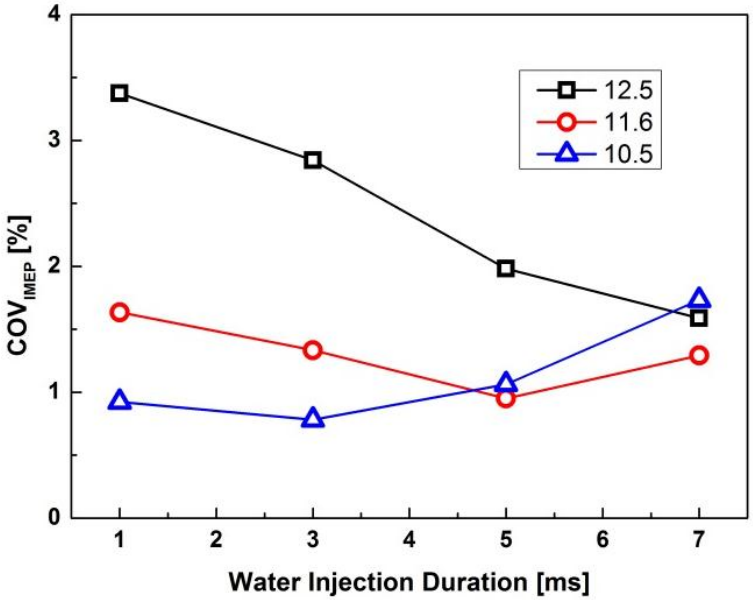


**Fig. 8.22** Effect of the water injection on the engine stability under different compression ratios

### 8.3.5 Effect of the working fluid temperature on the ICRC engine

The data derived from experiments of the frist-generation ICRC test system are investigated in this part. The engine was started with intake of air and changed to oxyfuel model after synchronized with the eddy current dynamometer, and run about 3 minutes to keep stable before any measurements were carried out. The operating conditions are listed in Table **8.8**. One hundred cycles, including 50 continuous water injection cycles, were collected for each condition. Water injection cycles and no water injection cycles (dry cycles) were distinguished by water injection signal recorded in the acquisition card. Indicator diagram and combustion parameters were drawn from the cylinder pressure to study the combustion characteristics of each test condition.

The combustion process of ICRC engine under different injection temperatures is investigated by analyzing in-cylinder pressure. The fuel injection mass was adjusted by changing injection duration, and the fuel injection duration of the three groups of dry cycles is 2.5ms (case 1), 2.7ms (case 2), 2.9ms (case 3) respectively. Fig. 8.23 shows the P-V diagram of the three cases and Table 8.9 lists some representative combustion characteristics. In the experiments, the in-cylinder

pressures are more than 2 MPa when water is injected at top dead center (shown in Fig. 8.23). These in-cylinder pressures are more than saturated vapor pressures of water at 20°C ~120° C in the experiments. It means that water is liquid when it is just injected into the cylinder.

**Table 8.8** Operating conditions

| | |
|---|---|
| Speed (r/min) | 2400 |
| O2 volume fraction (%) | 50 |
| Ignition timing (°CA BTDC) | 30 |
| Water Injection timing (°CA BTDC) | 0 |
| Water Injection pressure (MPa) | 22 |
| Throttle position (%) | 15 |

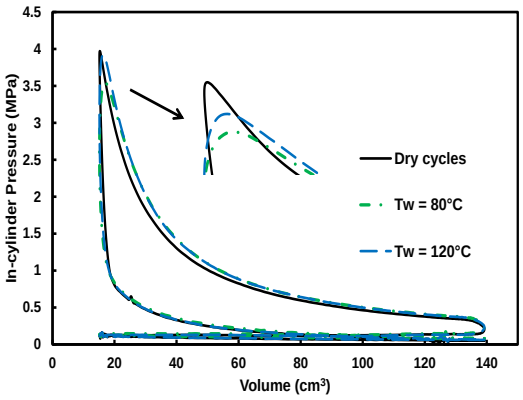


(a) Case 1

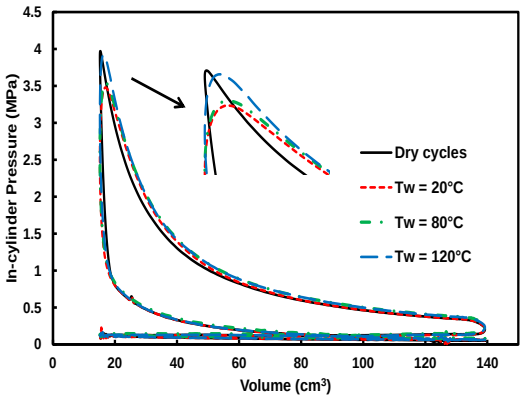


(b) Case 1

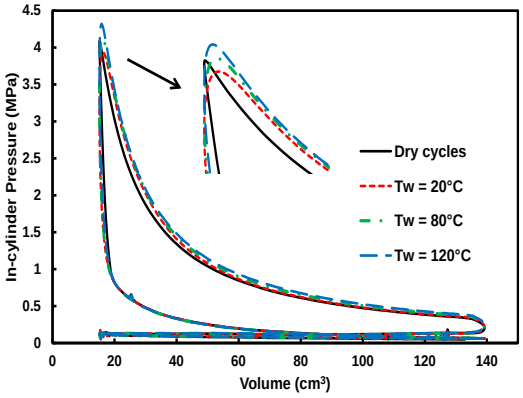


(c) Case 3

**Fig. 8.23** Effect of the working fluid temperature on the in-cylinder pressure

The fuel injection mass of case 1 is least among the three cases. Because the engine runs unsteadily and misfire happens frequently when the water injection temperature is 20°C, only results with 80°C and 120°C water injection temperatures are showed in Fig. 8.23(a). As seen in Fig. 8.23(a), the peak in-cylinder pressure of dry cycles is lower than the ones of the other two cases and only 3.80 MPa. The in-cylinder pressure drops obviously in water injections cycles in contrast to the dry cycles, but IMEP remains same or even higher because the evaporation of the injected water increases the mass of working gas inside the cylinder. Higher water injection temperature leads to rapider evaporation of water mist, which does less negative impact on the combustion process [58]. Therefore, the peak in-cylinder pressure rises from 3.10 MPa to 3.35 MPa when $T_w$ increases from 80°C to 120°C.

**Table 8.9** Operating conditions

| **Parameter** | **Case 1** | | | | **Case 2** | | | | **Case 3** | | | |
|---|---|---|---|---|---|---|---|---|---|---|---|---|
| Fuel injection duration (ms) | 2.5 | | | | 2.7 | | | | 2.9 | | | |
| Water injection duration (ms) | 0 | 0.4 | | | 0 | 0.4 | | | 0 | 0.4 | | |
| $T_w$ (°C) | _ | 20 | 80 | 120 | _ | 20 | 80 | 120 | _ | 20 | 80 | 120 |
| $P_{max}$ (MPa) | 3.80 | _ | 3.10 | 3.35 | 3.97 | 3.48 | 3.54 | 3.92 | 4.09 | 3.93 | 4.13 | 4.32 |
| $\phi_{Pmax}$ (°CA) | 364 | _ | 373 | 371 | 362 | 373 | 372 | 369 | 361 | 369 | 368 | 367 |
| $(dP/d\theta)_{max}$ (MPa) | 0.217 | _ | 0.108 | 0.119 | 0.238 | 0.133 | 0.135 | 0.169 | 0.252 | 0.171 | 0.183 | 0.202 |
| $\phi_{(dP/d\theta)max}$ (°CA) | 353 | _ | 358 | 357 | 351 | 359 | 357 | 356 | 349 | 357 | 356 | 355 |
| IMEP（MPa） | 0.65 | _ | 0.65 | 0.67 | 0.68 | 0.70 | 0.71 | 0.74 | 0.70 | 0.72 | 0.76 | 0.78 |

According to the Fig. 8.23(a) and Table 8.9, the in-cylinder pressure rise rate can be controlled as water is injected into the cylinder during the combustion process, and the peak in-cylinder pressure rise rate decreases effectively from 0.217 MPa to about 0.11 MPa. Besides, the combustion phasing is retarded in water injection cycles and the phenomenon of retard combustion phasing is more obvious under

lower water injection temperature condition. It is noteworthy that the in-cylinder pressure of the water injection cycle from combustion start to TDC is lower than that of the dry cycle for all cases, which is because the residual water from last cycle results moderates the combustion process of the next cycle.

More fuel injection mass is employed in case 2. Fig. 8.23(b) shows that the peak in-cylinder pressures of both the dry and the water injection cycles are significantly increased in case 2. The side effect of water injection to the peak in-cylinder pressures reduces as fuel mass increases. Especially when water injection temperature is 120°C, the peak in-cylinder pressure of water injection cycles reaches to 3.92MPa, which is almost same to that in dry cycle. It is also clear from the P-V diagram that the water injection cycle has a higher in-cylinder pressure during expansion stroke. Hence, the IMEP of water injection cycles are increased compared with the dry cycle. The IMEP increases as water injection temperature increases and reaches to 0.74 MPa under 120°C water injection temperature condition.

Fig. 8.23(c) shows case 3 where IMEP of the dry cycle is increased to 0.70MPa, and the water injection process no longer has side effects on the peak in-cylinder pressure. The peak in-cylinder pressures of water injection cycles are higher than that of dry cycles when $T_w$ are 80°C and 120°C.The increase of fuel mass results in higher in-cylinder temperature. The evaporation of water mist becomes much rapider under higher background temperature, which has less negative effect on combustion. Besides, the supplement of rapider evaporating water vapor to working fluid causes the peak in-cylinder pressure and pressure rise rate to rise, and higher peak in-cylinder pressure means larger area of indicator diagram. Therefore, it is seen from Table 8.9 that higher engine load and water injection temperature leads to higher peak in-cylinder pressure and IMEP. Furthermore, the phases of peak in-cylinder pressure and pressure rise rate are retarded more obviously as water injection temperature decreases.

Fig. 8.24 shows that the comparison between indicated work and ITE of case1, 2, 3 with different water injection temperatures. As shown in the figure 7, the indicated

work increases but indicated thermo efficiency (ITE) decreases in the dry cycles as fuel injection duration increases. That is because more fuel mass and higher engine load means increased heat loss through higher temperature of the exhaust gas and cylinder wall when the engine speed and expansion ratio remains the same with more fuel mass. The injected water can utilize this heat effectively and increase the mass of the working fluid. Hence, the heat from the extra fuel can be converted to the indicated work by using injected water. As mentioned before, higher temperature injected water can increase the mass of the working fluid with less negative effect on the combustion process. Therefore, the indicated work and ITE of water cycles is more than these of dry cycles in Fig. 8.24. In addition, it is also seen in the Fig. 8.24 that higher water injection temperature contributes to enhance the indicated work and ITE.

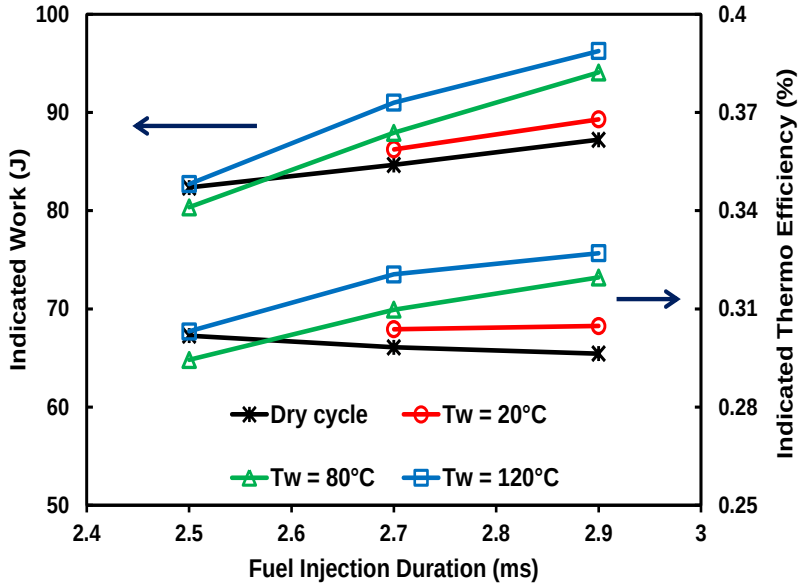


**Fig. 8.24** Comparison of the indicated work and ITE between dry cycle and water injection cycle

Fig. 8.25 shows the effect of water injection temperature on the increment of ITE under different water injection durations. The increment of ITE is the ITE increase compared with the dry cycles due to water injection in the combustion process. It is seen in Fig. 8.25 that water injection leads to the increase of ITE in all operating conditions. The increment of ITE decreases as water injection duration increases

when $T_w$ = 20°C. That is because that more low temperature water into cylinder is hard to evaporate promptly so that combustion process is affected by water mist. It also can be seen from Fig. 8.25 that more water injection temperature is propitious to increase indicated thermo efficiency. The increment of ITE curves appear to have a trend of rise first then fall under 80°C and 120°C water injection temperature condition, and an optimal injection duration for the best ITE exists in these two cases. When water injection temperature is high and injection mass is suitable, more water into cylinder contributes mainly to the increase of the working gas (water vapor) and have relatively little negative influence on combustion process and in-cylinder temperature, which leads to higher ITE. An inflection point, which is optimal injection duration for the best indicated thermal efficiency, is reached with the increase of water injection mass. After the inflection point, the negative effect of water injection occupies more important place with the increase of water injection mass, and it causes the ITE decreases after the inflection point as water injection duration increases. In addition, it is also observed that the optimal injection duration for the best indicated thermal efficiency improves with the increase of water temperature.

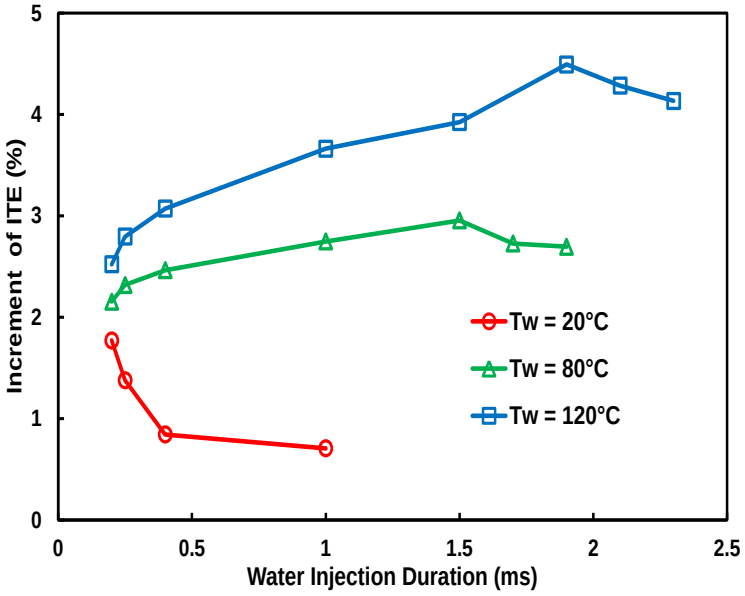


**Fig. 8.25** Effect of water injection temperature on the increment of ITE under different water injection durations (IMEP of dry cycles =0.70MPa)

The in-cylinder temperatures in Fig. 8.23 were calculated by using one dimensional model, and the in-cylinder temperature at the water injection timing was evaluated from the in-cylinder pressure. The ITE (mfuel=2.5ms, water injection temperature = 20°C) isnot shown due to bad engine stability. Fig. 8.23 shows that both of two working fluild (water and original working gas) temperatures can increase work. According to the previous analysis, the evaporation speed of the injected water increases due to higher water injection temperature and in-cylinder temperature. Hence, the work derived from the injected water focuses on TDC. Moreover, performance ability of the injected water increases, therefore, the work increases.

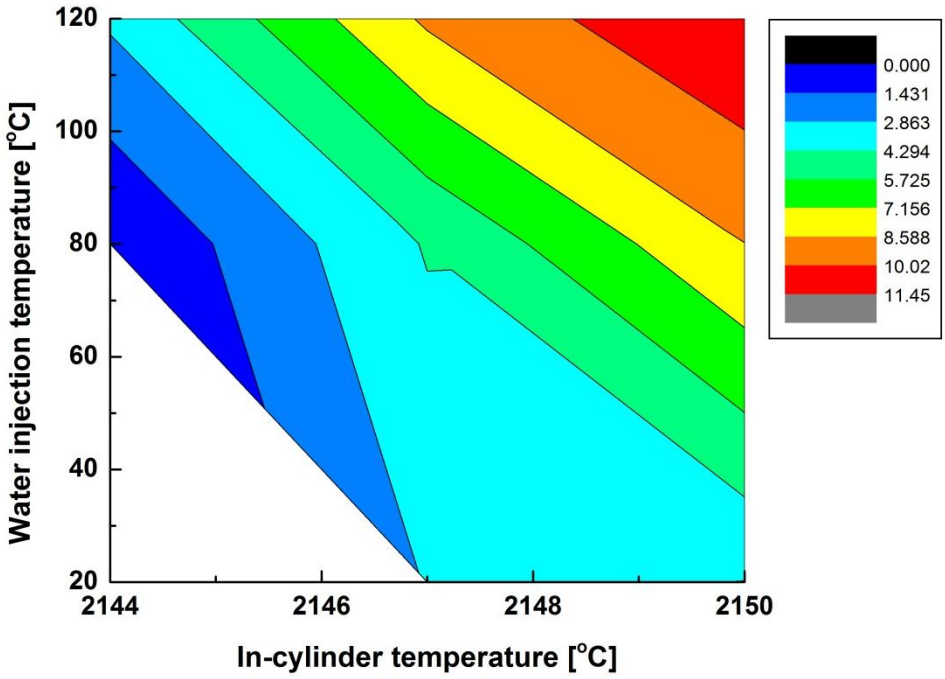


**Fig. 8.26** Effect of the working fluid temperature on the increment of the work

The exhaust gas analyzers manufactured by Combustion company (Model: HFR500 and CLD500) is used here to measure transient emissions of HC and NOx. Fig. 8.27 is the emission lines of 5 continuous oxy-fuel combustion cycles, and it is clear from the water injection signal that the first cycle is a dry cycle, and the other four cycles are water injection cycles.

The $NO_x$ line indicates that the $NO_x$ emissions of the dry cycle are around 800ppm, which is an abnormal phenomenon considering the fact that this is an oxy-fuel combustion cycle. The reason for this result may be the leakage of the intake pipe line, or the residual $N_2$ in the intake charge. The $O_2$ and $CO_2$ bought has a purity of 99%, and the residual gas is mainly $N_2$, although the $N_2$ concentration in the intake is very low, due to the much higher oxygen concentration and the high combustion temperature, the percent conversion of $NO_x$ will be much higher than that of air. When water is injected, the in-cylinder temperature is effectively decreased. Since high temperature is a decisive factor for the formation of $NO_x$, it is seen in the four water injection cycles that the $NO_x$ emission of the water injection cycle is kept at a very low level.

The HC emission, on the other hand, has an opposite result compared with the $NO_x$ emissions. The HC emission of the first cycle is quite low since the high oxygen concentration guarantees a complete combustion of the fuel injected.

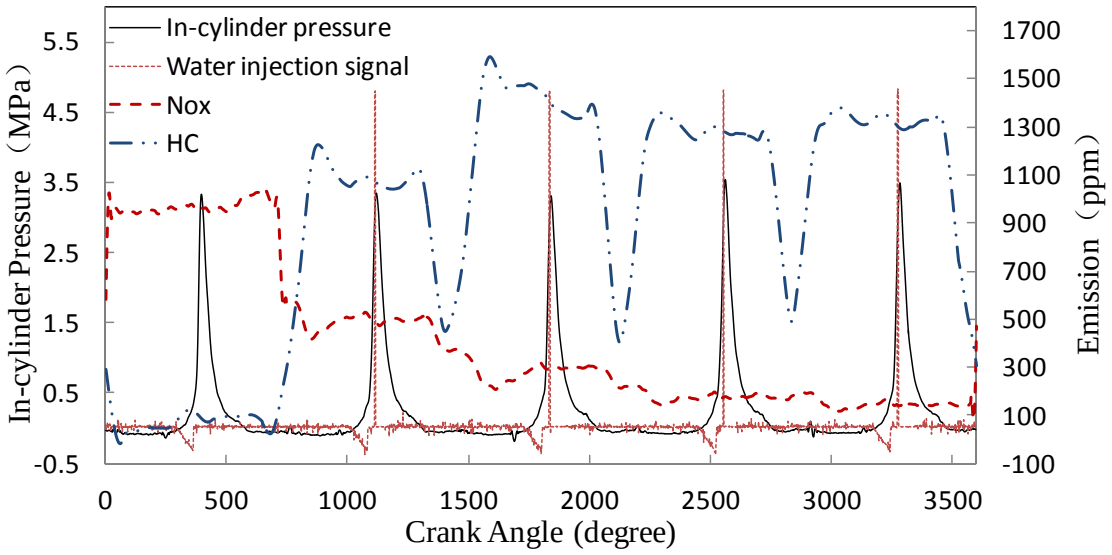


**Fig. 8.27** Emission characteristics of oxy-fuel combustion cycle with water injection

However, the HC emission increases significantly when water is injected. The reason for this is that the water mist injected has strong negative effects of the flame propagation, and may cause quench of the flame near top dead center. The incomplete combustion will cause an increase in the HC emission.

The HC emission of water injection cycles is shown in Fig. 8.28. Higher temperature injected water can evaporate more rapidly, which leads to less negative effect on combustion process. Relatively stable combustion environment and smooth flame propagation help the oxidation process of hydrocarbons. Therefore, HC emission decreases as the water injection temperature increases. In addition, the increase of the fuel mass means higher in-cylinder temperature, which results in the faster flame propagation and water mist evaporation speed. The HC emission is 667ppm when fuel injection duration reaches 2.9ms and water injection temperature reaches 120°C.

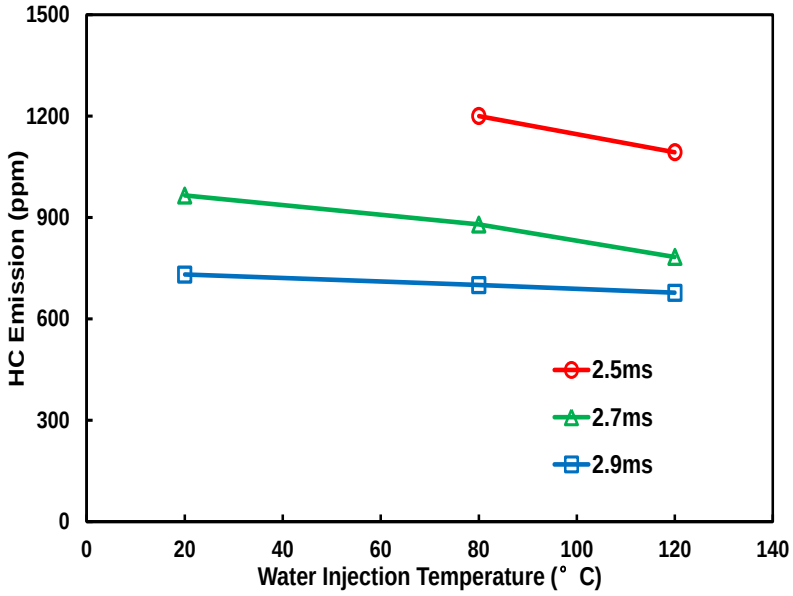


**Fig. 8.28** Effect of water injection temperature on HC emission under different fuel injection durations (water Injection duration = 0.4ms)

In the ideal state, NOx emission should not exist in oxyfuel combustion, but NOx emission in the dry cycles is even a little higher than conventional engine. The reason is that the purity of industrial $O_2$ and $CO_2$ production is about 99%, the remaining gas is mainly $N_2$. Although $N_2$ concentration in the intake is very low, due to the much higher oxygen concentration and higher combustion temperature, the production rate of NOx is much higher than that of air. However, water injection can decrease

the in-cylinder temperature, which is the key of NOx production. Hence, the NOx emission of the water injection cycle is less.

Fig. 8.29 illustrates that the effect of water injection temperature on NOx emission under different fuel injection durations. The trend of NOx emission runs counter to the HC emission. More water injection temperature and fuel injection mass, which means higher in-cylinder temperature, leads to higher NOx emission. However, Compared with HC emission, NOx emission stays under lower level because injected water reduces in-cylinder temperature. In these three operating conditions, the maximum of NOx emission is only 100ppm when fuel injection duration is 2.9ms and water injection temperature is 120°C.

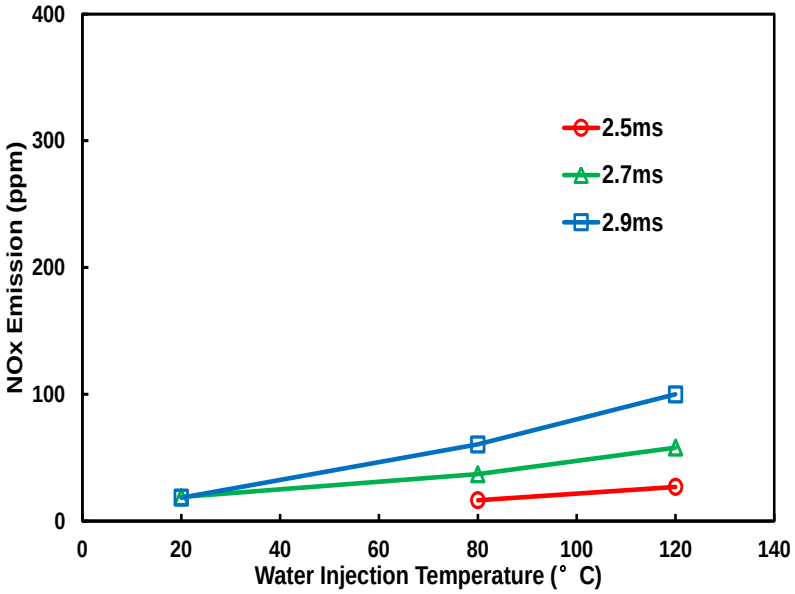


**Fig. 8.29** Effect of water injection temperature on NOx emission under different fuel injection durations (water Injection duration = 0.4ms)

## 8.4 Thermal efficiency boundary analysis of an internal combustion Rankine cycle engine

### 8.4.1 Effect of the working fluid temperature on the ICRC engine

The injected water is heated by exhaust gas in an ICRC engine. Thus, the final temperature of the injected water is determined by the heat exchange between

exhaust gases and injected water, and the exhaust gases heat exchanger is focused in this chapter.

Heat exchangers are frequently characterized by construction features. Four major construction types are tubular, plate-type, extended surface and regenerative exchangers. Among them, Tubular exchangers can be designed for high pressures relative to the environment and high-pressure differences between the fluids. Tubular exchangers are utilized primarily for liquid-to-liquid and liquid-to-phase change heat transfer applications [60]. In an ICRC heat exchange system, cold flow is the injected water under high pressure. Hence, the heat exchanger of tubular type is suitable for this application. Shell-and-tube exchanger, as one of the most commonly used tubular heat exchanger, is extensively used in industry for the following reasons: simple construction, wide application to various working conditions and low cost [20]. Therefore, a shell-and tube exchanger with 1 shell pass-2n shell passes presented in Fig. 8.30 is selected and designed for the heat exchange between exhaust gas and injected water in ICRC engine.

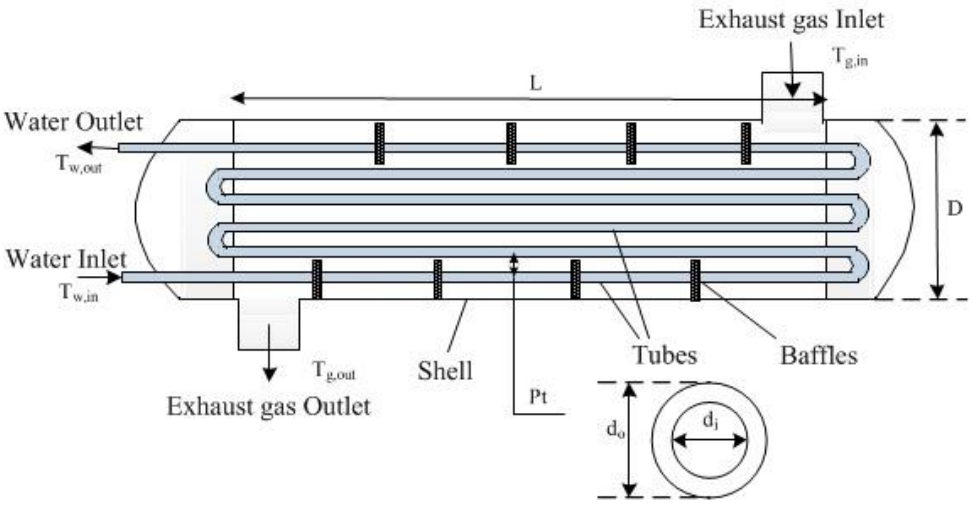


**Fig. 8.30** Schematic diagram of the shell-and-tube exchanger in ICRC engine

Based on the outputs of ideal thermodynamic analysis of the ICRC engine cycle, parameters and overall heat transfer coefficient of heat exchanger were designed and determined in this part.

According to heat transfer equation and heat balance [61], heat and the outlet temperature of exhaust gas can be solved:

$$\mathrm{Q} = \mathrm{K} \cdot \mathrm{A} \cdot \Delta \mathrm{T}_m \tag{8.10}$$

$$\Delta \mathrm{T}_m = \frac{(T_{w,out} - T_{w,in}) - (T_{g,in} - T_{g,out})}{\ln(T_{w,out} - T_{w,in}) - \ln(T_{g,in} - T_{g,out})} \tag{8.11}$$

$$\mathrm{Q} = \dot{\mathrm{m}}_w \cdot C_w \cdot (T_{w,out} - T_{w,in}) = \dot{\mathrm{m}}_g \cdot C_g \cdot (T_{g,in} - T_{g,out}) \tag{8.12}$$

where K is overall heat transfer coefficient, $A$ is heat transfer area and $\Delta T_m$ is logarithmic mean temperature difference. The subscript '*w*' and '*g*' designate the water and exhaust gas respectively. $\dot{m}$ is mass flow rate and C is specific heat.

Heat transfer area could be determined assuming a reasonable K through Eq. (8.10). The selection of both outside and inside tube diameters refers to common high pressure oil pipes (6mm and 3mm respectively). By means of heat transfer area value, the preliminary design parameters of heat exchanger, including tubes number (*N*), tubes length (*L*), tubes center distance (*Pt*), baffle spacing ($L_b$) and shell diameter (*D*), could be determined.

Tube side heat transfer coefficient could be calculated from the plot of heat transfer factor ($j_h$) and Reynolds Number presented by Kern [61], as shown:

$$\mathrm{h}_i = j_h \cdot \frac{k_w}{d_i} \cdot \left(\frac{C_p \cdot \mu}{k}\right)_w^{1/3} \cdot \left(\frac{\mu_w}{\mu_{wall}}\right)^{0.14} \tag{8.13}$$

where *k* is fluid thermal conductivity, $C_p$ is fluid specific heat and $\mu$ is fluid viscosity at the water temperature (with subscript '*w*') and wall temperature (with subscript '*wall*').

Assuming constant specific heat in the shell side, Reynolds Number and the shell side heat transfer coefficient could be calculated as following [61]:

$$\mathrm{h}_o = 0.36 \cdot \frac{k_g}{d_e} \cdot Re^{0.55} \cdot Pr^{1/3} \cdot \left(\frac{\mu_g}{\mu_{wall}}\right)^{0.14} \tag{8.14}$$

$$Re = \frac{d_e \cdot u_g \cdot \rho_g}{\mu} \tag{8.15}$$

where *u*, $\rho$ and *Pr* are flow rate, density and Prandtl number. $d_e$ is equivalent diameter of tubes. Equivalent diameter of tubes array ($d_e$) in the square arrangement is calculated with the following equation:

$$\mathrm{d}_e = \frac{4Pt^2 - \pi \cdot d_o^2}{\pi \cdot d_o} \tag{8.16}$$

An overall heat transfer coefficient H' could be derived from the convective heat transfer coefficients of shell and tube side, together with the heat conduction resistance of tube wall, as following [62]:

$$H' = \frac{1}{\frac{1}{h_o}+\frac{d_o}{2\lambda}\ln\left(\frac{d_o}{d_i}\right)+\frac{1}{h_i}\frac{d_o}{d_i}} \tag{8.17}$$

Finally, the calculation value of overall heat transfer coefficient (*H'*) is to be compared to the assumed value (*H*) in Eq. (8.10), and design is considered to be feasible if *H'* is greater than H. Otherwise, a smaller H value will be assigned and a single iteration will be continued.

### 8.4.2 Boundary conditions

The initial conditions, assumptions, and constraint conditions for calculating ICRC engine thermodynamic model are listed in Table 8.10, and the engine parameters are listed in Table 8.11.

Initial temperature, intake composition, water injection pressure and engine parameters are set according to the pervious experiments [54]. The water injection pressure (20MPa) is much higher than the saturated vapor pressure of water under 0°C~240°C and therefore water can be maintained in the liquid states before injection. Volume fraction of $O_2$ is set to 45% because $CO_2$ has strong side effect on flame propagation, and lower oxygen concentration may result in instability of combustion process, especially when water is injected. Different initial pressure and water injection temperature are chosen to investigate the effect of the parameters on cycle performance. The assumptions of instantaneous water injection, vaporization and mixing are not physically realistic, but helpful to evaluate the upper boundary on the potential thermal efficiency of this cycle. The in-cylinder temperature at the state point 4, where the expansion stroke ends at BTDC, is set larger than 330 °C for two reasons: to keep the exhaust gas temperature higher enough for the recycled water heating, and to keep the temperature of water vapor above its dew point to avoid potential equipment damage due to droplet erosion. Moreover, before the heat exchange verification procedure, the thermal efficiency

of ICRC engine increases with the increase of the injected water temperature. The numerator of thermal efficiency equation (Eq. (8.7)) includes not only the work from fuel combustion but also the work from injected hot water, and denominator is the heat from the fuel complete combustion. therefore the thermal efficiency of ICRC engine may increase to a too high value when the injected water temperature increases immoderately, which is impossible because the energy of water heating is derived from exhaust gas and water temperature cannot be heated too high through exhaust gas. Hence, in order to ensure the thermal efficiency calculation of ICRC engine reasonable before the heat exchanges verification procedure, the overall thermal efficiency was set to be not more than the ideal thermal efficiency of Otto cycle. The ideal thermal efficiency calculation of Otto cycle has no effect on the thermal efficiency boundary calculation of ICRC engine, and it just helps us to remove some useless calculation points before heat exchange verification procedure. The ideal thermal efficiency of Otto cycle can be calculated by equation 16, a median value of k=1.37 used in the evaluation, and the value of the engine is about 63% in this paper. Therefore, thermal efficiency is set not larger than 63%.

$$\eta_{Otto} = 1 - \frac{1}{\varepsilon^{k-1}} \tag{8.18}$$

Inputs for gas-to-liquid heat exchanger design are listed in Table 8.12. The temperature and mass per cycle of exhaust gas calculated from the engine model are the inputs for heat exchanger design. The injected water is heated through gas-to-liquid heat exchanger by exhaust gas, and water inlet temperature is set to ambient temperature 300K. The other parameter values are chosen elaborately so that the heat exchanger could be available under most engine operation conditions and the device structure is reasonable.

**Table 8.10** Initial conditions, assumptions, and constraints

| | |
|---|---|
| ***Initial conditions*** | |
| Fuel | $C_3H_8$ |
| Initial temperature | 20°C |

| | |
|---|---|
| Initial pressure | 0.3~1bar |
| Intake composition | 45% $O_2$, 55% $CO_2$ |
| Compression ratio | 9.2~14 |
| Water injection temperature | 0°C~240°C |
| Water injection pressure | 20MPa |
| Water injection mass | 20g - upper limit value |
| Water injection timing | 360°CA |
| ***Assumptions*** | |
| Water injection duration | Instantaneous at 360°CA |
| Water and air mixing | Instantaneous at 360°CA |
| Water vaporization | Instantaneous at 360°CA |
| $\eta_{pump}$ | 50% |
| Heat transfer to cylinder walls | None |
| ***Constrains*** | |
| Temperature at state point 4 | ≥330°C |
| Thermal efficiency | ≤65% |

**Table 8.11** Engine parameters

| ***Item*** | ***Content*** |
|---|---|
| IC engine type | Single cylinder SI engine |
| Bore (mm) | 56.5 |
| Stroke (mm) | 49.5 |
| Compression ratio | 9.2 |
| Displacement (mL) | 124 |
| Fuel type | $C_3H_8$ |

**Table 8.12** Inputs for heat exchanger design

| ***Item*** | ***Value*** |
|---|---|
| Exhaust gas inlet temperature | Engine model output |

| | |
|---|---|
| Water inlet temperature | 26.85°C |
| Water outlet temperature | 160°C |
| Exhaust gas mass per cycle | Engine model output |
| Injected water mass per cycle | 100mg/cyc |
| Engine speed | 6000rpm |

### 8.4.3 Heat exchange verification

Water is heated through exhaust gas in an ICRC engine, and the final temperature of the injected water depends on the performance of the heat exchanger system. A high temperature of the injected water will not be able to be utilized when it cannot be obtained through the heat exchange, although a higher overall thermal efficiency of ICRC engine may be reached accordingly. Hence, the verification of the injected water temperature is carried out in this part.

The design parameters of the heat exchanger listed in

Table **8.13**, are determined on the basis on heat exchanger design methodology and inputs (Table 8.12),

**Table 8.13** Design parameters of heat exchanger

| ***Item*** | ***Value*** |
|---|---|
| Heat transfer area | 0.515m |
| Tube number | 28 |
| Tube length | 1m |
| Tubes center distance | 0.02m |
| Baffle spacing | 0.05m |
| Shell diameter | 0.2m |

The effectiveness-NTU method is a convenient approach for the existing heat exchanger verification [63], and the inlet temperatures and mass flow rates of water and exhaust gas under a certain operation condition from the engine model are used as inputs in the verification model.

The number of transfer units (NTU) is a dimensionless parameter that is widely used for heat exchanger analysis and is defined as [63]:

$$\mathrm{NTU} = \frac{\mathrm{K \cdot A}}{(q_m \cdot C_p)_{min}} \tag{8.19}$$

where $A$ is derived from the design parameters of the heat exchanger, which has been determined in the previous section. By means of Eq. (8.14), (8.15) and (8.16), K could be calculated based on the verification model inputs and the designed heat exchanger parameters (listed in Table 8.13).

The effectiveness is defined as the ratio of the actual heat transfer to the maximum possible heat transfer, which is defined by the maximum temperature difference between the heat transfer fluids. Since cold fluid (water) has a greater specific heat than hot fluid (exhaust gas), the effectiveness could also be expressed as following [63]:

$$\varepsilon = \frac{T_{g,in} - T_{g,out}}{T_{g,in} - T_{w,in}} \tag{8.20}$$

The exchanger effectiveness $\varepsilon$ could also be expressed as a function of NTU and heat capacity ratio, and heat capacity ratio and the effectiveness of a 1 shell pass-2n tube passes heat exchanger are calculated with [63]:

$$C_r = \frac{(q_m \cdot C_p)_{min}}{(q_m \cdot C_p)_{max}} \tag{8.21}$$

$$\varepsilon = 2\{1 + \mathrm{C}_r + (1 + \mathrm{C}_r^2)^{1/2} \cdot \frac{1+\exp[(-NTU)\cdot(1+C_r^2)^{1/2}]}{1-\exp[(-NTU)\cdot(1+C_r^2)^{1/2}]}\} \tag{8.22}$$

The calculation for the evaluation of the output temperatures of exhaust gas and water ($T_{g,out}$ and $T_{w,out}$) should be carried out adopting an simple iterative procedure. Thus, the calculation is carried out at two-steps. First, a calculation for $T_{w,out}$ and K is made by assuming an outlet temperature of exhaust gas. At the second step, $T_{g,out}$ is obtained by solving Eq. (8.12), (8.19), (8.20), (8.21) and (8.22). The iterative calculation is terminated when the calculated and assumed values of $T_{g,out}$ reach the same. The evaluated $T_{w,out}$ is the highest temperature that the injected water could be heated under this operation condition and water injection mass.

### 8.4.4 Results and discussions

Fig. 8.31 illustrates the relationship between engine exhaust gas temperature and water/intake mass ratio under different water injection temperature. The temperature of state point 4 (Fig. 8.6) is indicated as exhaust gas temperature. Due to oxy-fuel combustion and without considering heat loss in ideal thermodynamic model, the calculated exhaust gas temperature is higher than the exhaust temperature of conventional engine. Engine exhaust gas temperature is the temperature of exhaust gas inlet in the heat exchanger. $m_{water}/m_{itake}$ is the mass ratio between injected water and intake charge, and $m_{water}/m_{itake}$ is set to 0 when there is no water injection in the cycle (dry cycle).

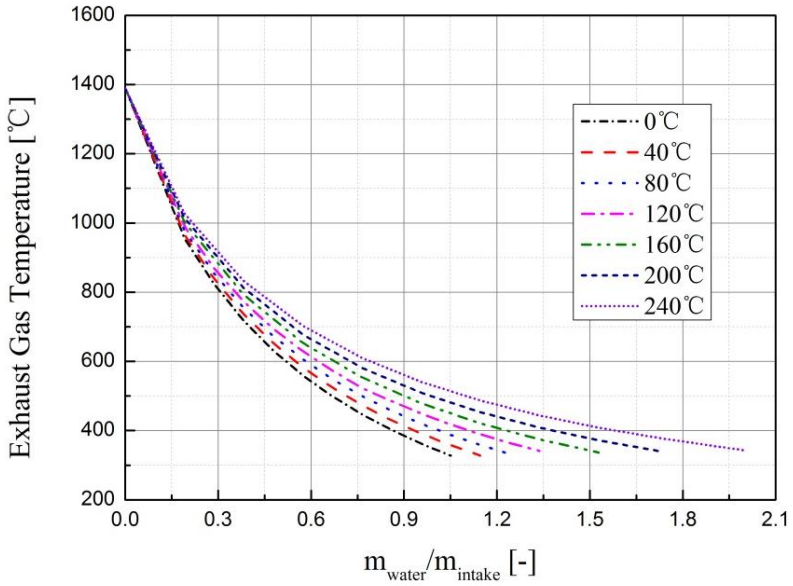


**Fig. 8.31** Engine exhaust gas temperature vs. water/intake mass ratio under different water injection temperature

As seen in Fig. 8.31, the exhaust gas temperature of dry cycle (state point 4) is near 1400°C, which results in energy loss through exhaust gas. Injected water can utilize combustion heat effectively by increasing the mass of the working fluid in the cylinder, and combustion heat could be converted into in-cylinder pressure and work. Hence, exhaust gas temperature decreases with the increase of water injection mass. On the other hand, besides the effective utilization of combustion heat, recycled water could recover waste heat through exhaust gas heat exchanger. Higher water

temperature means more heat energy recovery form the exhaust gas and more specific enthalpy. According to Eq. (8.3) and (8.3), the in-pressure and temperature of state point 5 increase due to the increase of water enthalpy, which increases the water vapor work (area 3-5-6-4 in Fig. 8.6) and is propitious to higher thermal efficiency. Hence, thermal efficiency of engine cycle increases with the increase of water injection temperature and mass as shown in Fig. 8.32. But in an ICRC engine water is heated through exhaust gas. The temperature of injected water cannot be reached without other assisted heating methods if exhaust gas temperature is too low or water injection mass is too large, and the thermal efficiency under this water injection temperature and mass is unable to be achieved. Hence, in order to ensure that the all energy of heating water from the exhaust gas, the temperatures of injected water under different injection masses were validated through the method introduced in previous section, and an overall thermal efficiency boundary of ICRC system was obtained and noted in Fig. 8.32 (red solid line). As shown in Fig. 8.32, the thermal efficiency above the thermal efficiency boundary is unable to be achieved and the highest efficiency (about 56%) appears between 160°C and 200°C.

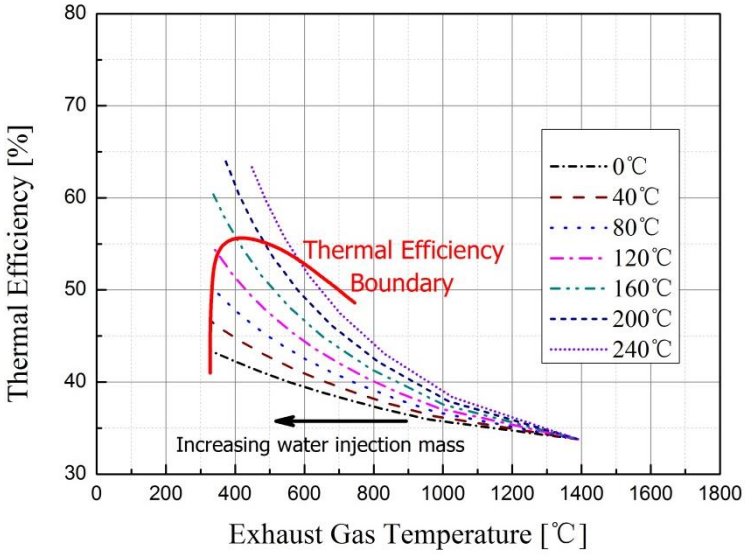


**Fig. 8.32** Thermal efficiency boundary under different injection temperature (2000rpm)

Fig. 8.33 demonstrates the thermal efficiency boundary under different engine speed (red/2000rpm, green/3000rpm, and violet/4000rpm). As seen in the Fig. 8.33, higher thermal efficiency is achieved under higher water injection temperature and more water injection mass, without regarding for the heat exchange between water and exhaust gas. It is also shown that these three thermal efficiency boundaries are calculated through heat exchange verification, and the overall thermal efficiency boundary is higher under a lower engine speed.

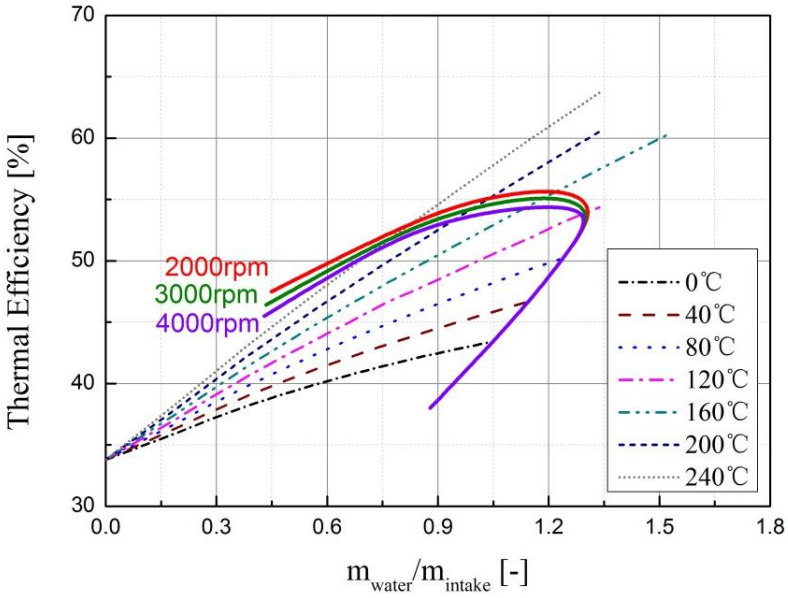


**Fig. 8.33** Thermal efficiency boundaries under different engine speed

Table 8.14 reports the parameters of heat exchange calculation process under different engine speeds, and the table shows that there is a proportional relationship between mass flow rate of exhaust gas and engine speed. It should be also noted that the overall heat transfer coefficient K of heat exchanger increases slightly with the increase of engine speed, since the increasing mass flow rate under high engine speed is propitious to bigger Reynolds Number and turbulence. Nevertheless, under higher engine speed, higher NTU and heat exchanger effectiveness are obtained with the decrease of mass flow rate according to Eq. (8.19) and (8.20). Thus, as shown in Figure 8, the maximum thermal efficiency under 2000rpm (56%) is higher than the

maximum efficiency under 3000rpm (55%) and 4000rpm (54%) due to higher heat exchanger effectiveness.

**Table 8.14** Parameters of heat exchange calculation process under different engine speeds ($m_{water}/m_{itake}$=0.76)

| *Engine speed [rpm]* | *$q_{m,g}$ [kg/s]* | *K [W/(m$^2$·K)]* | *NTU [-]* | *ε [-]* |
|---|---|---|---|---|
| 2000 | 0.0032 | 8.41 | 1.19 | 0.62 |
| 3000 | 0.0046 | 10.46 | 1.01 | 0.59 |
| 4000 | 0.0061 | 12.35 | 0.87 | 0.57 |

Intake pressure and air/fuel ratio usually indicate and control engine load in a conventional SI engine. In an ICRC engine, a mixture of $O_2/CO_2$ replaces air as intake charge. Thus, intake/fuel (I/F) ratio is used to replace the traditional air/fuel ratio as an indication for fuel mass fraction in the intake mixture. Moreover, a wide range of I/F ratio can be employed due to high oxygen concentration in the intake gas [50].

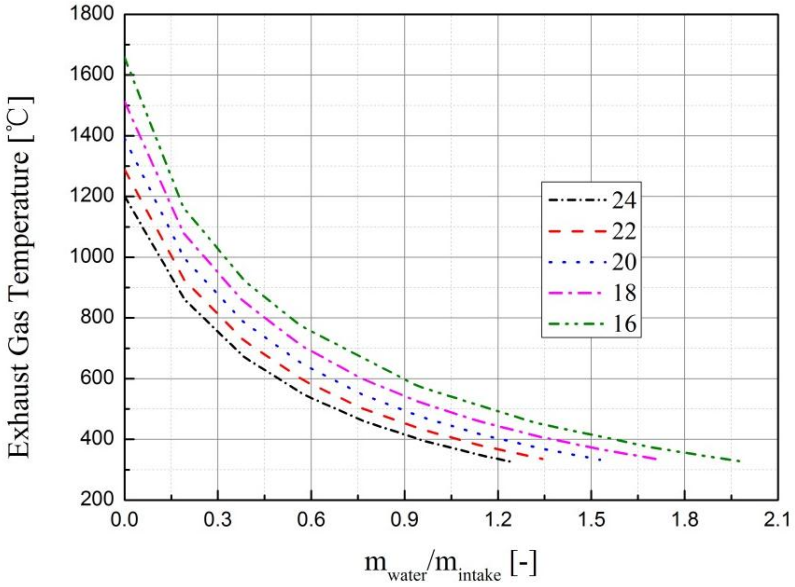


**Fig. 8.34** Exhaust gas temperature under different I/F ratio (2000rpm, water temperature 160°C)

Fig. 8.34 shows the exhaust gas temperature under different I/F ratio, and I/F ratio range is chosen according to the experiments results [23]. It is seen in Fig. 8.34

that exhaust gas temperature increases with the increase of fuel mass fraction under the same mass of the working fluid and compression ratio. More fuel consumption results in higher exhaust gas temperature and more heat loss, but injected water can use this part of heat efficiently and convert it to the work output by water vapor. And as shown in Fig. 8.35, more injected water is needed for the same thermal efficiency under higher fuel mass fraction in the mixture (lower I/F ratio). However, Thermal efficiency boundary under different I/F ratio remains the same basically.

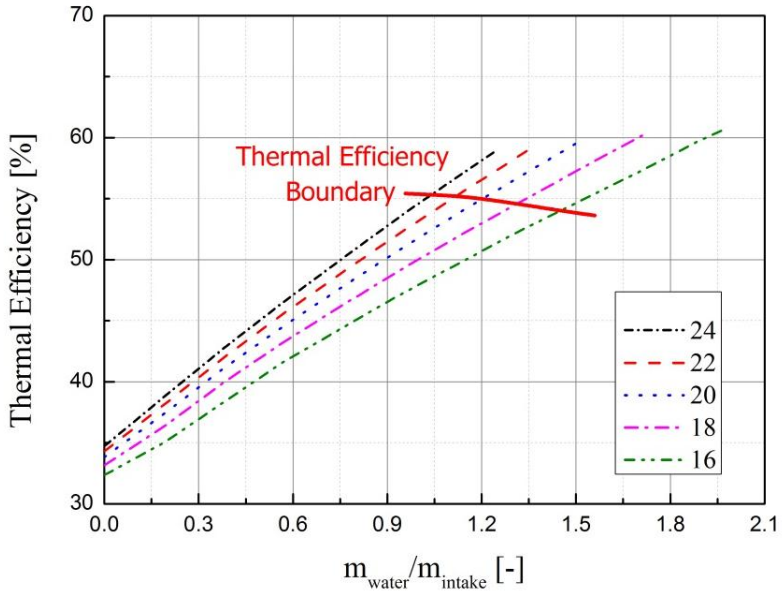


**Fig. 8.35** Thermal efficiency boundary under I/F ratio (2000rpm, water temperature 160°C)

Fig. 8.36 reports in-cylinder and exhaust gas temperatures under different intake pressure, while water injection temperature is 160°C. It is shown in Fig. 8.36 that the in-cylinder and exhaust gas temperature evolutions of all cases coincide with each other very well. The reason is that the intake pressure does not affect the maximum in-cylinder temperature much, and the temperatures of state point 4 keep the same under different intake pressure with the same water/intake mass ratio. Hence, as shown in Figure 11, thermal efficiency increases linearly with the increase of the water/intake mass ratio. Nevertheless, more intake and water mass are needed for the same thermal efficiency under higher intake pressure. According to the previous

analyses, more mass flow rates of cold and hot fluids mean lower exchanger effectiveness with the same water/intake mass ratio. Thus, it is shown in Fig. 8.37 that the thermal efficiency boundary is higher under lower intake pressure, and the optimal thermal efficiency stays about 57%. Nevertheless, the output work and IMEP are lower under lower intake pressure.

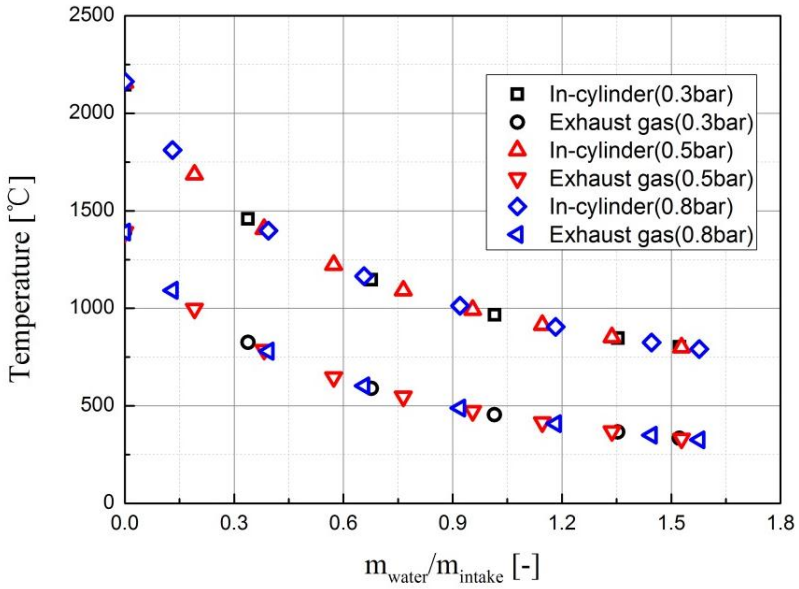


**Fig. 8.36** In-cylinder and exhaust gas temperatures under different intake pressure (2000rpm, water temperature 160°C, I/F=20)

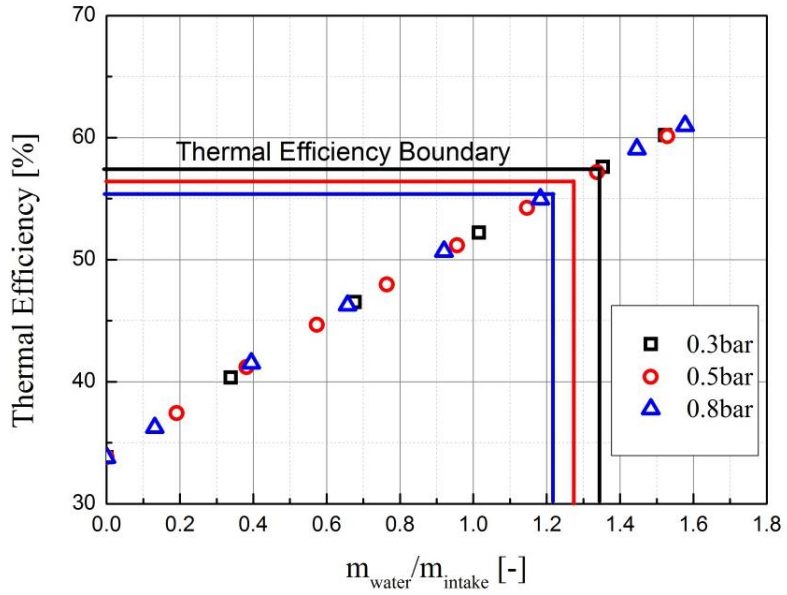


**Fig. 8.37** Thermal efficiency boundary under different intake pressure (2000rpm, water temperature 160°C, I/F=20)

Compression ratio is one of the most important engine variables, which has an important influence on the thermal efficiency [2]. Indicated thermal efficiency increases as compression ratio increases and exhaust gas temperature deceases due to expanding work stroke. Addition of water into the combustion process can decrease the in-cylinder temperature and increases the water vapor concentration before the combustion of next cycle. Thus, a more extensive compression ratio range can be applicative in an ICRC engine.

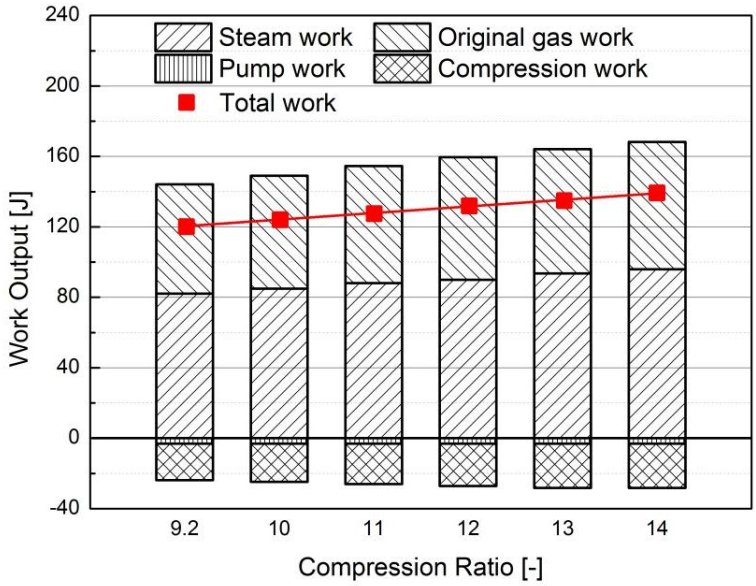


**Fig. 8.38** Work ratio under different compression ratio (2000rpm, water temperature 160°C. $m_{water}/m_{itake}$=0.76)

Fig. 8.38 reports the work ratio of water vapor and original working gas (residual $O_2$, $CO_2$ and a small amount of water vapor as product of combustion process) under different compression ratio, while compression work and pump work are also shown in the Fig. 8.38. Since expansion stroke increases with the increase of compression ratio, both original gas work and water steam work increase. Although compression negative work increases slightly as compression ratio increases, the total work of the cycle increases under same fuel consumption. Hence, higher thermal efficiency is achieved. Moreover, in an ICRC engine, the combustion temperature is higher and the combustion rate is faster compared with a conventional air-combustion engine, because oxygen concentration is higher. Hence,

a large number of water can be injected into the cylinder to increases the mass of the working gas. The mass of the injected water can be more than 12 times more than the mass of the fuel in our pervious experiment, and even more with optimizing combustion [50],[56]. Higher combustion temperature can be reach in ideal thermodynamic model, and therefore more water can be added as working fluid with less negative impact due to higher in-cylinder temperature. A large number of water is injected into the cylinder under the operation condition of Fig. 8.38. Considering the main component is $CO_2$ (molar mass 44) after the combustion, the mole number of the water vapor (molar mass 18) is more than the original working gas in expansion stroke. Hence, it is shown in Fig. 8.38 that a large percentage of work (about 69% when the compression ratio is 14) is produced by water steam in the engine, which is the reason why this cycle is referred to a special kind of Rankine cycle. Fig. 8.39 shows that exhaust gas temperature under different compression ratio. The exhaust gas temperature decreases with the increase of water/intake mass ratio. Longer expansion stroke is propitious to the conversion of combustion heat energy to the kinetic energy of the piston under higher compression ratio. Thus, it is also shown in Fig. 8.39 that the exhaust temperature decreases slightly under higher compression ratio.

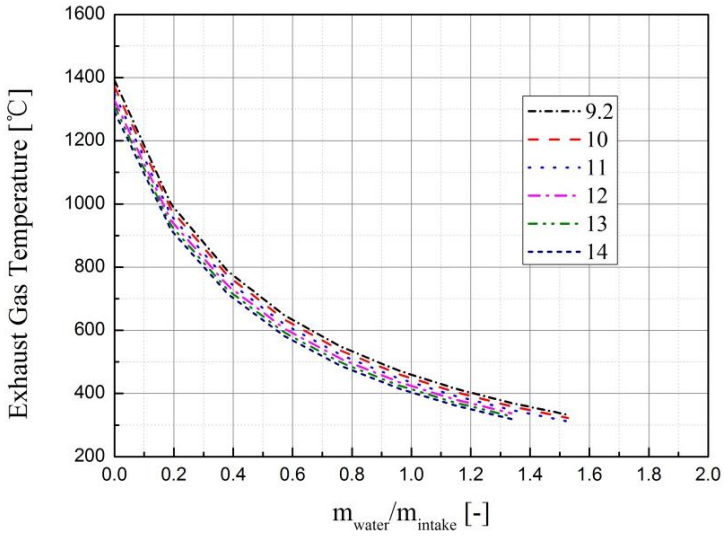


**Fig. 8.39** Exhaust gas temperature under different compression ratio (2000rpm, water temperature 160°C)

Fig. 8.40 reports the thermal efficiency boundaries under different compression ratio, with 2000rpm engine speed and 160°C water injection temperature. Under same water/intake mass ratio, thermal efficiency increases with the increase of compression ratio. As shown in Fig. 8.39, the exhaust gas temperature decreases slightly with the increase of compression ratio, which has a slight influence on the heating of the injected water. But the higher thermal efficiency boundary is still achieved under higher compression ratio due to longer expansion stroke.

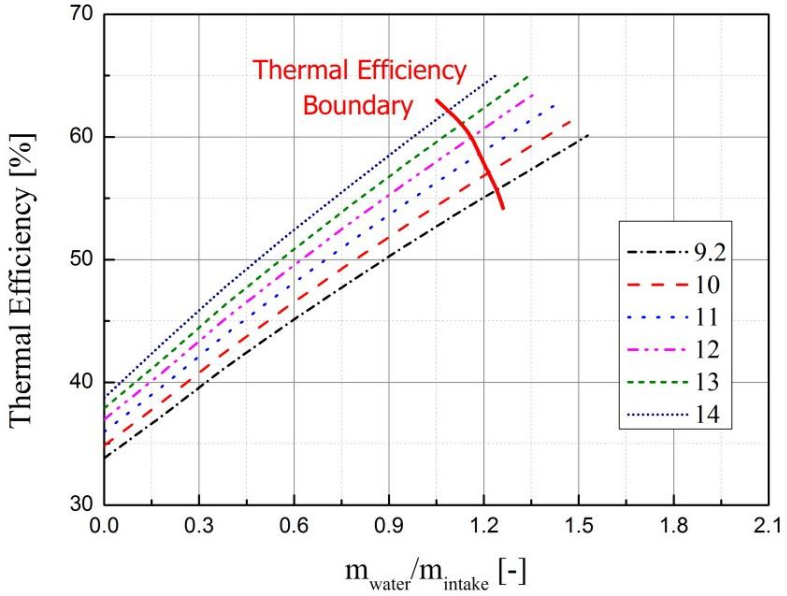


**Fig. 8.40** Thermal efficiency boundary under different compression ratio (2000rpm, water temperature 160°C)

Fig. 8.41 reports the comparison of thermal efficiency boundary between CR = 9.2 case and CR = 14 case, with 2000rpm engine speed. It is clear from Fig. 8.41 that higher thermal efficiency is achieved with the same water/intake mass ratio under higher compression ratio. However, the maximum allowable injected water mass is less under higher compression ratio due to the lower exhaust temperature. Moreover, the thermal efficiency boundary of CR = 14 case is higher, and the maximum thermal efficiency reaches to 62%.

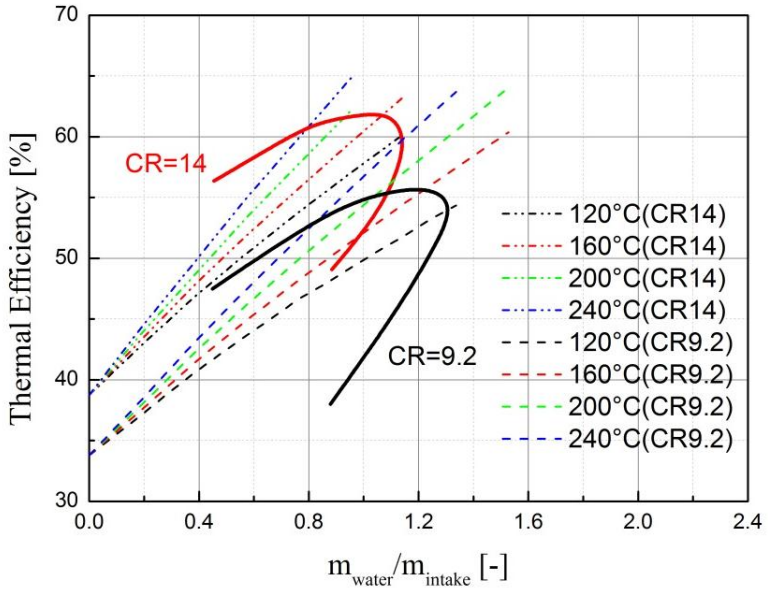


**Fig. 8.41** Comparison of thermal efficiency boundary between CR = 9.2 case and CR = 14 case (2000rpm)

In ICRC engine system, $CO_2$ can be separated and captured to achieve ultra-low emission through a subsystem. Hence, the energy consumption of $CO_2$ separation and capture system is analyzed in this section. $CO_2$ separation and capture is a complex process, and the installations in Fig. 8.1 are just the schematic diagram. For a better analysis, the $CO_2$ separation and capture system are considered as a whole, which is shown in Fig. 8.41, the all energy flow in $CO_2$ separation and capture system, including condenser and $CO_2$ pump, are analyzed and estimated. An operation condition with high thermal efficiency (Table 8.15) is employed to analyze the energy consumption of CO2 separation and capture system. Thermochemical properties of the species in this section come from NIST-JANAF Thermochemical Tables [64].

**Table 8.15** Operation Condition for the energy consumption estimation of $CO_2$ separation and capture system

| ***Item*** | ***Value*** |
|---|---|
| Compression ratio | 14 |
| Engine speed | 2000rpm |

| | |
|---|---|
| Oxygen concentration | 45% |
| Intake charge mass | 104.68mg |
| Fuel mass | 4.98mg |
| Water injection mass | 100mg |
| Indicated work | 153.5J |
| Outlet temperature of heat exchange | 181°C |
| Thermal efficiency after considering heat exchange | 62% |

In this operation condition, the oxygen concentration of intake charge is 45% and intake charge mass is 104.68mg according to Table 8.15, and therefore the mole number of $O_2$ and $CO_2$ are 1.49*10^-3mol and 1.22*10^-3mol. In order to control the combustion and keep the $CO_2$ concentration (55%) in inlet, 80% exhaust gas is recycled into the inlet. Hence, about 0.366*10^-3mol $CO_2$, 0.138*10^-3mol $O_2$ and 1.2*10^-3mol $H_2O$ (the outlet temperature of the heat exchange is 181$^oC$) are into the $CO_2$ separation and capture system. In order to separate $H_2O$ from the mixture gas, the temperature of mixture should be reduced to 30°C. The heat release of the mixture to heat management system during this process is about 8.52J. Because the saturated vapor pressure of $CO_2$ under 30 $^oC$ is 7.39MPa. Hence, after $H_2O$ is separated from the mixture gas, the mixture is pressured up to 7.39MPa to separate $CO_2$ from the mixture. 6.2J work is employed to the pressurizing process by a compression pump. The heat release of the $CO_2$ liquefaction heat to heat management system during this process is about 6.11J. Moreover, the heat used to evaporate liquid $O_2$ from heat management system is 8.55J. Hence, the input work of the whole system is 6.2J, and heat release of the whole system is 6.08J. The heat release of the system is so small that it can be taken away through engine cooling system (water or air cooling) easily. Therefore, the energy consumption of $CO_2$ separation and capture system is 6.2J. Because the indicated work of this operation condition is 153.5J, the energy loss ratio used for $CO_2$ separation and capture is about 4%, which accounts for a small proportion of the indicated work. Hence, the

system thermal efficiency under this operation condition is about 58% when heat exchange and $CO_2$ capture are considered.

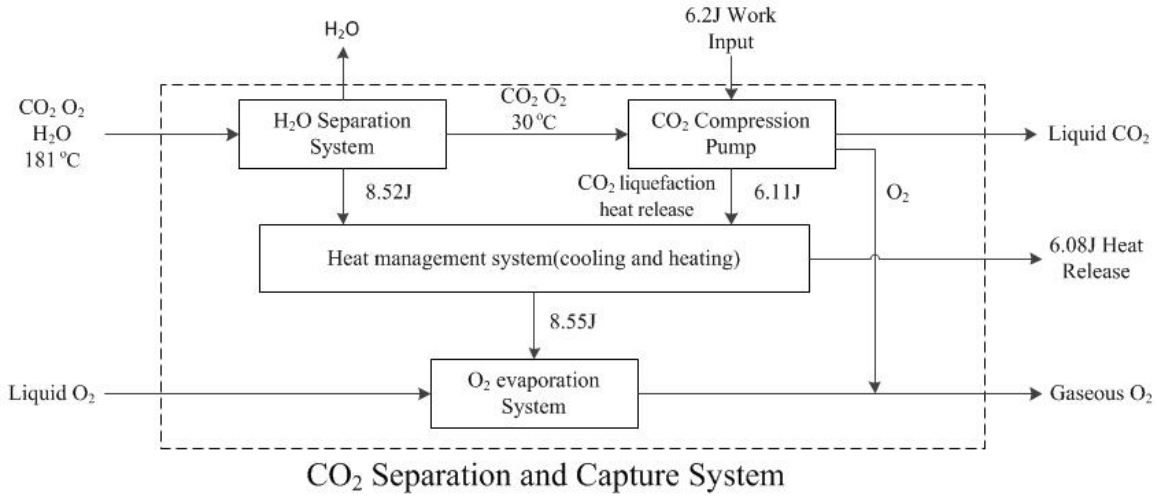


**Fig. 8.42** Energy flow in $CO_2$ separation and capture system

## 8.5 Conclusion

A novel oxy-fuel combustion system with water injection for reciprocating engines was discussed in this thesis. The injected water heated through exhaust gas (waste heat) is injected into the cylinder to control the rapid oxy-fuel combustion rate and temperature. Moreover, the injected water evaporates and increases the mass of the working fluid near TDC. Hence, higher thermal efficiency is obtained. The working fluid was chosen using an ideal engine thermodynamic model developed by the authors. The experiments were conducted using an self-design ICRC engine with port fuel injection and direct in-cylinder water injection that was designed by the authors. The effects of the working fluid on the combustion and emission characteristics were investigated. An ideal engine thermodynamic model combined with a heat exchange model was developed for the purpose of investigating the thermal efficiency upper boundary of this cycle, and the thermal efficiency boundaries under different operation conditions and engine compression ratio were investigated. The major conclusions of the present study are as follows:

(1) The injected water increases the thermal efficiency of the ICRC engine cycle significantly. The thermodynamic model results show that thermal efficiency

increases as the injected water mass increases. $CO_2$ (EGR) is a suitable diluent and working fluid for ICRC engines due to the less negative compression work.

(2) The injected water increases the mass of the working fluid during expansion strokes. The indicated work and thermal efficiency increased significantly compared with the dry cycles due to water injection. Lower intake pressures decrease the negative compression work and increase the thermal efficiency through the injected water added to the working fluid of the expansion stroke. Higher oxygen concentrations and higher compression ratios increase the combustion temperature in the cylinder and therefore are promising for achieving higher water vapor work and thermal efficiencies in ICRC engines. The indicated work and ITE increased by 12.4% and 3.1%, respectively, compared to the oxy-fuel combustion separately, and the ITE increased by 4.9% compared that for air combustion for a fuel injection duration of 52.9 ms, a water injection temperature of 120 °C and a compression ratio of 12.5.

(3) Lower intake pressures and higher oxygen concentrations increase combustion speed and decrease HC emissions. Moreover, NOx emissions remain low because the water injection process reduces the in-cylinder temperature significantly.

(4) Reasonable water injection durations decrease the cyclic variation of an ICRC engine under higher loads (higher fuel mass, higher oxygen concentrations and higher compression ratios). Excess injected water has a negative effect on engine stability.

(5) The injected water is heated by exhaust gas in an ICRC engine, and the temperature of injected water and thermal efficiency cannot be achieved without other assisted heating methods if exhaust gas temperature is insufficient for water heating. Hence, a thermal efficiency boundary of this system is obtained when the heat exchange between injected water and exhaust gas was considered. The maximum thermal efficiency increases from 33% (without water injection) to 56% when engine speed is 2000rpm and engine compression ratio is 9.2.

(6) The injected water can be heated to higher temperature under lower heat transfer medium mass flow rate due to higher heat exchanger effectiveness, with the same cold/hot flow mass ratio. Hence, a higher thermal efficiency is achieved under lower engine speed and intake pressure. Moreover, I/F ratio has little influence on thermal efficiency boundary.

(7) Addition of water into the combustion process can decrease the in-cylinder temperature and increases the water vapor concentration before the combustion of next cycle. Thus, a higher engine compression ratio can be utilized in the ICRC engine. Under higher compression ratio, combustion energy is efficiently converted into work due to longer expansion stroke, and higher thermal efficiency boundary is achieved. The best thermal efficiency increases from 56% to 62% with the increase of engine compression ratio from 9.2 to 14. The energy consumption of $CO_2$ separation and capture system accounts for about 4% of the indicated work, and therefore the best thermal efficiency of the whole ICRC system can still reach to 58% when the energy consumption of $CO_2$ separation and capture system is considered.

# Reference


[1] A.E. Catania, S. d'Ambrosio, R. Finesso, E. Spessa, G. Cipolla and A. Vassallo,Combustion system optimization of a low compression-ratio PCCI diesel engine for light-duty application, SAE Int J Engines 2 (1), 2009, 1314–1326,DOI: 10.4271/2009-01-1464.

[2] J.B. Heywood, Internal combustion engine fundamentals, 1988, McGraw-Hill Intern.

[3] Finesso R, Spessa E. Estimation of the engine-out NO2/NOx ratio in a EURO VI diesel engine. SAE paper no. 2013-01-0317; 2013.

[4] Ericson C, Westerberg B, Andersson M, Egnell R. Modelling diesel engine combustion and NOx formation for model based control and simulation of engine and exhaust aftertreatment systems. SAE paper no 2006-01-0687; 2006.

[5] Andersson M, Johansson B, Hultqvist A, Noehre C. A predictive real time NOx model for conventional and partially premixed diesel combustion. SAE paper no. 2006-01-3329; 2006.

[6] Zeldovich YB, Sadovnikov PY, Kamenetskii DAF. Oxidation of nitrogen in combustion. Translation by M. Shelef. Moscow-Leningrad: Academy of Sciences of USSR, Institute of Chemical Physics; 1947.

[7] G.A. Lavoie, J.B. Heywood and J.C. Keck, Experimental and theoretical study of nitric oxide formation in internal combustion engines, Combust Sci Technol 1, 1970, 313–326, DOI: 10.1080/00102206908952211.

[8] Miller R, Davis G, Lavoie G, Newman C, Gardner T. A super-extended Zel'dovich mechanism for NOx modeling and engine calibration. SAE paper no. 980781; 1998.

[9] J.A. Miller and C.T. Bowman, Mechanism and modeling of nitrogen chemistry in combustion, Prog Energy Combust Sci 1989 (15), 1989, 287–338.

[10] S.R. Turns, An introduction to combustion: concepts and applications, 2nd ed., 1999, McGraw-Hill Higher Education; New York, NY.

[11] Fenimore CP. Formation of nitric oxide in premixed hydrocarbon flames. In: 13th symp. (Int'l.) on combustion. The Combustion Institute; 1971. p. 373.http://dx.doi.org/10.1016/s0082-0784(71)80040-1.

[12] Dec JD. A conceptual model of diesel combustion based on laser-sheet imaging. SAE paper no. 970873; 1997.

[13] R. Finesso and E. Spessa, a real time zero-dimensional diagnostic model for the calculation of in-cylinder temperatures, HRR and nitrogen oxides in diesel engines, Energy Convers Manage 79, 2014, 498–510,DOI: 10.1016/j.enconman.2013.12.045, ISSN: 0196-8904.

[14] Finesso R, Spessa E. Real-time predictive modeling of combustion and NOx formation in diesel engines under transient conditions. SAE technical paper 2012-01-0899; 2012. http://dx.doi.org/10.4271/2012-01-0899.

[15] V. Rao and D. Honnery, A comparison of two NOx prediction schemes for use in

diesel engine thermodynamic modeling, Fuel 107, 2013, 662–670.
[16] M. Baratta, A.E. Catania, A. Ferrari, R. Finesso and E. Spessa, Premixed-diffusive multizone model for combustion diagnostics in conventional and PCCI diesel engines, J Eng Gas Turbines Power ASME Trans 133 (10),2011, 102801-1–102801-13, ISSN: 0742-4795.
[17] Catania AE, Finesso R, Spessa E. Diagnostics of mixing process dynamics, combustion and emissions in a Euro V diesel engine. SAE paper no. 2011-24-0018. In: ICE 2011, 10th international conference on engine and vehicles, Capri (NA), Italy; September 11–15, 2011.
[18] R. Finesso and E. Spessa, Analysis of combustion and emissions in a EURO V diesel engine by means of a refined quasi-dimensional multizone diagnostic model, SAE Int J Engines 5 (3), 2012, DOI: 10.4271/2012-01-106.
[19] V. Rao and Damon Honnery, A comparison of two NOx prediction schemes for use in diesel engine thermodynamic modeling, Fuel 107, 2013, 662–670.
[20] J. Asprion, O. Chinellato and L. Guzzella, A fast and accurate physics-based model for the NOx emissions of diesel engines, Appl Energy 103, 2013,221–233.
[21] J. Asprion, O. Chinellato and L. Guzzella, Optimisation-oriented modelling of the NOx emissions of a Diesel engine, Energy Convers Manage 75, 2013,61–73.
[22] M. Hirsch, K. Oppenauer and L. Del Re, Dynamic engine emission models. Automotive model predictive control, 2010, Springer; Berlin, Heidelberg, p. 73–87. http://dx.doi.org/10.1007/978-1-84996-071-7_5.
[23] Brace C. Prediction of diesel engine exhaust emissions using artificial neural networks. Lucas electrical and electronic systems-neural networks in systems design, Solihull, UK; 10 June 1988.
[24] Del Re L, Langthaler P, Furtmueller C, Winkler S, Affenzeller M. NOx virtual sensor based on structure identification and global optimization. SAE technical paper 2005-01-0050; 2012. http://dx.doi.org/10.4271/2005-01-0050.
[25] S. Roy, R. Banerjee and P.K. Bose, Performance and exhaust emissions prediction of a CRDI assisted single cylinder diesel engine coupled with EGR using artificial neural network, Appl Energy 119, 2014, 330–340.
[26] Gärtner U, Hohenberg G, Daudel H, Oelschlegel H. Development and application of a semi-empirical NOx model to various HD diesel engines. Thermo- and fluid dynamic processes in diesel engines 2. In: Selected papers from the THIESEL 2002 conference, Valencia, Spain; 11–13 September 2002. http://dx.doi.org/10.1007/978-3-662-10502-3_14.
[27] Krishnan A, Sekar VC, Balaji J, Boopathi SM. Prediction of NOx reduction with exhaust gas recirculation using the flame temperature correlation technique. In: Proceedings of the national conference on advances in mechanical engineering, Kota, India. ECKAME-2006-T-23; March 18–19, 2006. pp. 378–85.
[28] C. Guardiola, J.J. López, J. Martin and D. García-Sarmiento, Semiempirical in-cylinder pressure based model for NOx prediction oriented to control applications, Appl Therm Eng 2011,DOI: 10.1016/j.applthermaleng.2011.05.048.
[29] Arregle J, López JJ, Guardiola C, Monin C. Sensitivity study of a NOx estimation model for on-board applications. SAE paper 2008-01-0640; 2008.

[30] Pierpont DA, Reitz RD. Effects of Injection pressure and nozzle geometry on D.I. diesel emissions and performance. SAE paper no. 950604. 1995. http://dx.doi.org/10.4271/950604.
[31] Catania AE, Finesso R, Spessa E. Real-time calculation of EGR rate and intake charge oxygen concentration for misfire detection in diesel engines. SAE paper no. 2011-24-0149. In: ICE 2011, 10th international conference on engine and vehicles, Capri (NA), Italy; September 11–15, 2011.
[32] S. d'Ambrosio, R. Finesso and E. Spessa, Calculation of mass emissions, oxygen mass fraction and thermal capacity of the inducted charge in SI And diesel engines from exhaust and intake gas analysis, Fuel 90 (1), 2011,152–166, DOI: 10.1016/j.fuel.2010.08.02, ISSN: 0016-2361.
[33] Huber K, Woschni G, Zeilinger K. Investigations on heat transfer in internal combustion engines under low load and motoring conditions. SAE Paper No. 905018; 1990.
[34] Catania AE, d'Ambrosio S, Ferrari A, Finesso R, Spessa E, Avolio G, et al. Experimental analysis of combustion processes and emissions in a 2.0L multi-cylinder diesel engine featuring a new generation Piezo-driven injector. SAE paper no. 2009-24-0040. In: ICE 2009, 9th international conference on engine and vehicles, Capri (NA), Italy; September 13–18, 2009. http://dx.doi.org/10.4271/2009-24-0040.
[35] C. Beatrice, P. Napolitano and C. Guido, Injection parameter optimization by DoE of a light-duty diesel engine fed by Bio-ethanol/RME/diesel blend, Appl Energy 113, 2014, 373–384.
[36] ISO/IEC GUIDE 98-3:2008(E).
[37] B.J.P. Buhre, L.K. Elliott, C.D. Sheng, et al. Oxy-fuel combustion technology for coal-fired power generation. Progress in Energy and Combustion Science: 2005; 31:283–307.
[38] Zheng L. Oxy-fuel combustion for power generation and carbon dioxide (CO2) capture. Woodhead Publishing Series in Energy: Number 17, Cambridge, 2011.
[39] Andrzej Ziebik, Paweł Gładysz. Analysis of cumulative energy consumption in an oxy-fuel combustion power plant integrated with a CO2 processing unit. Energy Conversion and Management: 2014; 87:1305–1314.
[40] Park SK, Kim TS, Sohn JL, Lee YD. An integrated power generation system combining solid oxide fuel cell and oxy-fuel combustion for high performance and CO2 capture, Applied Energy 2011;88(4):1187-96.
[41] Maja B. Toftegaard, Jacob Brix, Peter A. Jensen. Oxy-fuel combustion of solid fuels. Progress in Energy and Combustion Science: 2010; 36:581-625.
[42] Akshay Gopan, Benjamin M. Kumfer, Jeffrey Phillips, et al. Process design and performance analysis of a Staged, Pressurized Oxy-Combustion (SPOC) power plant for carbon capture. Applied Energy: 2014; 125:179–188.
[43] Anderson, R.E., Doyle, S.E., K.L. Pronske, et al. Demonstration and commercialization of zero-emission power plants. 29th International Technical Conference on Coal Utilization & Fuel Systems, Clearwater, FL, 2004; April:18-22.
[44] Bilger, R. W.. Zero release combustion technologies and the oxygen economy.

Fifth International Conference on Technologies and Combustion for a Clean Environment. Lisbon, Portugal, 1999; Jul.12-15:1039-1046.
[45] Bilger R W., Zhijun Wu. Carbon Capture for Automobiles Using Internal Combustion Rankine Cycle Engines. Journal of Engineering for Gas Turbines and Power: 01/2009, 131(3): 10-13.
[46] Lanzafame R, "Water injection effects in a single-cylinder CFR engine," SAE Paper 1999-01-0568, 1999.
[47] R.B. Melton Jr., S.J. Lestz, R.D. Quillian Jr, "Direct water injection cooling for military engines and effects on the diesel cycle," Fifteenth Symposium (International) on Combustion. 1975; 15(1):1389–1399.
[48] V. Subramanian, J.M. Mallikarjuna, A. Ramesh, "Effect of water injection and spark timing on the nitric oxide emission and combustion parameters of a hydrogen fuelled spark ignition engine," International Journal of Hydrogen Energy. 2007; 32:1159 – 1173.
[49] B. Tesfa, R. Mishra, F.Gu. Water injection effects on the performance and emission characteristics of a CI engine operating with biodiesel. Renewable Energy: 2012; 37:333-344.
[50] Zhijun WU, Xiao Yu, Lezhong FU. A high efficiency oxyfuel internal combustion engine cycle with water direct injection for waste heat recovery. Energy: 2014; 70:110-120.
[51] Saidur R, Rezaei M, Muzammil WK, et.al. Technologies to recover exhaust heat from internal combustion engines. Renewable and Sustainable Energy Reviews: 2012; 16:5649-59.
[52] M. Hatamin, D.D. Ganji, M. Gorji-Bandpy. A review of different heat exchangers designs for increasing the diesel exhaust waste heat recovery. Renewable and Sustainable Energy Reviews. 2014; 37:168–181.
[53] Conklin J C, Szybist J P. A highly efficiency six-stroke internal combustion engine cycle with water injection for in-cylinder exhaust heat recovery. Energy: 2010; 35(4):1658-1664.
[54] Le-zhong Fu, Zhijun Wu, Liguang Li, et al. Effect of Water Injection Temperature on the Combustion and Emission Characteristics of an Internal Combustion Rankine Cycle Engine. SAE paper: 2014-01-2600, 2014.
[55] Zhijun Wu, Lezhong Fu, Yang Gao, et al. Thermal efficiency boundary analysis of an internal combustion Rankine cycle engine. Energy, 2016; 94: 38-49.
[56] Zhi-jun Wu, Xiao Yu, Le-zhong Fu, et al. Experimental study of the effect of water injection on the cycle performance of an internal combustion Rankine cycle engine. Proc. IMechE Part D: Journal of Automotive Ennineering, 2014, 288(5): 580-588.
[57] Reynolds WC. STANJAN chemical equilibrium solver, version 3.94. Stanford, CA: Department of Mechanical Engineering, Stanford University. 1987.
[58] A.N.Mazas, B.Fiorina, D.A.Lacoste, et al. Effects of water vapor addition on the laminar burning velocity of oxygen-enriched methane flames. Combustion and Flame 2011; 158: 2428-2440.
[59] H.G. Zhanga, X.J. Hana, B.F. Yao, et al. Study on the effect of engine operation

parameters on cyclic combustion variations and correlation coefficient between the pressure-related parameters of a CNG engine. Applied Energy 2013; 104: 992–1002.

[60] Warren M. Rohsenow, James R Hartnett, Young I. Cho. Handbook of Heat Transfer (3rd Edition). McGraw-Hill. 1998.

[61] D. Q. Kern. Porcess Heat Transfer (International Edition). McGraw-Hill. 1965.

[62] William S. Janna. Engineering Heat Transfer, Second Edition. CRC Press. 1999.

[63] F. P. Incropera, D. P. DeWitt, T. L. Bergman, et al. Fundamentals of Heat and Mass Transfer, 6th edition. John Wiley & Sons, US, 2006.

[64] M.W. Chase Jr. NIST-JANAF Thermochemical Tables, Fourth Edition (PARTS I&II). National Institute of Standards and Technology .1998.